

INFORMATION TO USERS

This manuscript has been reproduced from the microfilm master. UMI films the text directly from the original or copy submitted. Thus, some thesis and dissertation copies are in typewriter face, while others may be from any type of computer printer.

The quality of this reproduction is dependent upon the quality of the copy submitted. Broken or indistinct print, colored or poor quality illustrations and photographs, print bleedthrough, substandard margins, and improper alignment can adversely affect reproduction.

In the unlikely event that the author did not send UMI a complete manuscript and there are missing pages, these will be noted. Also, if unauthorized copyright material had to be removed, a note will indicate the deletion.

Oversize materials (e.g., maps, drawings, charts) are reproduced by sectioning the original, beginning at the upper left-hand corner and continuing from left to right in equal sections with small overlaps.

ProQuest Information and Learning
300 North Zeeb Road, Ann Arbor, MI 48106-1346 USA
800-521-0600

UMI[®]

**THE INFLUENCE OF TEXTURE ON THE RELIABILITY OF
ALUMINUM AND COPPER INTERCONNECTS**

BY

Kitae Lee

Department of Mining and Metallurgical Engineering,
McGill University, Montreal, CANADA
December, 2000.

A thesis submitted to the Faculty of Graduate Studies and Research in partial
Fulfillment of the requirements of the degree of Doctor of Philosophy.

© Kitae Lee, 2000.



National Library
of Canada

Acquisitions and
Bibliographic Services

395 Wellington Street
Ottawa ON K1A 0N4
Canada

Bibliothèque nationale
du Canada

Acquisitions et
services bibliographiques

395, rue Wellington
Ottawa ON K1A 0N4
Canada

Your file *Votre référence*

Our file *Notre référence*

The author has granted a non-exclusive licence allowing the National Library of Canada to reproduce, loan, distribute or sell copies of this thesis in microform, paper or electronic formats.

The author retains ownership of the copyright in this thesis. Neither the thesis nor substantial extracts from it may be printed or otherwise reproduced without the author's permission.

L'auteur a accordé une licence non exclusive permettant à la Bibliothèque nationale du Canada de reproduire, prêter, distribuer ou vendre des copies de cette thèse sous la forme de microfiche/film, de reproduction sur papier ou sur format électronique.

L'auteur conserve la propriété du droit d'auteur qui protège cette thèse. Ni la thèse ni des extraits substantiels de celle-ci ne doivent être imprimés ou autrement reproduits sans son autorisation.

0-612-70075-5

Canada

ABSTRACT

Texture in films develops during deposition processes and annealing of patterned wafers. Recent studies show that texture influences the performance and reliability of both aluminum and copper interconnects. To improve the current understanding of this matter, the influence of texture on reliability was studied.

The influence of texture on electromigration and stress-induced failures in aluminum interconnects was studied since these are the most often responsible for failures observed in aluminum interconnects. Results obtained showed that a strong $\{111\}$ texture in aluminum interconnects improves their median time-to-failure. The grain boundary character distribution and percentage of coincidence site lattice (CSL) boundaries, was quantified using orientation imaging microscopy. It was found that the median time-to-failure of specimens increased as the number of low angle and CSL boundaries increased. These boundaries are known to have low diffusivity. It was also demonstrated that while the investigated specimens had grains of comparable size, the grains of similar orientations were clustered in the specimens having the stronger $\{111\}$ texture. This phenomenon contributed to the longer median time-to-failure of the interconnects by reducing the frequency of high angle grain boundaries. The experimental data obtained shows that the residual stress in films decreases as the intensity of the $\{111\}$ texture increases. A model based on Monte-Carlo simulation of texture formation during the deposition of aluminum film was proposed to suggest the optimum conditions for a growth of a strong $\{111\}$ texture component. A low deposition rate and a high mobility of atoms on the surface, which corresponds to a high substrate temperature, can strengthen $\{111\}$ texture.

Copper has been recently used as an interconnecting material because of its good electromigration resistance and low electrical resistivity. One of the major problems of copper as an interconnecting material is that it easily oxidizes at relatively low temperatures. The formation of oxide degrades the electrical and mechanical properties

of copper interconnects. The influence of substrate texture on the oxidation kinetics was studied to suggest methods to reduce copper oxidation. Copper single crystals having (100), (110), (123), (314), (111) and (311) orientations were oxidized at 200°C in air. Only the Cu₂O phase was formed during oxidation. The oxidation of the (100) single crystal substrate was much faster than that of the others. This is attributed to a large number of fine oxide grains on the (100) crystal in the initial stages of oxidation. It is recommended that the {100} texture in copper interconnects should be avoided in order to reduce oxidation rate. A quantitative model was proposed to predict the oxidation kinetics of copper from the texture of the specimens. Reasonable agreement was obtained comparing the model predictions and the experimental results obtained from the test of oxidation of polycrystalline copper specimens. However, further improvement of the model can be done if more data from single crystal experiments are obtained.

RÉSUMÉ

La texture dans les couches minces se déroule durant les processus de déposition et de recuit des wafers. Des études récentes ont montré que la texture influence la performance et la fiabilité des interconnexions de cuivre et d'aluminium. Afin de comprendre ce phénomène, l'influence de la texture sur la fiabilité des couches minces a été étudiée.

L'influence de la texture sur l'électromigration ainsi que l'application de contraintes dans les interconnexions d'aluminium ont été étudiées puisque celles-ci sont les facteurs le plus souvent responsables de rupture observées sur les interconnexions d'aluminium. Les résultats obtenus ont montré qu'une forte texture $\{111\}$ améliore la résistance à la rupture pour les interconnexions en aluminium. La distribution des joints de grains et le pourcentage de la superposition de joints de grains spéciaux, ont été quantifiés à l'aide d'un OIM (Orientation Imaging Microscope). Il a été découvert que la résistance à la rupture des échantillons augmente quand le nombre de sous-joints de grains et que la superposition de joints de grains spéciaux augmentent. Ces joints de grains sont connus pour avoir une faible diffusivité. Il a notamment été démontré que dans les échantillons analysés possédant une taille de grain comparable, les grains ayant une orientation similaire étaient amassés dans les échantillons ayant une texture $\{111\}$ la plus forte. Ce phénomène contribue à la résistance à la rupture des interconnexions en réduisant la fréquence des joints de grains fortement désorientés. Les données expérimentales obtenues montrent que la contrainte résiduelle dans les couches minces décroît lorsque l'intensité de la texture dans la famille de plan $\{111\}$ augmente. À l'aide du modèle de Monte Carlo, un modèle de simulation concernant la formation de la texture durant la déposition d'un film d'aluminium a été proposé pour prédire les conditions optimales de la croissance d'une forte texture $\{111\}$ dans l'échantillon. Une faible vitesse de déposition et une grande mobilité des atomes à la surface, ce qui correspond à une haute température du substrat, peuvent renforcer la texture $\{111\}$.

Le cuivre a récemment été utilisé comme matériel d'interconnection dû à sa bonne résistance à l'électromigration et à sa faible résistivité électrique. L'un des problèmes majeurs du cuivre est le fait que celui-ci s'oxyde à très faible température. La formation d'oxyde diminue les propriétés mécaniques et électriques des interconnections de cuivre. L'influence de la texture du substrat sur la cinétique d'oxydation a été étudiée afin de proposer des méthodes pour réduire l'oxydation du cuivre. Des monocristaux de cuivre ayant les orientations suivantes: (100), (110), (123), (314), (111) et (311) ont été oxydés à 200 °C à l'air. Une unique phase de Cu_2O a été formée durant l'oxydation. L'oxydation du monocristal ayant l'orientation (100) était plus rapide que les autres. Ceci a été attribué à la présence d'un large nombre d'oxydes de grains très fins durant les premiers stades d'oxydation. Il est recommandé d'éviter la texture {100} dans les interconnections de cuivre afin de réduire la vitesse d'oxydation. Un modèle quantitatif a été proposé pour prédire la cinétique d'oxydation du cuivre à partir de la texture des échantillons. Une corrélation raisonnable entre les résultats expérimentaux et le modèle théorique a été obtenue sur les tests d'oxydation des échantillons polycristallins de cuivre. Cependant, des améliorations sur le modèle peuvent être effectuées si des données supplémentaires sur les expériences de monocristaux sont obtenues.

ACKNOWLEDGEMENTS

First of all, I would like to express my deepest gratitude and appreciation to my thesis supervisor J. A. Szpunar for his guidance, support, encouragement and invaluable advices throughout the course of this work.

I would like to thank Dr. D. B. Knorr for his advice and his discussions on the nature of the electronic thin films. I would also like to thank Dr. D. P. Field from the TexSEM Lab for his advice on the orientation imaging microscope that provided me good quality data. I would like to thank to Dr. K. P. Rodbell, Prof. S. Dobrzynski and Prof. J. Kuśnierz for offering the specimens.

Special thanks to Prof. H. T. Jeong for his discussions and help in developing the computer model of the oxidation kinetics. I also like to thank F. Andersen for his help in making the computer program for the simulation of texture development.

I would like to thank Aluminum Canada (ALCAN) Inc. for enabling a one year scholarship.

I want to express my sincere thanks to Slavek Poplawski, Peter Blanford, Jongtae Park, Baekyun Kim, and Jaeyoung Cho for their advice, encouragement and friendship. I also would like to thank the people from the texture Lab and beyond, who have made my stay at McGill all the more enjoyable. This includes: Byeoungsoo Ahn, Hualong Li, Jianlong Lin, Raj Narayanan, Yang Cao, Raed Hazhaikch, Rachid Nciri, Mike Glavicic, Askal Sheikh-Ali, Neil D'Souza, Val Gertsman, Yasuyuki Hayakaya, Dongyang Li, Jian Lu, Frank Czerwinski, Brian Morris, Hyunsoo Park, Sasha Zhilyaev, Marius Birsan, Sanghyun Cho, Hyungbae Kim, Jinsoo Kim, Sungmo Yang, Jaehun Oh, Kihyun Mun.

Finally, I am very grateful to my parents for their support, understanding and love. Without them, this work could not have been completed.

TABLE OF CONTENTS

	page
ABSTRACT	i
RESUME	iii
ACKNOWLEDGEMENT	v
TABLE OF CONTENTS	vi
LIST OF FIGURES	ix
LIST OF TABLES	xiv
CHAPTER 1: INTRODUCTION	1
CHAPTER 2: LITERATURE REVIEW	6
2.1. A REVIEW OF TEXTURE	7
2.2. INTEGRATED CIRCUIT (IC) TECHNOLOGY	14
2.2.1. Historical Background	14
2.2.2. Fabrication Process of Integrated Circuit	17
2.3. METALLIZATION FOR THE INTEGRATED CIRCUITS	24
2.4. RELIABILITY CONCERNS IN METALLIZATION	30
2.4.1. Electromigration in Thin Films	30
2.4.2. Stress-Induced Voids in Thin Films	36
CHAPTER 3: EXPERIMENTAL TECHNIQUES	40
3.1. X-RAY DIFFRACTOMETRY	41
3.1.1. Texture Measurement using X-ray Diffraction	41
3.1.2. Measurement of Residual Stress by X-ray Diffraction	45

3.2. ORIENTATION IMAGING MICROSCOPY	47
3.3. ATOMIC FORCE MICROSCOPY	53
3.4. THERMOGRAVIMETRIC ANALYSIS	56
CHAPTER 4. THE INFLUENCE OF TEXTURE ON THE RELIABILITY OF ALUMINUM INTERCONNECTS	58
4.1. INTRODUCTION	59
4.2. EXPERIMENTAL PROCEDURES	61
4.2.1. Sample Preparation	61
4.2.2. Electromigration Test	61
4.2.3. Texture Measurement	63
4.2.4. Calculation of Grain Boundary Character Distribution (GBCD)	64
4.2.5. Microstructure Analysis	66
4.2.6. Measurement of Residual Stress	67
4.2.7. Monte-Carlo Simulation to Obtain the Optimum Texture	67
4.3. CORRELATION BETWEEN THE TEXTURE OF FILMS AND THEIR RELIABILITY	68
4.4. CORRELATION BETWEEN THE GRAIN BOUNDARY CHARACTER AND THE RELIABILITY OF INTERCONNECTS	74
4.5. INFLUENCE OF MICROSTRUCTURE ON THE FILM RELIABILITY	85
4.6. CORRELATION BETWEEN THE TEXTURE OF FILMS AND THEIR STRESS-INDUCED RELIABILITY CONCERNS	92
4.7. MONTE CALRO SIMULATION OF THE TEXTURE DEVELOPMENT IN ALUMINUM THIN FILMS	97
4.8. SUMMARY	105

CHAPTER 5: THE INFULENCE OF TEXTURE ON THE OXIDATION KINETICS OF COPPER	107
5.1. INTRODUCTION	108
5.2. EXPERIEMENTAL PROCEDURES	112
5.2.1. Sample Preparation	112
5.2.2. Oxidation Test	112
5.2.3. Texture Measurement	113
5.2.4. Microstructure Analysis	114
5.2.5. Prediction of Oxidation Kinetics of Copper	115
5.3. THE INFLUENCE OF SUBSTRATE ORIENTATIONI ON THE OXIDATION KINETICS OF COPPER	116
5.3.1. The Oxidation Kinetics of Copper Single Crystals	116
5.3.2. The Changes in the Oxide Texture during Oxidation	119
5.3.3. The Changes in the Morphology of Oxides during Oxidation	123
5.4. PREDICTION OF OXIDATION KINETICS FROM THE TEXTURE OF THE SPECIMEN	130
5.5. SUMMARY	140
CHAPTER 6: SUMMARY AND CONCLUSIONS	141
6.1. CONCLUSIONS	143
6.1.1. The Influence of Texture on the Reliability of Aluminum Thin Films	143
6.1.2. The Influence of Texture on the Oxidation Kinetics of Copper	144
6.2. STATEMENT OF ORIGINALITY	145
6.3. FUTURE WORK	146
REFERENCES	148

LIST OF FIGURES

Figure		Page
1.1	Exponential growth of the number of components per IC chip. (a), (b), (c) and (d) components per chip versus year for MOS, bipolar, MOSFET, and MODFET ICs, respectively [1, 2].	2
1.2	Exponential decrease of (a) minimum feature length, (b) junction depth, (c) gate oxide thickness of MOSFET [3].	2
2.1	The presentation of pole figure: (a) projection sphere and reference frame of the sheet, (b) projection of poles for a single grain, (c) projection of pole from textured grains, (d) pole figure with iso-density contour lines [17].	8
2.2	The sample-fixed coordinate K_A and the crystal-fixed coordinate system K_B in the sheet.	9
2.3	The definition of the Euler angle φ_1 , Φ , φ_2 : (a) the crystal coordinate system $K_B(X'Y'Z')$ lies parallel to the sample coordinate system $K_A(XYZ)$, (b) the crystal coordinate system is rotated around the Z' axis through the angle φ_1 , (c) the crystal coordinate system is rotated around the X' axis through the angle Φ , (d) the crystal coordinate system is rotated around the Z' axis through the angle φ_2 [18].	10
2.4	The ODF of the typical recrystallized ARMCO iron.	13
2.5	Location of fibers and some low index orientations on the (a) $\varphi_1 = 0^\circ$, (b) $\varphi_2 = 45^\circ$ sections of the ODF.	13
2.6	Sales of electronics in the United States. (a) Factory sales of electronics, (b) Integrated circuit market [23, 24].	16
2.7	Integrated circuit manufacturing process flow [25].	17
2.8	Stages in photolithography [26].	20
2.9	Boron diffusion system. (a) Solid diffusion source system, (b) Liquid diffusion source system, (c) Gaseous diffusion source system [27].	19

2.10	Ion implantation system [28]	22
2.11	Schematic cross section of typical MOSFET [29].	25
2.12	Schematic cross section of a multilevel metallization structure [30].	25
2.13	Schematic of simplified dc-magnetron sputtering system [3].	29
2.14	Model of electromigration damage in a thin film strip [39].	31
2.15	Schematic illustration of (a) a thin film grain structure. (b) a wide line with width, w , greater than average grain diameter, d . (c) a narrow line where width, w , is less than or about equal to d .	34
2.16	The effect of post-patterning annealing on the grain structure of interconnects.	35
2.17	Vacancy flow mechanisms generating wedge-shaped or slit-like void [49].	37
2.18	Grain boundary sliding model of hillock growth. (a) typical columnar grain structure. (b) lateral motion of neighboring grains for stress relaxation.	38
3.1	Schematic of x-ray diffractometer [51].	42
3.2	Schematic diagrams of (a) a vertical-axis texture goniometer. (b) the specimen rotation angles [52].	44
3.3	Definition of Euler angles ψ and ϕ with respect to the overall state of stress.	46
3.4	Schematic description of the Orientation Imaging Microscope.	48
3.5	Aluminum EBSP indexed using OIM.	50
3.6	OIM map of a recrystallized nickel alloy.	51
3.7	Discrete and shaded (100) pole figures for recrystallized aluminum.	52
3.8	Schematic of the sensing system of AFM.	55
3.9	A schematic of the TGA (TG-171) from Cahn Instruments Inc.	57
4.1	A schematic drawing of the partially ionized beam deposition.	62
4.2	A schematic of barrel plasma RIE system.	63
4.3	Orientation Distribution Function (ODF) for the specimen: (a) PIB2/1, (b) PIB2/2, (c) SP2.	69

4.4	$\varphi_l = 45^\circ$ sections of the ODF obtained from the three specimens.	70
4.5	A schematic of the basic energy equilibrium on a substrate surface during film formation.	70
4.6	The results of electromigration tests from the specimens.	72
4.7	Median time to failure as a function of the intensity of fiber texture.	73
4.8	Distribution of misorientation angle of grains in (a) PIB2/1. (b) PIB2/2. (c) SP2. (d) randomly oriented specimen.	75
4.9	The number fraction of low angle grain boundaries ($\theta < 15^\circ$).	77
4.10	Median time to failure as a function of number of Low angle grain boundaries.	77
4.11	Distribution of CSL boundaries obtained from OIM ($\Sigma 3 - \Sigma 29$).	79
4.12	Distribution of CSL boundaries obtained from ODF ($\Sigma 3 - \Sigma 29$).	80
4.13	Median time to failure as a function of total frequency of CSL boundaries from $\Sigma 3$ to $\Sigma 29$.	82
4.14	Frequency of low angle grain boundaries ($\theta < 15^\circ$) and CSL boundaries ($\Sigma 3 - \Sigma 29$) as a function of intensity of $\{111\}$ fiber texture.	82
4.15	Grain boundary and orientation map of the failed area.	84
4.16	Microstructure and grain size distribution of the specimens: (a) PIB2/1. (b) PIB2/2. and (c) SP2.	85-86
4.17	Average grain size as a function of misorientation angle [92].	88
4.18	Surface morphology obtained by atomic force microscope (AFM) from: (a) PIB2/1. (B) PIB2/1. and (c) SP2.	90
4.19	A stress-temperature profile for an Al-Si film deposited at 150°C .	93
4.20	A typical morphology of hillocks on the patterned line.	93
4.21	Correlation between the intensity of $\{111\}$ texture and the residual stress.	95
4.22	Median time to failure (MTF) as a function of residual stress.	96

4.23	Processes on substrate in the early stages of thin film growth: 1. Impingement on nucleus. 2. Diffusion to nucleus. 3. Impingement on substrate surface. 4. Diffusion on substrate surface. 5. Re-evaporation	97
4.24	Volume fraction of differently oriented grains with different deposition rates. Total deposition = 100.000 blocks. T =550 K. MCS =1 (The number of trials in each scan)	102
4.25	Volume fraction of differently oriented grains with different number of trials in each Monte Carlo scan. Total deposition = 100.000 blocks. T =550 K. Deposition rate =1.000 blocks per scan	103
4.26	Volume fraction of differently oriented grains having different conditions during the film deposition. Total deposition = 100.000 blocks. T =550 K	104
5.1	Reduced complexity: one of the main benefits of copper [105].	109
5.2	Oxidation kinetics of the copper single crystals having different faces. at 200°C.	117
5.3	Pressure-temperature stability region for Cu ₂ O and CuO [116].	118
5.4	Volume fraction of different texture components in Cu ₂ O oxidized at 200°C for (a) 1 minute, (b) 30 minutes, (c) 3 hours and (d) 9 hours.	120- 121
5.5	The morphology and roughness of oxide after 1 minute at 200°C on the (a) (100) face, (b) (110) face, (c) (123) face, (d) (314) face, (e) (111) face and (f) (311) face.	125
5.6	The morphology and roughness of oxide after 30 minutes at 200°C on the (a) (100) face, (b) (110) face, (c) (123) face, (d) (314) face, (e) (111) face and (f) (311) face.	126
5.7	The morphology and roughness of oxide after 3 hours at 200°C on the (a) (100) face, (b) (110) face, (c) (123) face, (d) (314) face, (e) (111) face and (f) (311) face.	127

5.8	The morphology and roughness of oxide after 9 hours at 200°C on the (a) (100) face, (b) (110) face, (c) (123) face, (d) (314) face, (e) (111) face and (f) (311) face.	128
5.9	The cross-sections of oxides on specimen C, which oxidized at 200°C for (a) 1 minute and (b) 30 minutes.	129
5.10	Oxidation inverse pole figures generated at various oxidation times: (a) 60 seconds, (b) 1.800 seconds, (c) 3.600 seconds, (d) 10.800 seconds, (e) 18.000 seconds, and (f) 32.640 seconds.	132
5.11	Inverse pole figures generated for the specimens assumed to have different orientations.	134
5.12	Oxidation kinetics simulated for the specimens having different orientations.	135
5.13	Oxidation kinetics of the copper polycrystalline specimens at 200°C.	136
5.14	Texture of the polycrystalline specimens: (a) PA, (b) PB, (c) PC and (d) randomly oriented specimen.	138
5.15	Oxidation kinetics simulated for the specimens PA, PB, PC and the randomly oriented specimen.	139

LIST OF TABLES

Table		Page
2.1	Specified requirements for the various metallization.	27
2.2	Metallization schemes being used for IC fabrication.	27
2.3	Thermal expansion coefficients for some materials.	36
4.1	Surface energy of nine aluminum grains used for the simulation (at 550 K. calculated by ADESH program)	100

Chapter 1

Introduction

A modern integrated circuit (IC) is composed of 10^8 or more electronic devices. These devices form a circuit by metallic films patterned into strips, which function as wires to interconnect devices. The wires are usually simply referred to as interconnects. In an IC occupying a surface area of 1 cm^2 Si substrate, there can be more than 10 m of total interconnect length. This length is in the form of more than 10^8 line segments contacting pairs of devices and different segments of the circuit. This enormous number of wires is made possible by their small widths. Interconnect widths as small as $0.2 \text{ }\mu\text{m}$ are currently used in commercial circuits, and circuits and processes leading to smaller and smaller widths are continuously being developed (Figure 1.1 & Figure 1.2).

Since interconnects occupy a large fraction of the total area, reducing the average interconnect width allows an increase in the packing density of the devices in a circuit. Also, by reducing interconnect width (and therefore circuit dimensions), the transmission distances are reduced and thus operation speed can be increased. Consequently, there is tremendous incentive to produce designs with interconnects that carry higher and higher current density. During the operation of an IC, interconnects carry current densities as high as $5 \times 10^5 \text{ A/cm}^2$. In comparison, the maximum current density allowed for house wiring is of 10^2 A/cm^2 .

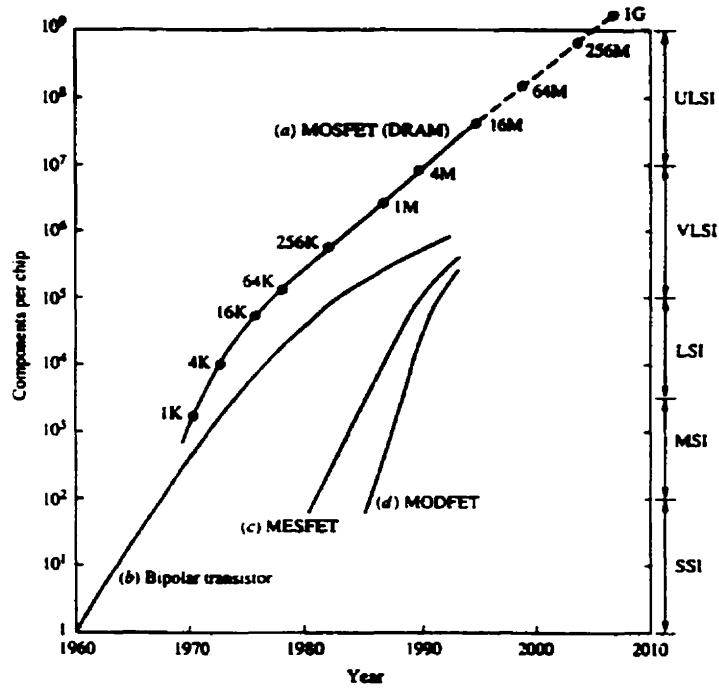


Figure 1.1. Exponential growth of the number of components per IC chip. (a), (b), (c) and (d) components per chip versus year for MOS, bipolar, MOSFET, and MODFET ICs, respectively [1, 2].

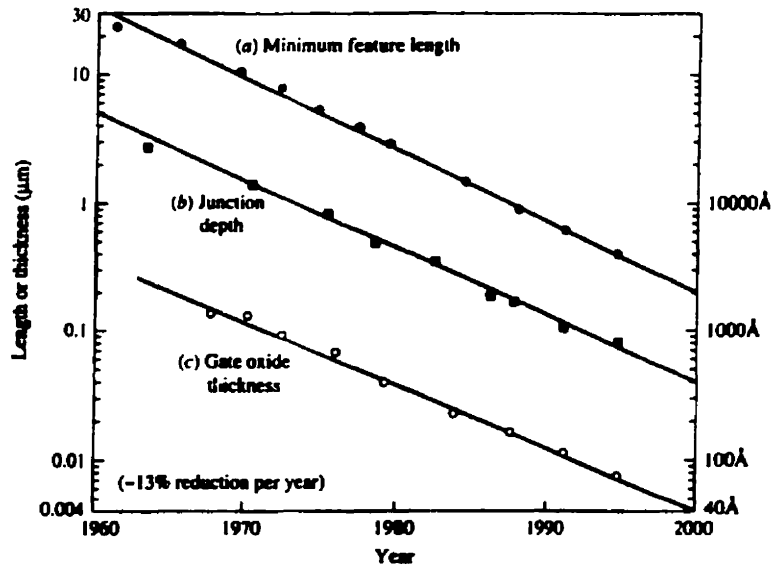


Figure 1.2. Exponential decrease of (a) minimum feature length, (b) junction depth, (c) gate oxide thickness of MOSFET [3].

Unfortunately, the ability to implement the designs that increase the packing density and the operation speed is currently limited by reliability concerns, such as electromigration-induced and stress-induced failures.

Aluminum has been used as a popular interconnecting material. An important mechanism of failure in aluminum interconnects is electromigration failure. Many factors influence electromigration lifetime of interconnects, including texture [4, 5, 6]. The texture in interconnects develops during such deposition processes as evaporation, sputtering, chemical vapor deposition, and electrochemical deposition; it also develops during the annealing of patterned wafers. In fact, it is rather difficult to deposit a sample without inducing texture. Recent studies show that the activation energy for electromigration is texture-dependant and that a strong {111} texture in aluminum interconnects improves the electromigration lifetime [7, 8]. Another important factor which causes failure of interconnects is the stress due to thermal expansion mismatch between the Al metallization layer and the Si substrate or the dielectric layer of SiO₂ [9, 10]. Not much work has been done to correlate the texture and stress-induced failures, although it is speculated that controlling the local orientation could minimize stress-induced failures [11].

Copper has recently been the new metallization material for ultra-large scale integration (ULSI) devices and electronic packaging due to its low electrical resistivity and good electromigration resistance [12, 13]. One of the disadvantages of copper as an interconnect material is that this element is easily oxidized at relatively low temperature. Unlike the oxidation of aluminum, the oxidation rate of copper is fast and no self-protective oxide layer forms to prevent further oxidation. The formation of oxide degrades the electrical and mechanical properties of copper as interconnection material. The study of copper oxidation kinetics and the development of means to prevent copper oxidation are important to the application of copper as an interconnection material in ULSI technology. Many researches have focused on the oxidation of copper in the 50's and 60's. It was found that copper oxidation is an

outward oxidation that is strongly dependent on oxidation temperature and oxygen partial pressure [14]. In the 90's, the study of copper oxides intensified due to the interest in using copper as an interconnection material. Some methods have been suggested to protect the oxidation of copper interconnects. One such method is passivating copper with a protection layer such as Si_3N_4 [15] and another one is adding alloying elements [16]. However, there has not been much work related to the influence of the texture and the microstructure of copper substrate and oxide on the oxidation kinetics of copper.

The main objectives of this study are:

- 1) to improve the understanding of the influence of texture on electromigration and stress-induced failures in Al interconnects.
- 2) to suggest a quantitative model to obtain optimum texture which would minimize the reliability concerns of Al interconnects.
- 3) to understand the oxidation kinetics of copper and the influence of substrate texture on oxide growth and suggest a method to reduce Cu oxidation.
- 4) to propose a quantitative model to correlate the texture of substrates with the oxide growth.

To understand the influence of texture on the reliability of thin film interconnects, it is necessary to review the basics on the texture and failure mechanisms of interconnects. In addition to a general review on texture, details on the reliability concerns are described in Chapter 2. A brief review on integrated circuit technology and metallization in integrated circuits is also provided in Chapter 2. Chapter 3 describes the techniques and the equipments used to characterize the texture and morphology of specimens, for example the texture goniometer, atomic force microscopy (AFM), orientation imaging microscopy (OIM) and so on. It is to note that a thermal gravimetric analyzer (TGA) was used for the study of copper oxidation. The results of the influence of texture on the reliability of Al interconnects are described in Chapter 4.

A quantitative model to obtain optimum texture, which minimizes the reliability concerns of aluminum interconnects, is presented at the end of Chapter 4. In Chapter 5, the influence of substrate texture on oxidation kinetics at 200°C is presented along with the model to correlate the texture of substrates with the oxide growth. Chapter 6 then presents the conclusion of the work, a list of the contribution to original knowledge, and recommendations for future work.

Chapter 2

Literature Review

This chapter consists of four sections. It starts with a review of the literature and terminology relevant to understanding texture. The second section provides a brief review of integrated circuit technology by giving a historical background of the evolution of integrated circuit (IC) technology and an introduction to the fabrication process of integrated circuits. The basic properties of a silicon wafer and processes of the wafer treatment are also described in this section. The following section covers more details on the IC manufacturing process and, in particular, on the metallization process. The last section describes the reliability concerns of metallization during the fabrication procedure and the actual use of IC chips.

2.1. A REVIEW OF TEXTURE

Many technically important materials such as metals and ceramics are polycrystalline. One of the most important quantities in describing the internal structure of a polycrystalline material is the distribution of its crystallites (grains). It is quite unusual for the grains in such materials to have a random distribution of orientation. Texture is a term used to describe the presence of preferred crystallographic orientations of the crystallites in polycrystalline material. Texture is developed at virtually all stages of the manufacturing process such as deformation, annealing, solidification, and phase transformation [17]. The mechanism of texture development is a very complex function of the mechanical and thermal processes as well as of the material itself. Texture plays a very important role in understanding the physical, chemical, and mechanical properties of materials, such as elastic modulus, Poisson's ratio, strength, ductility, toughness, magnetic permeability, and the energy of magnetization.

Various methods are used for describing texture. One standard method is using pole figures. The term 'pole' is defined as the normal to particular crystallographic plane, $\{hkl\}$. In a textured sheet, the poles, $\mathbf{n}_{\{hkl\}}$, from all grains are not evenly distributed in the specimen reference frame and cluster in certain directions depending on the crystal symmetry and texture. The $\{hkl\}$ pole figure represents the variation of $\{hkl\}$ pole density as a function of the pole orientation within the sheet reference frame. Pole orientation is usually specified by the azimuthal (β) and polar (α) angles of spherical-polar coordinate systems defined in the RD-TD-ND reference frame of the sheet where RD represents the rolling direction, TD is the transverse direction and ND is the normal direction. A specific pole density is then completely described as $P_{\{hkl\}}(\alpha, \beta)$. The standard presentation of the pole figure is a stereographic projection of the hemisphere of pole density data onto the RD-TD plane. Figure 2.1.(a) shows how the sheet is considered to sit at the center of the stereographic sphere. The orientation of a single grain in the sample can be represented by plotting its three $\{100\}$ poles at the appropriate angular positions relative to the reference directions and its stereographic projection, as shown in Figure 2.1.(b).

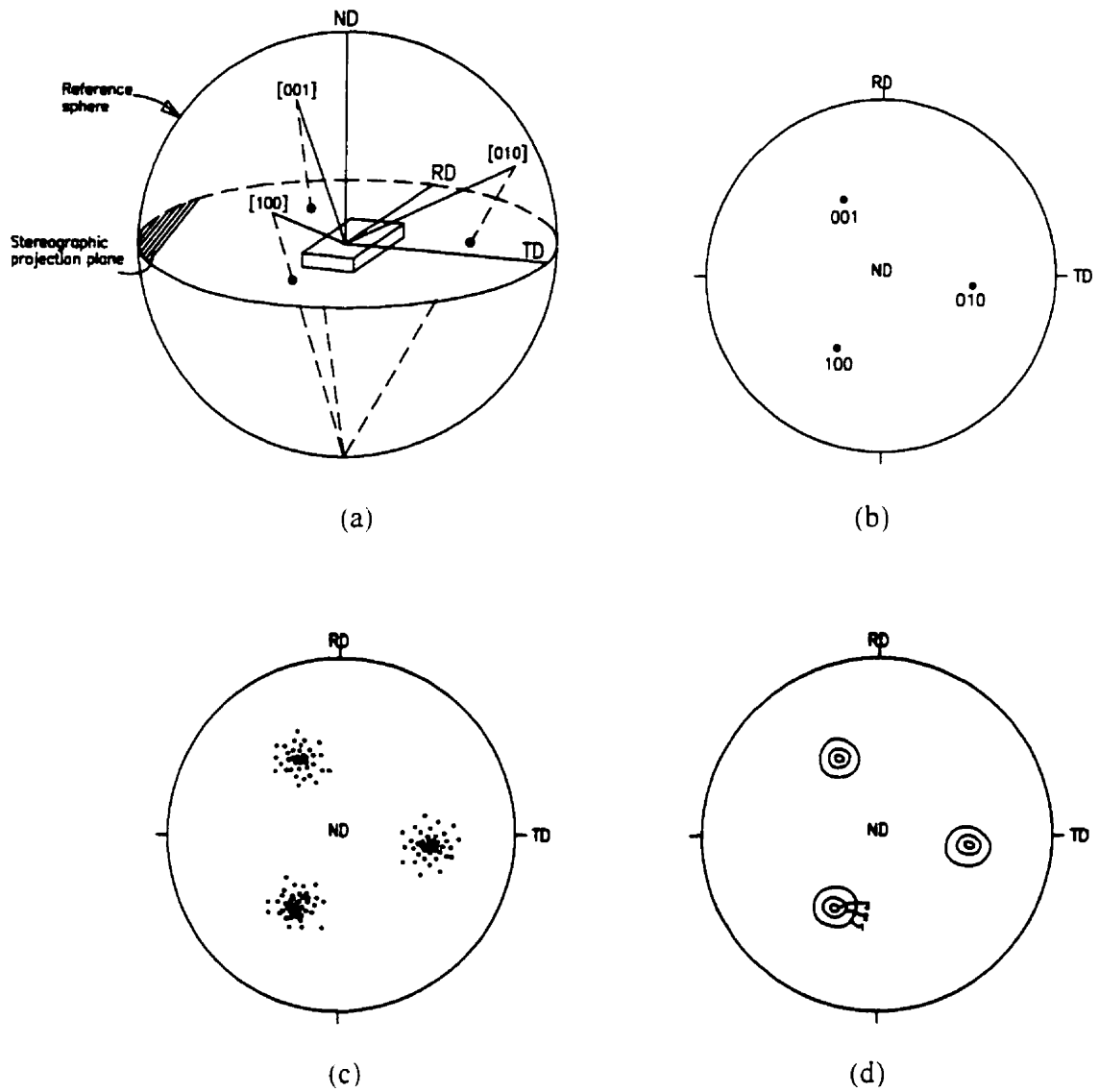


Figure 2.1. The presentation of pole figure: (a) projection sphere and reference frame of the sheet. (b) projection of poles for a single grain. (c) projection of pole from textured grains. (d) pole figure with iso-density contour lines [17].

For a polycrystalline sample, all grains must be considered and all of their respective $\{100\}$ poles must be plotted. The poles tend to cluster together in certain areas of the pole figure in textured materials as shown in Figure 2.1.(c). Iso-density contour lines connecting the projected data are usually plotted to produce the pole figure as shown in Figure 2.1.(d).

The fully quantitative method is based on a description of the orientation of crystallite. In order to describe the orientation of individual crystallites, a rotation g , which transforms a sample-fixed coordinate system into a crystal-fixed coordinate system, must be defined. Figure 2.2 shows both the sample-fixed coordinate system K_A and the crystal-fixed coordinate system K_B . In 1755, Euler introduced the "three rotation concept", one of the most widely used methods in describing the orientations of crystals. It is defined by assuming that, initially, the axes of the crystal coordinate system are parallel to those of the sample coordinate system.

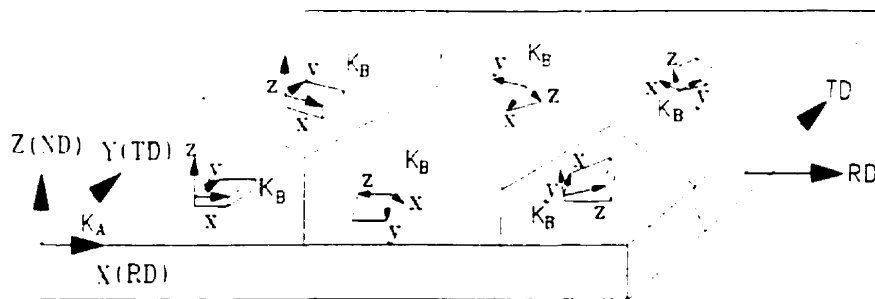


Figure 2.2. The sample-fixed coordinate K_A and the crystal-fixed coordinate system K_B in the sheet.

The Euler angles are then introduced by describing the rotation of one around the other. First of all, the crystal coordinate system is rotated around the Z' -axis through the angle φ_1 , then around X' -axis through Φ and finally around the Z' -axis again through the angle φ_2 as

illustrated in Figure 2.3.

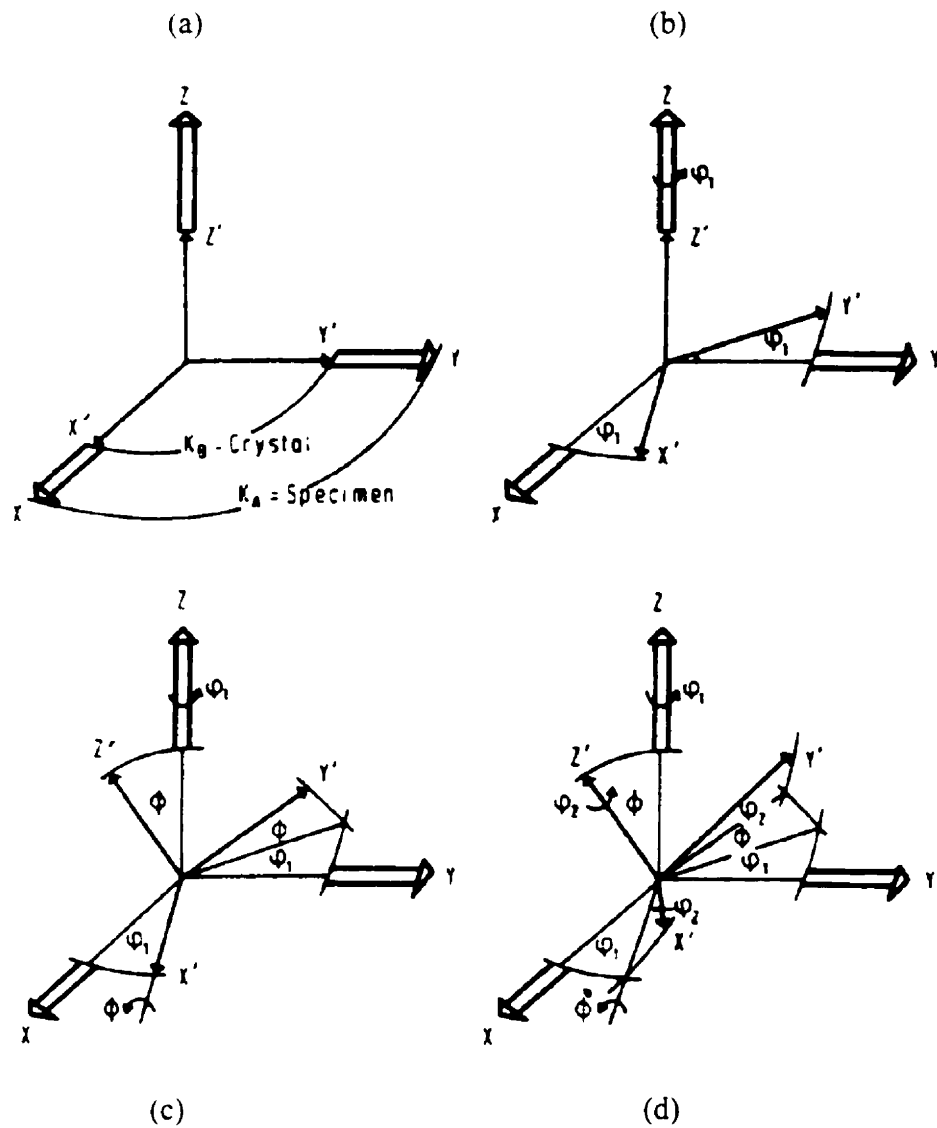


Figure 2.3. The definition of the Euler angle φ_1 , Φ , φ_2 : (a) the crystal coordinate system $K_B(X'Y'Z')$ lies parallel to the sample coordinate system $K_A(XYZ)$, (b) the crystal coordinate system is rotated around the Z' axis through the angle φ_1 . (c) the crystal coordinate system is rotated around the X' axis through the angle Φ . (d) the crystal coordinate system is rotated around the Z' axis through the angle φ_2 [18].

The rotation g is thus represented by the three Eulerian angles $\varphi_1, \Phi, \varphi_2$.

$$g = \{\varphi_1, \Phi, \varphi_2\} \quad (2.1)$$

All possible ranges of these Euler angles are as follows.

$$0 \leq \varphi_1 \leq 2\pi, 0 \leq \Phi \leq \pi, 0 \leq \varphi_2 \leq 2\pi$$

One of the standard methods used in quantitatively describing a texture is the orientation distribution function (ODF). The ODF is a statistical measure of distribution that describes the volume fraction of individual crystallites as a function of their orientation g . Assuming dV is the volume of all the elements of the sample that possess the orientation g within the infinitesimal range of orientation dg and that V is the volume of the entire sample, then the ratio dV/V defines the ODF function $f(g)$ by the equation (2.2) where dg is defined as equation (2.3).

$$\frac{dV}{V} = f(g)dg \quad (2.2)$$

$$dg = \frac{1}{8\pi^2} \sin \Phi d\varphi_1 d\Phi d\varphi_2 \quad (2.3)$$

A function $f(g)$ can be represented by the series of an expansion of generalized spherical harmonics [18, 19].

$$f(g) = \sum_{l=0}^{\infty} \sum_{m=-l}^l \sum_{n=-l}^l C_l^{mn} T_l^{mn}(g) \quad (2.4)$$

C_l^{mn} are constants quantifying the contribution of individual generalized spherical harmonics T_l^{mn} to the value of the function as a whole.

Depending on the lattice symmetry, the crystal reference system can be chosen among

several equivalent possibilities. In the case of a cubic system, there are 24 different representations for the same crystallite. These are related to one another by the rotations that form the rotational subgroup of the crystal symmetry. Each orientation g is associated with 24 symmetrically equivalent ones defined by 24 different sets of Euler angles. In addition to crystal symmetry, the sample can also exhibit elements of statistical symmetry. For example, a rolled sheet generally exhibits mirror symmetry in the planes defined by the sheet normal and rolling directions, and the sheet normal and transverse direction. Considering these crystal and sample symmetries, the generalized spherical harmonics T_l^{mn} can be summed into a linear combination and symmetrized to $T_l^{\mu\nu}$ and the limits of the m and n summation can be reduced. As a consequence, the equation (2.4) is modified to equation (2.5).

$$f(g) = \sum_{l=0}^{\infty} \sum_{\mu=-l}^{M(l)} \sum_{\nu=-l}^{N(l)} C_l^{\mu\nu} T_l^{\mu\nu}(g) \quad (2.5)$$

where,

$$T_l^{\mu\nu}(g) = \sum_{m=-l}^l \sum_{n=-l}^l A_l^{m\mu} A_l^{n\nu} T_l^{mn}(g) \quad (2.6)$$

The coefficients $A_l^{m\mu}$ and $A_l^{n\nu}$ are chosen to fulfill the crystal and sample symmetries, respectively, and the coefficients $C_l^{\mu\nu}$ are the coefficients of ODF that are symmetrized for the calculation of the texture of rolled sheet materials. Because the ODF is a function of the three Euler angles, it can be represented as a function defined at each point in a Cartesian space defined by the axes φ_1 , Φ , φ_2 . The Euler angles defining the ODF within a space are confined by $0^\circ < \varphi_1, \Phi, \varphi_2 < 90^\circ$. Figure 2.4 shows the ODF of the typical recrystallized ARMCO iron in the Euler space.

The ODF is also represented by one-dimensional plots of $f(g)$ along certain lines, called fibers, in the Euler space. The alpha fiber contains orientations where $\varphi_1 = 0^\circ$ and $\varphi_2 = 45^\circ$, while Φ changes from 0° to 90° . These orientations have their (110) crystallite directions parallel to the rolling direction (RD). The gamma fiber contains orientations where $\Phi \cong 55^\circ$, $\varphi_2 = 45^\circ$ and φ_1 goes from 0° to 90° . Orientations along the gamma fiber

have $\{111\}$ planes parallel to the sheet of the plane. The eta fiber contains the orientations where $\varphi_1 = 0^\circ$, $\varphi_2 = 0^\circ$ for the range of $0^\circ < \Phi < 90^\circ$. The (100) directions along the eta fiber are parallel to the rolling direction. The $\varphi_1 = 0^\circ$ and $\varphi_2 = 0^\circ$ sections of the ODF are generally used to describe these fibers and some other important orientations. Figure 2.5 shows α , γ , and η fibers and some low index orientations on the $\varphi_1 = 0^\circ$ and $\varphi_2 = 45^\circ$ sections of the ODF.

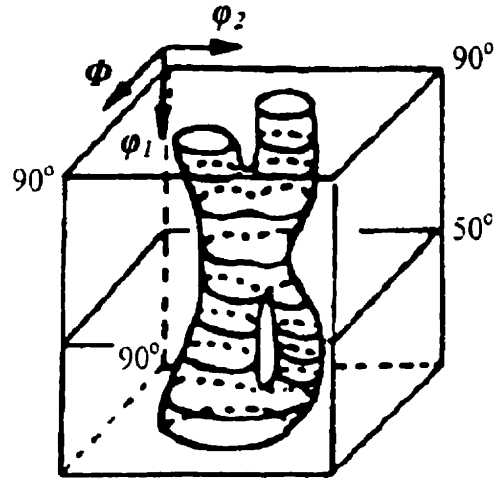


Figure 2.4. The ODF of the typical recrystallized ARMCO iron.

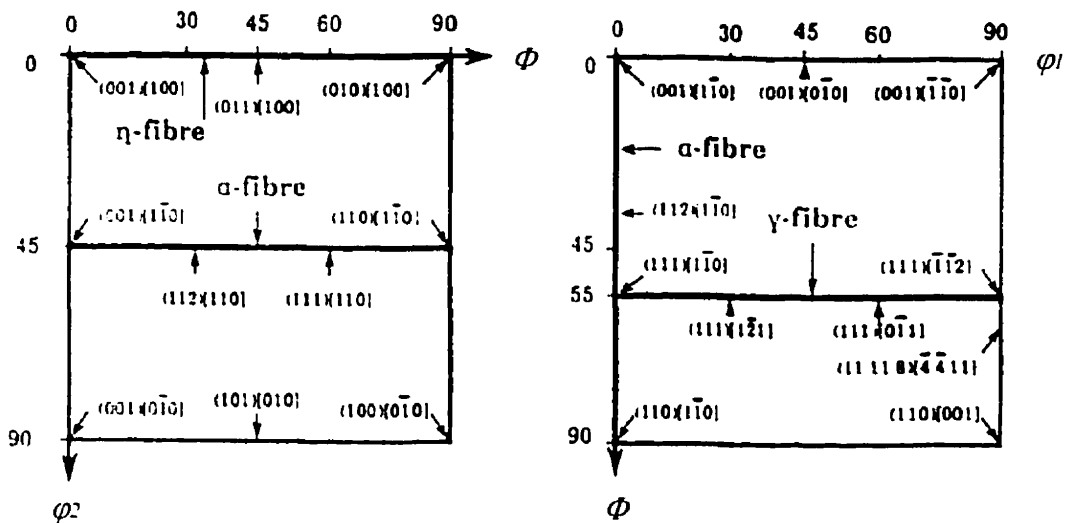


Figure 2.5. Location of fibers and some low index orientations on the (a) $\varphi_1 = 0^\circ$, (b) $\varphi_2 = 45^\circ$ sections of the ODF.

2.2. INTEGRATED CIRCUIT (IC) TECHNOLOGY

2.1.1. Historical Background

The microelectronics industry began in 1947 with the invention of the transistor by Bardeen and co-workers [20]. The planar silicon technology had developed in the late 1950s and this enabled active devices, such as transistors, and passive devices, such as resistors, to be integrated on the same silicon substrate. Since then, the growth has been remarkable, with the number of components, which can be accommodated on a single silicon integrated circuit virtually doubling every year [21]. The result is that microelectronic devices, which not so long ago were concentrated in the domain of expensive specialized equipment, now form the basis of a whole range of products which are widely available in the street. Advances in microelectronics have had a major impact on the size and cost of computer hardware. The continually increasing capacity of semiconductor memories has resulted in cheap, efficient means of accessing and storing large amount of information, whilst the ability to integrate a central processing unit on a single chip has resulted in completely new industries based around personal and home computers. The information technology revolution, which is now occurring, compares with previous industrial revolution and threatens to have a major social, commercial and political impact on the way we live.

The 1947 discovery that led to the invention of the transistor occurred was somewhat accidental. John Bardeen and Walter Brattain [20] of the Bell Telephone Laboratories were investigating the potential distribution in the vicinity of the rectifying contact associated with point contact 'Cat's Whisker' diodes. To do this, they placed another contact on the surface close to the 'Cat's Whisker' and noticed that the signal which appeared at this contact was an amplified version of the original signal. A fellow scientist, Shockley [22], at Bell Telephone Laboratories refined the operation principles of this 'transfer resistor' or 'transistor'. The term 'transfer resistor' refers to the transfer of current from a forward biased circuit with a low resistance to a reversed biased

circuit with a high resistance. This transfer of current enabled the transistor to be useful again. The three Bell Laboratories' workers later shared the Nobel Prize for their discovery.

The concept of the integrated circuit was first proposed by Harwick Johnson of the RCA Corporation and was later extended by Dummer of RRE (now the Royal Signals and Radar Establishment) in the UK. The first commercial devices appeared in the early 1960s because of the subsequent US Government funding for research and development in the emerging semiconductor companies. It was in fact Fairchild Inc. that conceived the planar technology from which today's integrated circuits have developed. The growth of the electronics industry has been extremely rapid following this development. Initially, the drive was concentrated on applying this new technology to military systems under funding from the US Department of Defense, with commercial manufacturers of computer and communications equipment preferring to use hybrid circuits built from discrete components. This emphasis started to change towards the end of the 1960s when companies such as DEC recognized the importance of incorporating complete digital functions on a single chip. This led to the development of a whole series of relatively cheap microcomputers and paved way for the commercial exploitation of microelectronic technology. The processing of ICs advanced rapidly and the exponential increase in transistor count per chip during the two decades (1959-1979) followed fairly closely Gordon Moore's prediction of 1960s, in which he forecast that the function density per chip would double every year [21].

Until the late 1960s, the microelectronics industry was dominated by bipolar technology. Metal-Oxide-Semiconductor (MOS) technology did not really emerge until later because of material problems associated with making high quality gate oxides. MOS has become the primary technology for fabricating integrated circuits because of its intrinsic low power consumption, moving from a small percentage (12%) of all ICs manufactured in 1982 to 82% by 1996. Bipolar ICs are reserved for special applications, which demand their superior speed. The success and evolution of MOS

are directly the result of intense industrial competition, particularly in the US and Japan, to increase the capacity of semiconductor memory circuits.

The growth of microelectronic industries over the last two decades is more dramatic. In the early 1970s, sales of ICs reached \$ 1 billion; in the year 2000, digital MOS ICs are projected to dominate a market worth about \$ 100 billions. Likewise, the broader market for electronic equipment is expected to climb up to near a trillion dollars (Figure 2.6). The number of component per IC chip has been increased dramatically, too. Commercial chips with less than $0.2 \mu\text{m}$ of their minimum device size and with more than 10^8 devices per chip are produced these days.

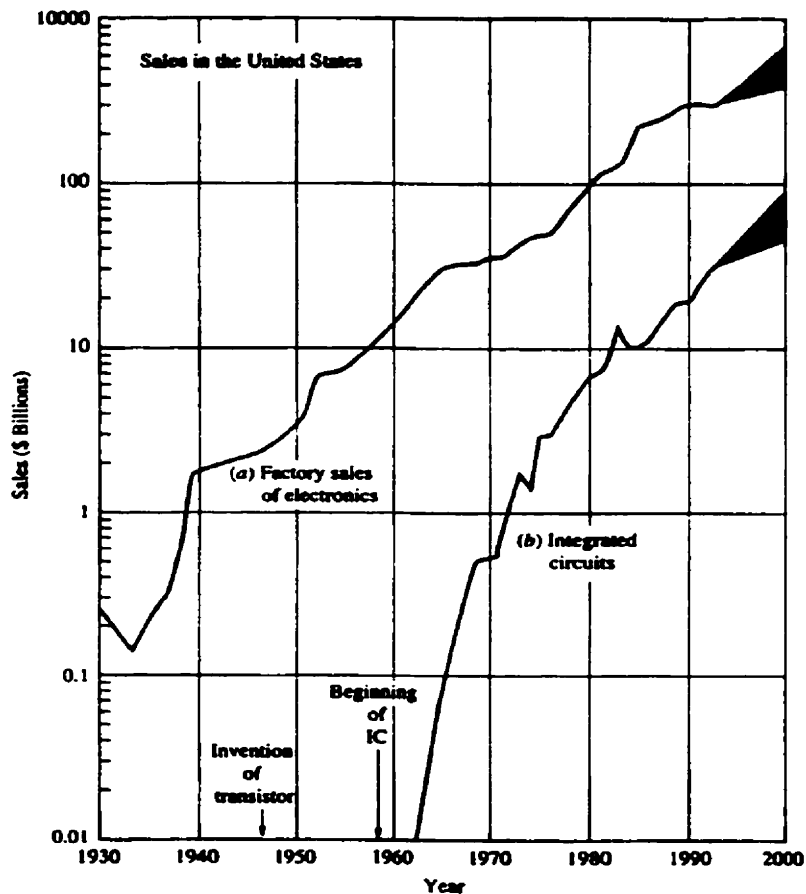


Figure 2.6. Sales of electronics in the United States.

(a) Factory sales of electronics, (b) Integrated circuit market [23, 24].

2.2.2. Fabrication Process of Integrated Circuit

The fabrication of integrated circuits is now a well-established process, and even though developments are still taking place, the basic processes are not changing greatly. Figure 2.7 shows a brief IC manufacturing process flow.

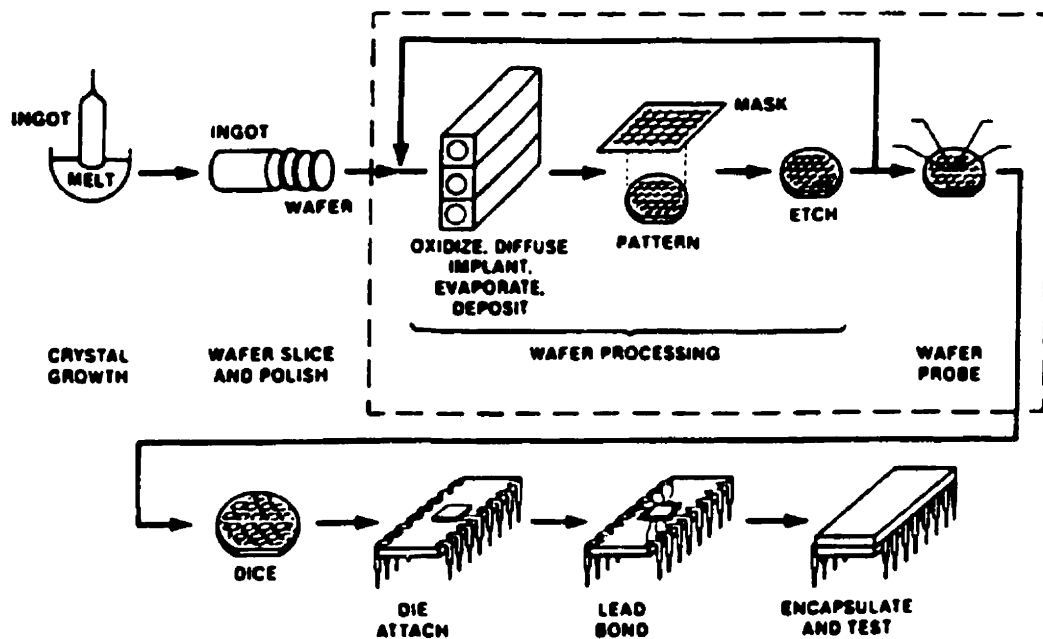


Figure 2.7. Integrated circuit manufacturing process flow [25].

The main semiconductor is silicon while gallium arsenide (GaAs) is being used increasingly for very high-frequency applications. The production of silicon is usually separate from the manufacture of integrated circuits, and the majority of IC manufacturers purchase the silicon in the form of wafers some 100-200 mm in diameter.

These wafers are approximately 1 mm thick, are highly polished and are ready for processing. A wafer may be n-type or p-type depending on whether the silicon has been doped with n-type or p-type elements during the production process. The most commonly used dopant elements for silicon are boron for p-type wafers, and phosphorus or arsenic for n-types. These dopant elements are distributed uniformly throughout the thickness of the wafer and the amount determines the resistivity of the silicon. The more elements are present, the lower the resistivity, and vice-versa. One of the major advantages for the use of silicon in fabricating ICs is its ability to grow a natural oxide (silicon dioxide). Silicon dioxide (SiO_2) is a good dielectric with a relatively high dielectric constant (~ 4), and high breakdown voltage. It is also impervious to the ingress of moisture and it acts as a barrier to the diffusion of impurities. Silicon dioxide is formed by heating the silicon wafer in an atmosphere that contains either oxygen or water vapor. This takes place in a furnace inside a quartz tube at the temperature between 1100°C and 1200°C and may take a few minutes to many hours depending on the thickness of oxide that is required. Oxide thickness may range from 50 nm for the gate oxides for MOS transistors, to $1.5\ \mu\text{m}$ for oxide isolation regions where the increased thickness reduces interelectrode capacitance between the metal interconnections and the silicon substrate, which forms a ground plane.

To construct devices and circuits on the surface of the silicon wafer, the transfer of the layout pattern onto the wafer is required. The patterns describe the location of further doping, insulating layers, metal interconnections, etc. The build-up of a functional circuit requires the definition of many such layers on top of each other. The layer patterns are usually computer generated, based on the position and interconnection of the basic building blocks in the circuit. The alignment of one layer on top of the other is of crucial importance to the success of the circuit fabrication.

In order to transfer the layer patterns on to the wafer, the first step is to transfer each pattern onto an actual-size plate that consists of areas that are transparent and opaque. These plates are called masks and usually consist of a glass plate with the pattern

defined in a metal layer. Where metal is present, the area is opaque, and where there is no metal, the mask is transparent. The next stage is to cover the entire wafer with a chemical layer in which the pattern will be transferred from the mask. The chemical is sensitive to light and is called photoresist; it is an organic material with chains of molecules. When exposed to light, the resist either polymerizes, making even longer chains of molecules and hardening, or the molecules break up and the material softens. These two types of resist are termed negative and positive respectively, and require inverse mask patterns to provide the same pattern of resistive layer. Whether positive or negative, the photoresist comes in a liquid form. After the application of light through the mask, the soft areas of resist have to be washed away. This leaves just the polymerized areas of resist protecting certain areas of the wafer. In order that the remaining resist can withstand the next processing stage such as doping and etching, the resist is thoroughly dried and hardened by baking in a furnace. Once the subsequent process has been completed and the resist has served its purpose, it is stripped away. The brief process of photolithography is illustrated in Figure 2.8.

The basic wafer can have a certain amount of dopant introduced into it at the purification and crystallization stage, and higher-doped active layers can be obtained by providing a thin epitaxial region on the top of the basic wafer. However, these processes are global, in that the entire wafer is doped. For certain parts of the process, it is required that areas are selectively doped in conjunction with the photolithography process. As photoresists cannot usually tolerate the high temperature in which the doping process is performed, the 'protection' layer must be a dielectric layer. Dopant elements may be added at several points in the IC manufacturing process. As mentioned before, the most commonly used dopant materials for silicon are boron for p-type wafers, and phosphorus or arsenic for n-type wafers. There are two basic approaches for introducing the dopant material into the wafer, diffusion and ion implantation.

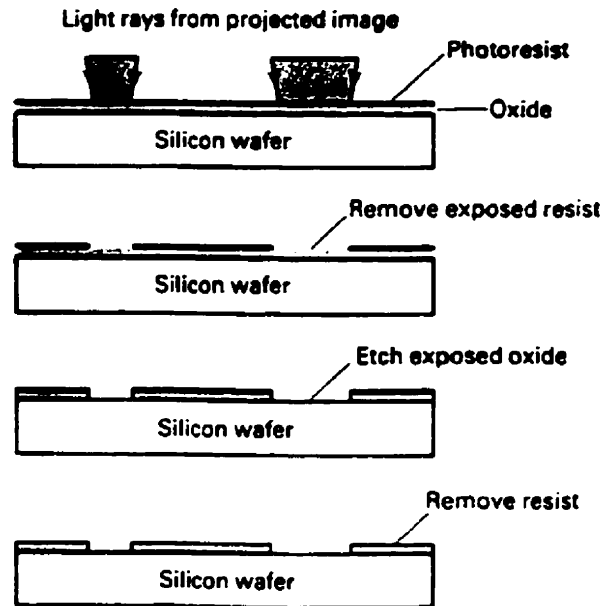


Figure 2.8. Stages in photolithography [26].

Diffusion is the original process by which all selective doping used to be introduced. The basic approach is to expose the area to be doped to a source of the dopant material, and then by elevating the wafer to high temperatures, the material diffuses into the semiconductor. The diffusion can either be done in a one-stage process or a two-stage process, the latter being used more popularly to achieve maximum control. A two-stage process consists of a lower temperature 'deposition' stage, after which the dopant source is cut off, followed by a higher temperature 'drive-in' stage. The first of these stages is termed continuous source, as a fresh supply of the dopant is continuously available. The second is termed limited source, with which the desired depth of diffusion is achieved. These two diffusion processes are used at different stages of IC fabrication depending on the profile requirements of the various doped areas. Diffusion takes place in temperature-controlled furnaces and the normal temperatures for diffusion are typically 1000°C-1400°C. The dopant material must be introduced in a

gaseous form, although the original source of the dopant may be of solid, liquid or gaseous form. An example of the diffusion system is shown in Figure 2.9.

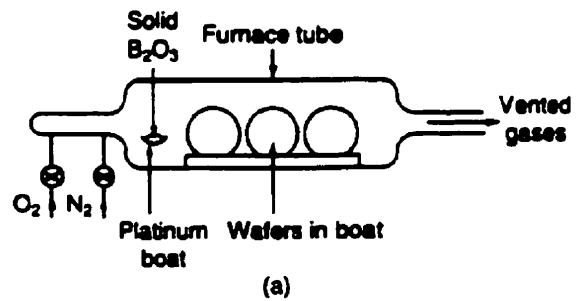


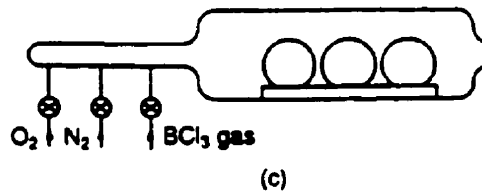
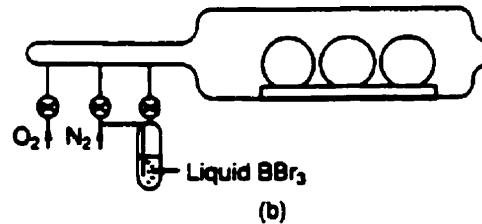
Figure 2.9.

Boron diffusion system.

(a) Solid diffusion source system.

(b) Liquid diffusion source system.

(c) Gaseous diffusion source system [27].



Ion implantation is increasingly being used to introduce impurities into silicon. The wafers are placed at the end of an acceleration tube in a high vacuum and ions are accelerated and directed to the wafer. The high kinetic energy of these atoms means that they can penetrate into the surface of the semiconductor. The faster they are 'shot' at the wafer, the deeper they will penetrate, so control of the doping profile is achieved by the speed of the dopant material. The mechanism for 'shooting' the dopant material is to accelerate it through an electric field. To do this, the material must be charged. As such, this process is termed ion implantation since the dopant material consists of charged ions. Figure 2.10 shows a brief schematic system of the ion implantation. As the implanting effect will cause much mechanical damage to the surface region of the

wafer. it is necessary to pass the wafer through an annealing process. This consists of raising the wafer to a temperature of around 600°C . and this has two effects. Firstly, the semiconductor wafer can re-align its crystal structure back to the single crystal, which is important for efficient device operation. Secondly, it allows the dopant material to fit substitutionally into the crystal lattice. The great advantage of ion implantation over the diffusion process is that the former is a low-temperature process, so unwanted diffusion of impurities is greatly restricted. Another advantage is that dopant materials can be penetrated through a thin oxide. Either n-type or p-type dopants can be implanted through the gate oxide. Thus, by means of ion implantation, it is possible to fabricate several different types of MOS transistors on the same wafer. However, the ion implantation equipment is much more expensive than a diffusion furnace system, and as the operation has to be performed in an evacuated system, the throughput of wafers is very low.

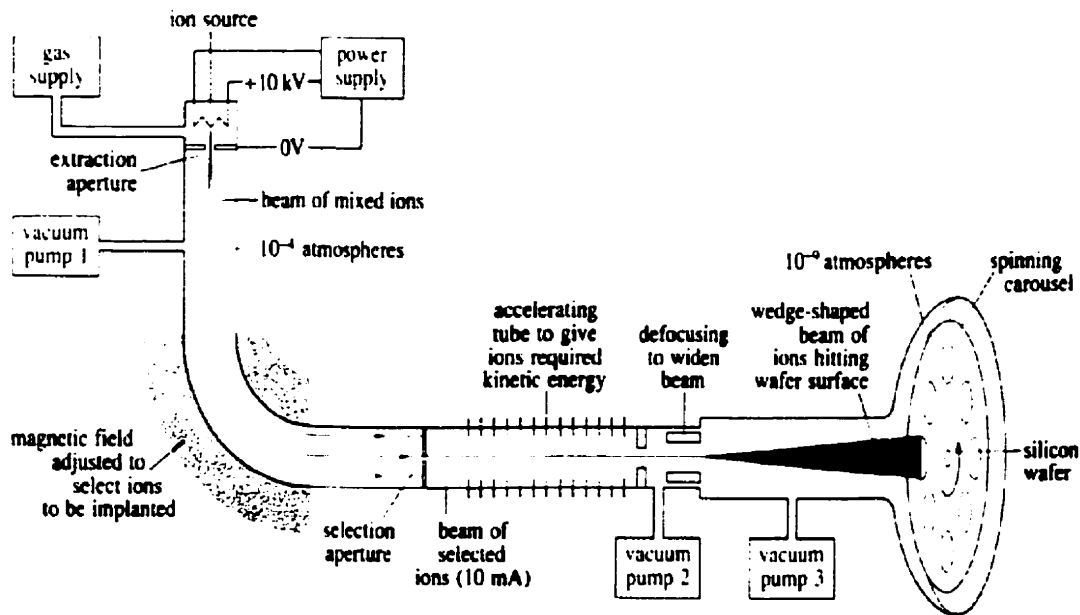


Figure 2.10. Ion implantation system [28].

The processes on fabricating silicon wafer have been explained so far. The next step in the IC manufacturing process is the formation of the metal interconnects. When all the high temperature steps have been completed and when all the silicon is once again fully covered with oxide, a photolithography step is used to create windows in the oxide to form contacts. The complete surface of the wafer is then covered with a thin layer of metal and photolithography is again used to define the metal tracks and to allow the surplus metal to be removed. This process is repeated to obtain multi-layered circuits. Details of this process, dubbed metallization, are explained in the following section.

As the final step of chip fabrication has been completed, each individual chip, also called a die, is cut from the wafer. This die is then mounted in a package that normally consists of a frame with a number of metal leads connected to 'legs', which will form the connections that can be soldered on to the circuit board. Once the electrical contacts are completed, the chip is hermetically sealed into the package to provide a further layer of protection from contamination or mechanical stress that may cause premature failure of the device. The usual forms of the packaging are a plastic compound that is molded around the bonded chip, or a ceramic package that is more expensive but provides better stability and greater thermal range. The packaged chip goes to a test line in which defective products are screened and eliminated.

2.3. METALLIZATION FOR THE INTEGRATED CIRCUITS

Metals have been known to carry electric currents from the source of its generation to the point of its use. In microelectronics, metals are basically used in a similar fashion as a means of supplying power and transmitting information from one place to another. The application of metals and metal-like layers during integrated circuit fabrication is called metallization. As microelectronics technology progressed from the sixties to the nineties, the demand on the properties of useful thin films as interconnection layers and their materials has progressively increased. This trend is expected to continue into the twenty-first century. Such demands are reflected not only in the fundamental characteristics of the thin-film materials but also in their processing. Thus the demands on the progressive integrated circuit and on microelectronics technology are also placed on metallization. At the present time the development of new metallization schemes has become the key to the success of continued miniaturization of devices and circuits and also to the success of three-dimensional devices and circuits in the future.

Figure 2.11 shows a cross section of a metallization scheme of a typical metal-oxide-semiconductor field effect transistor (MOSFET). The central region is called the *gate*. In this region, the substrate silicon is isolated from the metal electrode by an insulation layer, a *dielectric layer*, which is generally a thin thermally grown SiO_2 . The metal electrode, generally a heavily doped polysilicon layer that serves as a metal, is called *gate electrode*. It controls the on-off working properties of the MOSFET. The two regions adjacent to the gate region are called the *source* and the *drain*. All metals involving direct contact with the semiconductor surface are called *contacts*. The structure of integrated circuits used for electronics these days is much more complicated than the structure shown in Figure 2.11. Figure 2.12 shows a schematic of a cross section of a multilevel metallization structure. It has five metal layers with tungsten plugs (W1-W4), which connect different level of metal layers. This plug is also called *via*. Interlevel dielectric layers (ILD1-ILD4) are used to electrically isolate one level of

metal interconnects from another. The chip will be connected to a package through solder bumps or wire bonds.

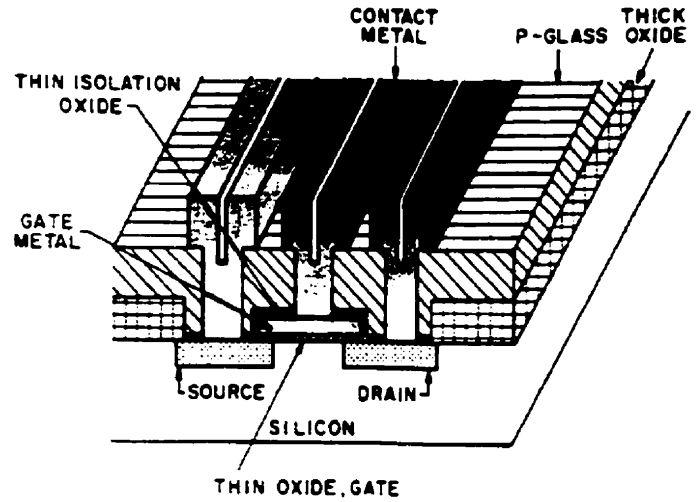


Figure 2.11. Schematic cross section of typical MOSFET [29].

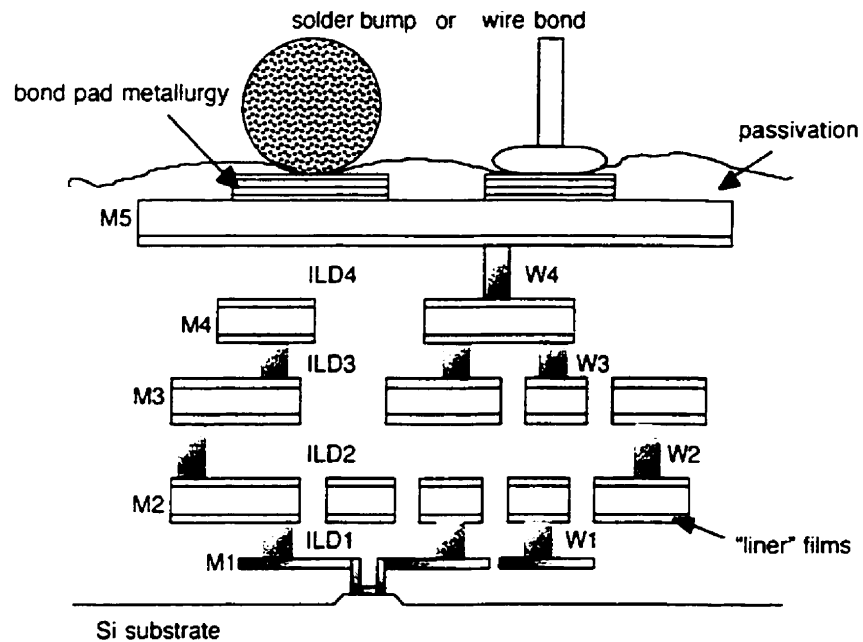


Figure 2.12. Schematic cross section of a multilevel metallization structure [30].

There are a variety of requirements for any metallization scheme to satisfy when used for integrated circuits. It supposes to have low resistivity and good adherence to silicon and silicon oxide. It must be easy to form and etch. It should be stable throughout oxidizing and other processing, especially it must not react with packaging materials or the wires used for bonding. Additional properties are required for the metallization used in power devices and circuits operate at temperature as high as 250°C. At such temperature metallurgical reaction can readily occur. Therefore, the most important requirement is the stability of the metallization throughout the IC fabrication procedure and during the actual use of the finished product. For better stability, metallization does not interact with other contacting materials and must have strong resistance to electromigration and thermal stress induces failures such as voids and hillocks. More specific requirements of the various metallization such as contacts, gate metal, interlevel interconnects and via filling metals are listed in Table 2.1. It should be pointed out that these requirements of the metallization are not fulfilled yet. A lot of research and development has been done to satisfy these requirements.

Table 2.2 shows some of the metallization schemes that are being used and being investigated. As mentioned before a heavily doped polysilicon is used as gate material. Aluminum or silicide is usually used for this purpose. Aluminum or aluminum alloys are the most popularly used as interconnecting materials. Recently, copper is being substituted for aluminum because of its low electric resistivity. Tungsten, aluminum or copper is usually used as the materials for *via*, however, tungsten is the most popular among those. Interconnecting materials, such as aluminum and copper, are readily diffuse to dielectrics especially at high temperature. Therefore, a certain layer is necessary to prevent a metallurgical or chemical reaction that might lead to electrical failure in the circuit. TiN, TiW, TiC, Ta or TaN is commonly used as a diffusion barrier.

Table 2.1. Specified requirements for the various metallization.

Metallization	Requirements
Gate Metal	Low resistivity Stability throughout high temperature processes No needs for diffusion barrier when contacting with upper level of metals
Contact Metal	Low contact resistance High electromigration resistance No/minimum consumption of silicon No interaction with oxide wall No needs for diffusion barrier when contacting with upper level of metals
Metal Interconnects	Low resistivity High resistance to electromigration and stress Compatible, chemically and electrically, with the dielectric
Via Fill Metal	Low contact resistance with underlying and over layer metal Planarizable Low resistivity

Table 2.2. Metallization schemes being used for IC fabrication.

Application	Metallization
Gate Metal	Doped polysilicon with or without silicide (WSi ₂ , TiSi ₂ , CoSi ₂) on top
Contact Metal	Al. Silicide (CoSi ₂ or TiSi ₂)
Metal Interconnects	Al or Cu
Via Fill Metal	W, Al or Cu
Diffusion Barrier	TiN, TiW, TiC, TaN, Cr or Ta

Metals are deposited by a variety of techniques but principally by physical vapor deposition (PVD) or by chemical vapor deposition (CVD). The most common forms of PVD are evaporation, e-beam evaporation, plasma spray deposition and sputtering. Evaporation and e-beam evaporation were used extensively in earlier generations of medium scale integration (MSI) and large scale integration (LSI). 1960s - early 1970s, but have since been replaced by sputtering. Sputtering is the most popular deposition technique being used for the IC fabrication these days. Sputtering prevailed over other techniques because of (1) high deposition rate, (2) the capability to deposit complex alloy compositions and refractory metals, (3) the capability to maintain well-controlled, uniform deposition on wafers, and (4) the capability, in multichamber system, to clean the contact before depositing metal. No other deposition technique can offer all of these advantages for Al alloys and contact metals.

Sputtering takes place in a vacuum chamber as shown in Figure 2.13. The mechanism of sputtering is quite simple. The argon (Ar) plasma is introduced into the chamber, which contains the wafers and the target. The particular material to be sputtered is made into a disc that is thermally bonded to the cathode. The Ar ions from plasma are charged positively while the target is maintained at a negative potential. The positive ions accelerate towards a target, lead to an impact, and knock off some of the target atoms. The ejected atoms fly through the plasma and land on the wafer. The Details of basic sputtering techniques can be found in Refs. 31 and 32. Quite a large amount of power is supplied to the Ar plasma to maximize the sputtering rate (in the range of 3kW to 20kW). Most of momentum of the Ar ions transfers to the target, which needs to be cooled through thermal contact with the cathode. Usually, the cathode is water-cooled.

A number of metals and metal compounds can be deposited by chemical reaction or thermal decomposition of precursors. In the CVD method, a chemical (in the gaseous state) containing atoms of the material to be deposited is introduced into the system reaction chamber. The desired material can be formed as a nonvolatile solid film on a substrate by the reaction of the chemical with another vapor-phase chemicals. Usually

the wafer needs to be heated to 100 to 800°C to provide the initial thermal energy to overcome the reaction barrier. CVD metal can also be deposited in plasma [33]. The advantage of plasma decomposition is that the energy required to overcome the initial reaction barrier can be supplied by the plasma, and the deposition temperature can be reduced. This reduction is especially important for metal or metal compounds used for vias and multilevel interconnects since their tolerance for high temperature is limited. CVD techniques for depositing Al, Cu, WSi_2 , TiN, and W, have all been developed and applied to devices and/or prototype circuits [34 - 38]. However, except for WSi_2 used on top of gate polysilicon and W used as a contact plug, CVD metals are not widely used yet because of immature process and equipment development. The techniques of film deposition are being challenged everyday. Lots of efforts have been done to improve the deposition process and the equipment.

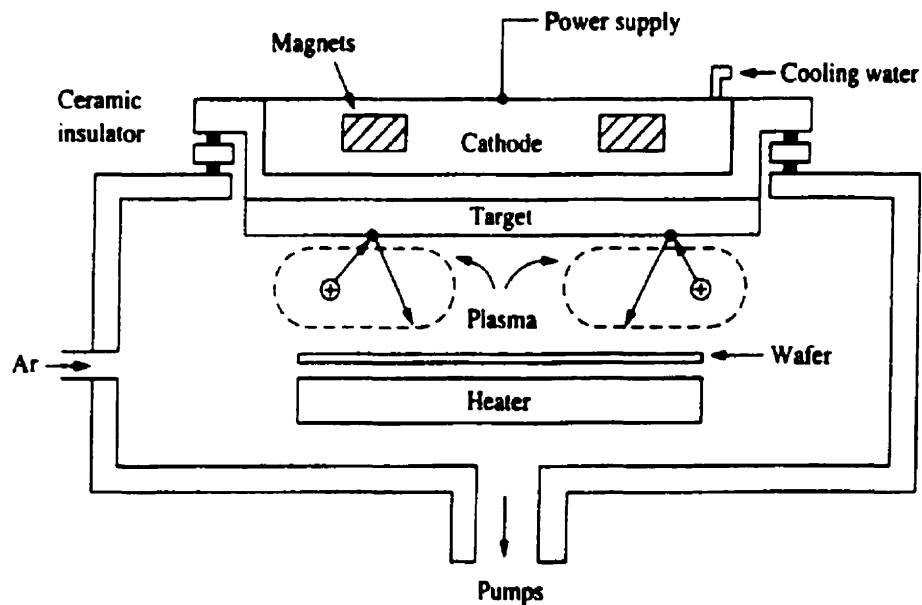


Figure 2.13. Schematic of simplified dc-magnetron sputtering system [3].

2.4. RELIABILITY CONCERNS IN METALLIZATION

In modern electronics industry, the progress is usually measured by how small you can make a device and how many devices you can fit onto a single chip. Since interconnects occupy a large fraction of the total area, reducing the average interconnect width allows an increase in the packing density of the devices in a circuit. Also, by reducing interconnect width (and therefore circuit dimensions), the transmission distances are reduced and thus operation speed is increased. Consequently, there is tremendous incentive to produce designs with interconnects that carry higher and higher current density. Unfortunately, the ability to implement these designs is currently limited by reliability concerns. *Reliability* is a measure of failure-free operation of a component or circuit under a set of stated operating conditions. It is not a precise measurement of how long the component will operate but, rather, a measure of the probability of successful operation over a recognized period of time. All devices, whether electrical or mechanical, have a finite lifetime. For an integrated circuit the lifetime is closely related to the manufacturing process plus its final operating conditions. In this section, some important reliability concerns in metallization such as electromigration-induced failures and stress-induced failures are explained. A discussion of overall product reliability and performance reliability is described in various sources [3, 39, 40].

2.4.1. Electromigration in Thin Films

Electromigration is the migration of metal atoms along metallic conductors carrying large direct current densities. This phenomenon was observed in liquid metal alloys well over a century ago and is the primary mechanism responsible for the failure of tungsten light-bulb filaments. Bulk metals approach the melting point when powered with current densities (j) of about 10^4 A/cm². On the other hand, thin films can tolerate densities of 10^6 A/cm² without immediate melting or open-circuiting because the Joule heat is effectively conducted away by the substrate, which behaves as a massive heat

sink. In a very large scale integrated (VLSI) circuit chip containing several million devices, these are connected by polycrystalline aluminum interconnects that are typically less than 1 μm wide and 1 μm thick. Under high current densities, mass-transport effects are manifested by void formation, hillocks, cracked dielectric film overlayers, grain boundary grooving and thinning near the contacts. Generally, open circuiting terminates the life of the conductor. For these reasons, electromigration has been recognized as a major reliability problem in integrated circuit metallizations. The model of electromigration damage in thin films is illustrated in Figure 2.14.

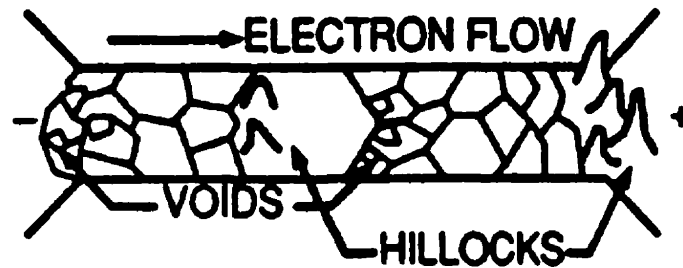


Figure 2.14. Model of electromigration damage in a thin film strip [39].

At a fundamental level, electromigration involves the interaction between current carriers and migration atoms. The mechanism of this interaction is not entirely understood, but it is generally accepted that electrons streaming towards the anode through the stripe can impart sufficient momentum to metal atoms upon impact to propel them into neighboring vacant sites. Thin film damage is caused by a depletion or accumulation of atoms, which is defined by either a negative or positive value of dC/dt , respectively. For one-dimensional diffusion, the value of dC/dt can be written as,

$$\frac{\partial C}{\partial t} = -\frac{\partial}{\partial x} \left(\frac{CDZ^* q \rho J_e}{RT} \right) - \frac{\partial}{\partial T} \left(\frac{CDZ^* q \rho J_e}{RT} \right) \frac{\partial T}{\partial x} \quad (2.7)$$

where C is the concentration of the diffusing atoms (atoms/cm³), D is the diffusivity of the atom, R is the universal gas constant, T is the absolute temperature, q is the fundamental charge, ρ is the resistivity of the metal, J_x is the current density, and Z^* is an 'effective charge', which is usually empirically determined for polycrystalline films. When $dC/dt < 0$, mass depletion occurs and voids form. On the other hand, mass accumulates in hillocks when $dC/dt > 0$. The first term on the right-hand side reflects the isothermal mass flux divergence due to film structure while the second term represents mass transport in the presence of a temperature gradient. The resulting transport under these distinct conditions can be qualitatively understood with reference to Figure 2.14, assuming that the atom migration is confined solely to grain boundaries and in the direction to the anode. Let us first consider electromigration under isothermal conditions. Because of varying grain size and orientation distributions, local mass flux divergences exist throughout the film. Each cross section of the strip contains a lesser or greater number of effective grain boundary transport channels. If more atoms enter a region, such as a junction of grains, than leave it, a mass pile up and growth can be expected. A void develops when the reverse happens. At highly heterogeneous sites, where, for example, a single grain extends across the strip width and neighbors numerous small grains, the mass accumulation and depletion is accelerated. For this reason, uniform grain size distribution is desirable.

In addition to the influence of microstructure, there is the added influence of the temperature gradient due to non-uniform temperature distribution that develops at various sites within device structures. The resulting damage pattern can be understood by considering the second term on the right-hand side of Equation (2.7). As shown in Equation (2.7), all terms in parentheses are positive and $Cq\rho J_x/RT$ is roughly temperature-independent, whereas DZ^* increases with temperature. Therefore, dC/dt varies as $-dT/dx$. Voids will thus more likely form at the negative electrode, where $dT/dx > 0$, and hillocks will grow at the positive electrode, where $dT/dx < 0$. Physically, the drift velocity of atoms at the cathode increases as the temperature increases. Thus,

more atoms then exit the region than flow into it. At the anode, the atoms decelerate in experiencing lower temperatures and thus pile up there.

The reliability of a metal interconnect is most commonly described by a lifetime experiment on a set of interconnect lines to obtain the median time to failure (MTF). The data for the actual time to failure of each line are plotted on a lognormal graph, and the value of T_{50} (time for 50% of the lines to fail) is extracted. The stress experiment involves stressing the lines at high current densities (usually from 10^6 to 3×10^6 A/cm²) at temperatures ranging from 150 to 250°C. The failure criterion is typically an electrical open for nonbarrier (non-passivated) interconnect lines or about a 20% increase in line resistance for barrier (passivated) lines. Analysis of extensive accelerated testing that has been performed on interconnections has led to the following general relationship between film median time to failure (*MTF*) and the current density, J_c [41]:

$$MTF^{-1} = AJ_c^n \exp\left(-\frac{E_a}{kT}\right) \quad (2.8)$$

As with virtually all mass-transport-related reliability problems, damage is thermally activated. For Al thin films, the metal-dependent constant n is typically 2 to 3, and E_a , the activation energy for electromigration failure, ranges from 0.5 to 0.8 eV [42], depending on the grain size. In contrast, an energy of 1.4 eV [43] is associated with bulk lattice diffusion so that low-temperature electromigration in thin films is clearly dominated by grain boundary transport. The constant A depends on film structure and processing. k is the Boltzmann's constant. This equation plays a useful role in designing metallization; for example, no more than 10^5 A/cm² is recommended for strip widths of about 1.5 μm.

Since electromigration in thin films is dominated by grain boundary transport, the influence of microstructure is very important. Al and Al-alloy thin films generally have columnar microstructure in which most of the grain boundaries extend from the bottom

to top of the film (Figure 2.15.(a)); these produce long and continuous grain boundary paths for electromigration (Figure 2.15.(b)). However, if the width (w) of the line is less than or about equal to the average grain diameter (d), as shown in Figure 2.15.(c), some of the grains will span the line, interrupting and shortening paths for grain boundary diffusion due to electromigration. As the ratio w/d is decreased, the average length of the grain boundary diffusion paths decreases. For very small w/d , some lines will not have any paths of length greater than the critical length (l^*) so that electromigration-induced failures will then only occur by other slower mechanism such as diffusion along the Al/Si interface and diffusion through the grain lattices. This results in an increase of the median time to failure.

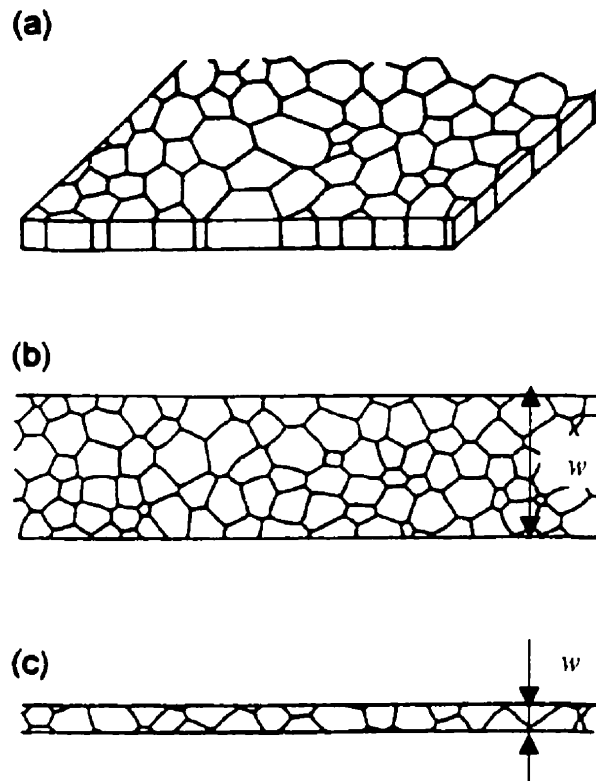


Figure 2.15. Schematic illustration of (a) a thin film grain structure, (b) a wide line with width, w , greater than average grain diameter, d , (c) a narrow line where width, w , is less than or about equal to d .

If the film is annealed after it has been patterned into lines, grain growth leads to an evolution toward a bamboo structure as shown Figure 2.16. As this evolution occurs, bamboo and non-bamboo segments develop, where the non-bamboo segments can be described as polygranular clusters. As the evolution toward fully bamboo structures continues, the average length of these polygranular clusters decreases so that it becomes less and less likely that a line will have a cluster longer than l^* . Post-patterned grain growth therefore also leads to increased lifetime of thin films due to the loss of grain boundary diffusion paths. The numbers and average lengths of polygranular clusters are expected to decrease with increased initial grain size in the unpatterned film, with decreased line width, and with increased post-patterning anneal times and temperatures.

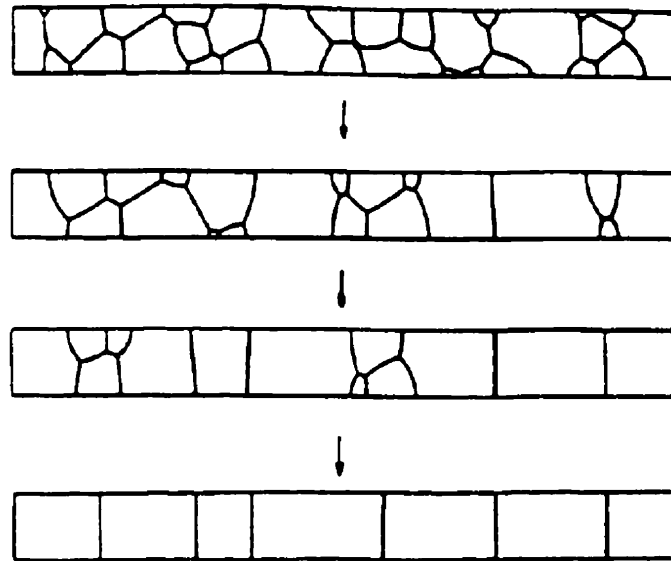


Figure 2.16. The effect of post-patterning annealing on the grain structure of interconnects.

2.4.2. Stress-Induced Voids in Thin Films

Stress-induced failures in Al interconnect were first reported around 1984 - 1985 by a number of investigators [44 - 46]. Unlike the void formed by electromigration, stress-induced voiding is due to tensile stress gradients produced by thermal expansion mismatch between the passivating dielectric layer of SiO₂ and the Al interconnects. Numerical values of thermal expansion coefficients for some materials of interest are given in Table 2.3. Note that the thermal expansion coefficients for all the metals are much larger than the coefficient of silicon and silicon oxide.

Table 2.3. Thermal expansion coefficients for some materials.

Materials	Al	Cu	Ag	Au	Si	SiO ₂
Thermal Expansion Coefficient (10 ⁻⁶ /K)	23.0	16.6	19.0	14.2	3.0	0.55

At the dielectric deposition temperature (typically 400°C), the metal will be soft and virtually stress free. After the deposition, during the cooling to room temperature, the metal will be subjected to large tensile stress because its coefficient of thermal expansion is much larger than that of the silicon and dielectric. The metal tries to relieve itself of this large tensile stress by plastic deformation. However, it cannot be deformed since the metal line is strongly adhered to the encapsulating dielectric layer. It is generally believed that the major relaxation of stress occurs by diffusional or power-law creep, which causes void formation and growth. Thus, voids are created and grown as a by-product of stress itself. Smaller voids migrate toward grain boundaries and agglomerate into larger voids to reduce the total free energy of the system, and

finally, a void can be large enough to sever the metal line. Experimental data for Al lines show that the maximum stress-induced failure generally occurs in the temperature range between 150 and 200°C [44, 47]. This can be explained by noting that the driving force due to stress decreases as temperature increases in thermal creep, but the vacancy diffusion rate increases exponentially with temperature. The product of these two driving forces gives a maximum somewhere between 150 and 200°C. Note that the temperature reaches up to 250°C by Joule heating and cools down to room temperature during the operation of power devices and circuits. It means that the stress-induced failures not only occur during metallization process but also during operation of circuits. Two types of stress-induced voids are reported [48]; a slit-like void and wedge-shaped void at the edge of the interconnection. Figure 2.17 schematically explains the formation of the two types of voids. The wedge-type void is produced by vacancy migration along the grain boundaries. The slit-like void is formed by lattice diffusion of vacancies to a grain boundary perpendicular to the interconnection length (e.g., in bamboo type grain structure).

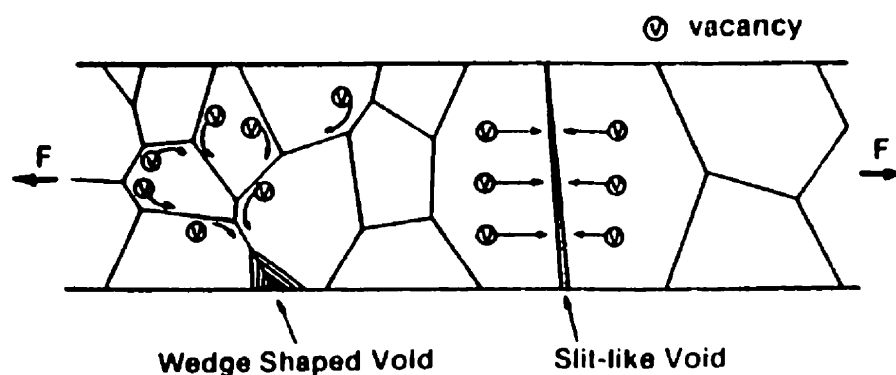


Figure 2.17. Vacancy flow mechanisms generating wedge-shaped or slit-like void [49].

Hillock Growth in metal interconnects can occur also by stress [49]. Although the metal films on Si or SiO₂ are in general under tensile stress, there are localized pockets where a compressive stress develops during deposition, especially in the near-room-temperature deposition. Any rise in wafer temperature also initiates a compressive stress in metal film. This stress induces grain boundary sliding and rotation, which excludes hillocks from the film surface, thereby causing the relaxation of the compressive stress. The process is depicted in Figure 2.18.(a), which shows a cross section of a typical columnar film structure. The arrows directed along grain boundaries describe the grain boundary shear stresses that result from the compressive stress. Figure 2.18.(b) shows the extruding grain and the lateral motion of neighboring grains that results in stress relaxation. Such grain boundary sliding is dependent on grain boundary diffusivity. Grains tend to lock along steps and triple points and unlocking requires diffusive mass transport. Thus, resistance to hillock growth is induced by the addition of diffusion-inhibiting elements such as copper, tin and indium.

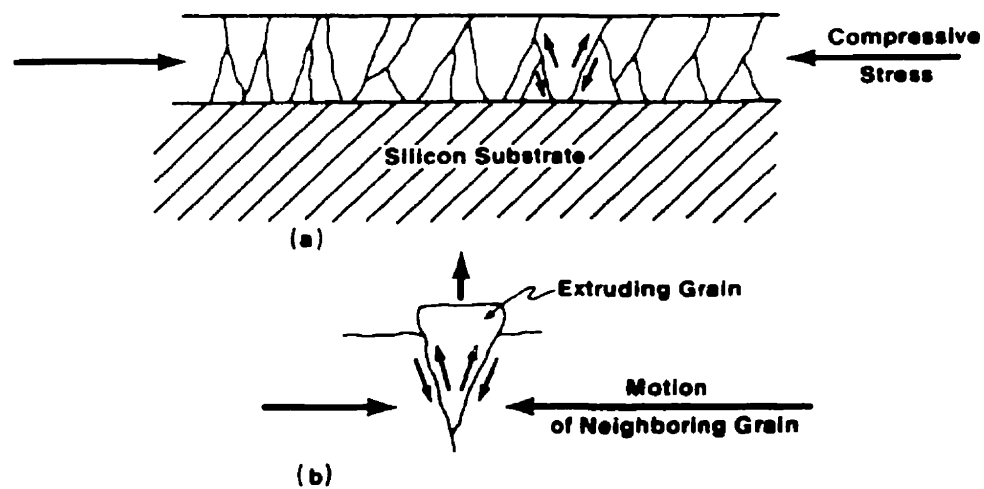


Figure 2.18. Grain boundary sliding model of hillock growth. (a) typical columnar grain structure, (b) lateral motion of neighboring grains for stress relaxation.

The main factor in the stress-induced voiding problem is the reduction in line width. As long as the line width is large relative to the thickness, bending of the dielectric above the line could relieve much of the stress and reduce the driving force for voiding. As the line width is reduced, the stress and the risk of voiding inevitably increase. Recent work [50] shows that the maximum stress occurs when the line width and line thickness are approximately equal.

Chapter 3

Experimental Techniques

The techniques and equipment used to characterize the texture and microstructure of the specimens are described in this chapter. In the beginning, the methods to obtain the film texture and residual stress are explained. For the grain boundary character distribution and the film microstructure such as grain size and grain orientation clustering, orientation imaging microscopy (OIM) was used. Details on this equipment and data available are also explained. One of equipment for surface morphology is atomic force microscope (AFM). A brief explanation on AFM follows with an explanation on scanning electron microscope (SEM). Near the end of the chapter, the thermogravimetric analyzer used for the study of copper oxidation is introduced.

3.1. X-RAY DIFFRACTOMETRY

3.1.1. Texture Measurement using X-ray Diffraction

This section provides a brief description of how x-ray diffraction is used to obtain information on material texture. The Bragg law, shown below, formally describes the conditions required for diffraction to occur in crystalline materials,

$$n\lambda = 2d_{\{hkl\}} \sin \theta_B \quad (3.1)$$

where n is the order of reflection; it may take on any integer number consistent with $\sin \theta$ not exceeding unity and is equal to the number of wavelengths in the path difference between rays scattered by adjacent planes. λ is the x-ray wavelength, $d_{\{hkl\}}$ is the interplanar spacing of the diffracting plane and θ_B is the diffracting angle. The diffracted intensity, $I_{\{hkl\}}$, depends on the volume of crystallites satisfying the Bragg law, which are illuminated by the x-ray beam.

The brief schematic of the x-ray diffractometer is shown in Figure 3.1. A specimen C is located on the table H , which can be rotated about an axis O perpendicular to the plane of the drawing. The x-ray source is S ; it is the line focal spot on the target T of the x-ray tube. S is also normal to the plane of the drawing and therefore parallel to the diffractometer axis O . X-rays diverge from this source and are diffracted by the specimen to form a convergent diffracted beam that comes to a focus at the scatter slit F and then enters the counter G . A and B are divergence and receiving slit respectively, which define and collimate the incident and diffracted beam. The receiving slit and counter are located on the carriage E , which can be rotated about the axis O and whose angular position 2θ can be read on the graduated scale K . The supports E and H are mechanically coupled so that a rotation of the counter through certain degrees is automatically accompanied by rotation of the specimen through half of those degrees. This coupling ensures that the angles of incidence on, and reflection from, the flat

specimen will always be equal to one another and equal to half the total angle of diffraction.

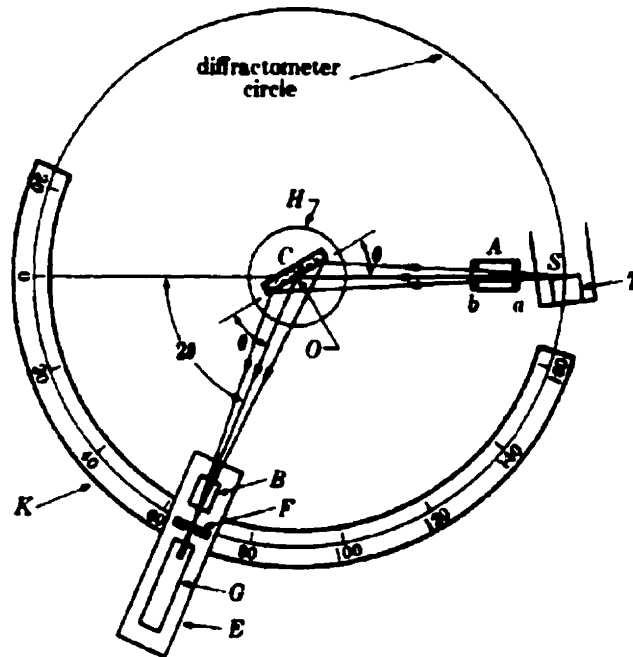


Figure 3.1. Schematic of x-ray diffractometer [51].

In textured materials, as the specimen is tilted or rotated with respect to the incident and diffracted beams, the volume of the crystallites satisfying Bragg law changes. Figure 3.2 presents schematic diagrams for a vertical-axis texture goniometer, in which the four rotation axes, $\hat{\Theta}_2$, $\hat{\Theta}_1$, $\hat{\chi}$ and $\hat{\eta}$, are defined; the scattering plane, defined by the incident (\hat{i}_i) and diffracted (\hat{i}_d) beams, is always horizontal in this type of goniometer. The $\hat{\Theta}_2$ axis is perpendicular to the scattering plane and rotates the detector to select the diffracting plane of the pole figure being measured. The $\hat{\Theta}_1$ axis is coincident with the $\hat{\Theta}_2$ axis, and rotates the Eulerian cradle – the mechanism, which produces the two specimen rotations, η and χ . The $\hat{\chi}$ axis tilts the specimen normal, ND, out of the scattering plane about an axis perpendicular the Eulerian cradle. The $\hat{\eta}$

axis rotates the specimen about its normal. The four rotations combine to move the detector and specimen such that the pole figures can be measured.

A standard pole figure measurement for the $\{hkl\}$ family of planes consists of rotating the $\hat{\Theta}_2$ and $\hat{\Theta}_1$ axis to: $\Theta_2/2 = \Theta_1 = \theta_{B\{hkl\}}$ is the Bragg angle; data is then acquired by stepping the χ and η rotations in 2.5° or 5° increments through the ranges. $0^\circ \leq \chi \leq 80^\circ$ and $0^\circ \leq \eta \leq 355^\circ$. The intensity measured at each step is proportional to the volume of crystallites within the specimen that have their poles, $\mathbf{n}_{\{hkl\}}$, parallel to the angular bisector of the incident and diffracted beams. The variation of the diffracted intensity from one complete scan can be written as $I_{\{hkl\}}(\alpha, \beta)$, where α and β are the polar and azimuthal angles describing the orientation of the scattering poles in the RD-TD-ND reference frame of the specimen.

The diffracted intensity measurements are not absolute measure of the specimen's texture because they contain the effects of systematic errors and have not been normalized. Typical systematic errors are caused by background and absorption variations and defocusing effects. In standard texture measurements, the background and defocusing effects vary with the specimen tilt angle only, and are corrected using measurements made on a randomly-oriented specimen of the same chemical composition and density; theoretical corrections are used to correct for the absorption effects. After the error corrections, the intensities are normalized using the integrated intensity of the entire pole figure. The correction and normalization produces values, $P_{\{hkl\}}(\alpha, \beta)$, in the traditional 'times-random' unit of the pole figure. The standard presentation of the pole figure is described in Chapter 2.1.

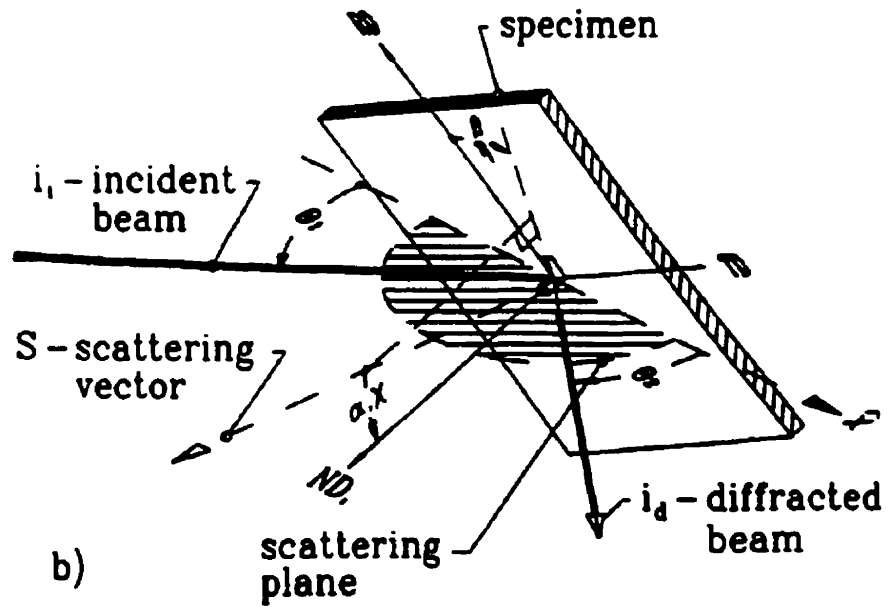
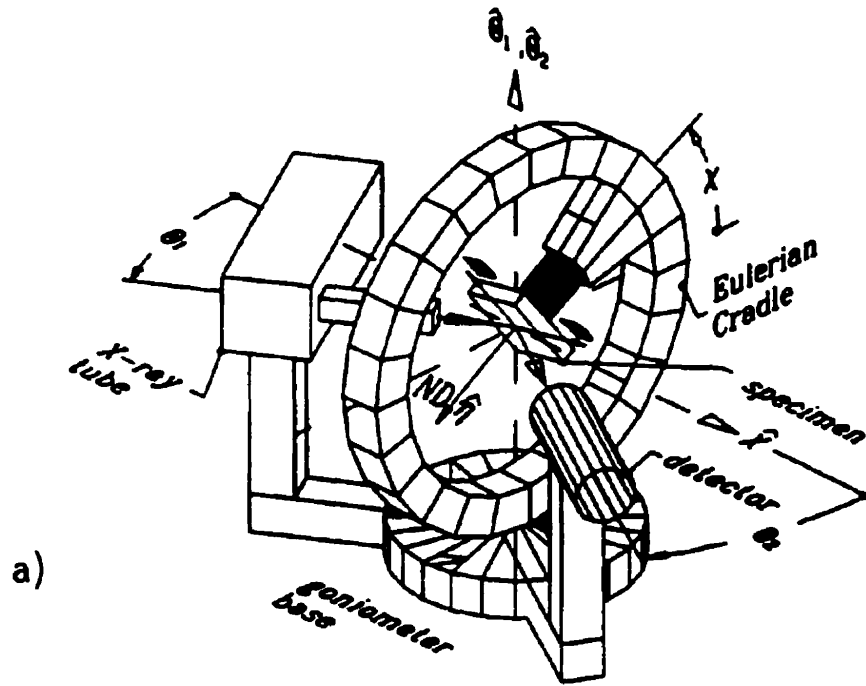


Figure 3.2. Schematic diagrams of (a) a vertical-axis texture goniometer, (b) the specimen rotation angles [52].

3.1.2. Measurement of Residual Stress by X-ray Diffraction

The residual stress of the films can be measured by the X-ray diffraction method, which is nondestructive and very practical. The method is based on the measurement of lattice plane spacing “ d ” at various tilts. When a polycrystalline material is deformed elastically in such manner that the strain is uniform over relatively large distances, the lattice plane spacings in the constituent grains change from their stress-free value to new value corresponding to the magnitude of the applied stress. From the changes in the lattice plane spacings of several orientations, which correspond with the various tilts of the specimen, the strain in the crystal lattice is measured and the residual stress producing the strain can be calculated.

For thin surface layers, a biaxial state of stress within the plane of the layer is usually assumed. In other words, the stress acting perpendicular to the surface is relaxed because x-ray diffraction occurs only in the surface layer. Then, the elastic lattice strain along a direction perpendicular to the diffraction plane, $\varepsilon_{\phi\psi}$, in a direction defined by the Euler angles ϕ and ψ with respect to the specimen reference frame (Figure 3.3) is determined as

$$\varepsilon_{\phi\psi} = \frac{d_{\phi\psi} - d_0}{d_0} \quad (3.2)$$

where ϕ is the rotation angle within the plane of the layer, and ψ is the angle between the normal to the diffracting set of the lattice plane and the normal to the specimen surface. $d_{\phi\psi}$ is the lattice spacing of planes in the direction defined by ϕ and ψ , and d_0 is the corresponding stress-free lattice spacing. Elastic theory for an isotropic solid shows that the strain, $\varepsilon_{\phi\psi}$, is

$$\varepsilon_{\phi\psi} = \frac{1}{E} [\sigma_{\phi} (1 + \nu) \sin^2 \psi - \nu(\sigma_{11} + \sigma_{22})] \quad (3.3)$$

where E is the modulus of elasticity and ν is the Poisson's ratio. The value of ν ranges from about 0.25 to about 0.45 for most metals and alloys.

Substituting this value into equation 3.2 reduces to,

$$\frac{d_{\sigma\psi} - d_0}{d_0} = \frac{1+\nu}{E} \sigma_\psi \sin^2 \psi - \frac{\nu}{E} (\sigma_{11} + \sigma_{22}) \quad (3.4)$$

For a homogeneous stress distribution, σ_ψ is constant for all ψ tilts and can be determined from the slope of the $(d_{\sigma\psi} - d_0)/d_0$ versus $\sin^2 \psi$ plot.

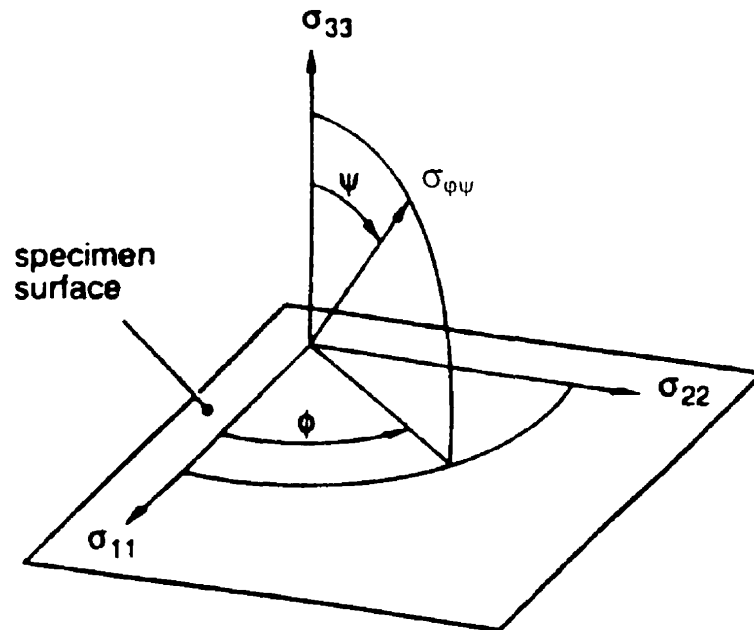


Figure 3.3. Definition of Euler angles ψ and ϕ with respect to the overall state of stress.

3.2. ORIENTATION IMAGING MICROSCOPY

Orientation Imaging Microscopy (OIM) is a technique enabling the researcher to analyze local texture and grain boundary structure of polycrystalline materials. By rapidly capturing and processing electron backscatter diffraction patterns (EBSPs) from bulk samples in the scanning electron microscope (SEM), an OIM system can produce thousands of orientation measurements in a matter of minutes, linking local lattice orientation with grain morphology.

Early exploration of the electron backscatter diffraction (EBSD) technique was in work by Alam et al. [53], where it is referred to as wide-angle backscatter Kikuchi diffraction (BKD). They used a specially constructed instrument consisting of an electron source targeted as a stationary beam onto a single crystal specimen. It was found that contrast in the diffraction patterns increased with decreasing angle of incidence of the electron beam, having the imaging plane inclined away from the vertical towards the horizontal to capture the forward scattered electrons. Application of the technique to the SEM originated with the work of Venables and co-workers [54, 55]. They describe comprehensively the experimental basis of the method. Experiments were conducted using both a standard tungsten electron source SEM and a field emission microscope. Using the latter instrument, they were able to demonstrate that the resolution limit might be as high as 20 nm laterally and 60 nm along the specimen surface in the direction of the incident beam. The difference between these two figures is due to the elongation of the electron probe along the steeply inclined specimen surface. Dingley and co-workers [56, 57] contributed to the technique by introducing online computer methods for pattern indexing. They then pioneered its use for local texture measurement, phase identification and plastic strain and plastic strain measurement. This led to the eventual adoption of the technique as a general metallographic tool. The schematic of the OIM system is provided in Figure 3.4.

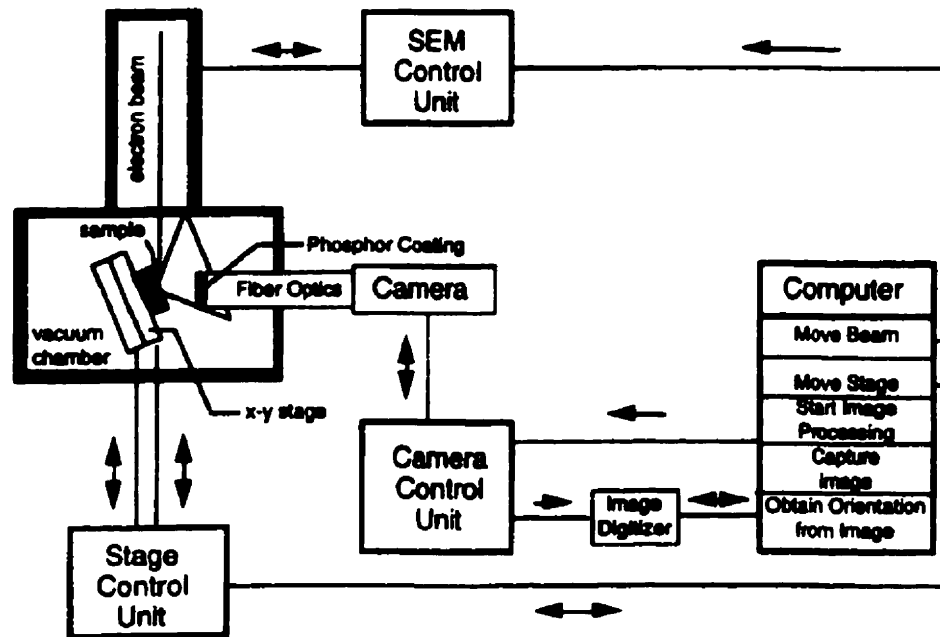


Figure 3.4. Schematic description of the Orientation Imaging Microscope.

The sample is placed in the SEM and examined first in normal secondary electron imaging or backscatter imaging (BEI) mode to seek the area from which crystallographic information is sought. The beam is collimated and positioned on the area of interest. When an electron beam of narrowly defined energy (such as that formed in a SEM) strikes a crystal with an inclined surface ($\sim 70^\circ$), the electrons disperse beneath its surface and subsequently diffract in a systematic manner. A phosphorous screen placed approximately 40 mm from the specimen, and a pattern composed of intersecting bands is formed by the diffracted electrons on the phosphorous screen. The bands in the pattern are termed Kikuchi bands and are representative of lattice planes in the diffracting crystal. The width and intensity of the bands are directly related to the spacing of atoms in the crystal planes, and the symmetry of the crystal lattice is reflected in the pattern. Thus, information regarding the structure of an unknown crystal lattice can be gained from such patterns.

High quality electron backscatter diffraction patterns (EBSPs) are obtained using a low light camera such as a silicon-intensified target (SIT) or a charge-coupled device (CCD) camera. A digital signal processor is capable of averaging a variable number of video images. The choice is usually dictated by the quality of the EBSPs, and is a function of atomic number, strain level in the sample, and the quality of the sample preparation. This averaged pattern is enhanced by flat fielding using a stored background image obtained by scanning over a large number of grains on the surface. This flat fielding removes intensity gradients in the image that were not fully removed by the camera control unit and enhances contrast.

EBSPs are used to determine the orientation of the crystal lattice with respect to some laboratory reference frame in a material of known crystal structure. To obtain the orientation from a diffraction pattern, the pattern must be indexed. Electron backscatter diffraction patterns are made up of many bands at different angles and positions. Given the angle and position of three or more bands in a diffraction pattern, the software can determine the orientation. The angles between the bands are compared against the theoretical angles stored in a look-up-table for the given material being examined to identify the (hkl) of the reflecting plane associated with the digitized bands. If the (hkl) of two bands can be determined, a corresponding orientation can be calculated. The angles in the look-up-table are calculated for a set of user-specified planes. The planes used are the strong reflecting planes, which produce the higher contrast bands in the diffraction patterns. The angles between the bands digitized by the user will usually not precisely match the theoretical ones in the look-up-table. Therefore, some deviation is allowed when matching the theoretical angles to the measured ones. This may lead to more than one solution being obtained for a set of bands. For each possible triplet of bands in the set, all possible solutions are tracked. The solutions are ranked according to how often they appear for the different triplets. The highest-ranking solution is recorded to file. An example of an indexed pattern is shown in Figure 3.5.

the sample makes an angle of approximately 70° from the vertical line of the electron beam. The flat sample surface is stationed parallel to the plane of motion of the stage such that x-y motions remain in eucentric focus.

The stored data (location, orientation, and image quality) can be processed to create Orientation Imaging Micrographs, enabling a visual representation of the microstructure. Each location is represented by a pixel, to which a color or gray scale value is assigned on the basis of the local details of lattice orientation or the quality of the corresponding EBSP. Figure 3.6 shows an example of an image that has been generated from OIM data obtained on a sample of a recrystallized nickel alloy.



Figure 3.6. OIM map of a recrystallized nickel alloy.

In addition to the visualization of microstructure, many tools are available for performing quantitative analysis of the orientation aspects of microstructure. This is the

area where OIM provides a wealth of insight that traditional microscopy techniques are simply not capable of providing. OIM can be used to investigate preferred orientation (or texture) in polycrystals similar to conventional x-ray and neutron diffraction pole figure techniques. However, since electron diffraction provides point specific orientation measurements, OIM can be used to investigate the misorientation between points in the microstructure. Thus, the preferred misorientation or grain boundary texture can be investigated using OIM. As an example of the use of OIM to investigate the distribution of orientation, sample discrete and shaded (100) pole figures measured in a sample of recrystallized aluminum are shown below in Figure 3.7.

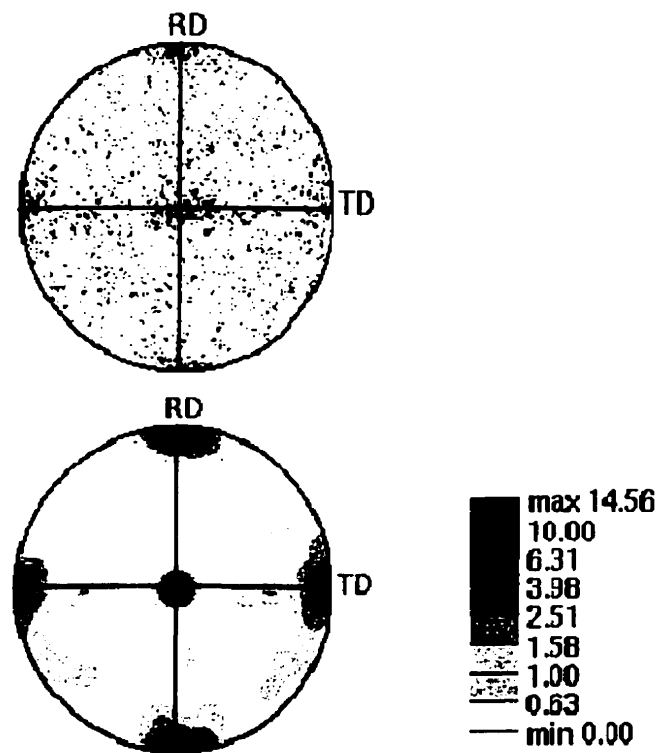


Figure 3.7. Discrete and shaded (100) pole figures for recrystallized aluminum.

3.3. ATOMIC FORCE MICROSCOPY

Very precise morphology of a sample surface can be obtained by using an atomic force microscope (AFM) that can give nanoscale morphology of sample surface.

Prior to the invention of AFM, the scanning tunneling microscope (STM) was invented in the early 1980s by G. Binnig and H. Rohrer. It scans over the sample with an atomically sharp tip and senses the tunneling current between the sample and the tip. Unfortunately, the STM is limited to conductive samples. To circumvent this limitation by G. Binnig, C. Gerber and C. Quate invented the atomic force microscope in 1985 [58]. AFM relies on the precise scanning of the tip over the sample surface like STM; however, it operates by the repulsive force between the tip and the sample surface unlike STM, which leads to the reproducing of the image of conducting samples. This invention was made possible thanks to the production of a flexible cantilever with a very low spring constant. With this cantilever that induced forces smaller than interatomic forces, the topography of the sample could be obtained without displacing the atoms. Even though the contact forces are very small, the tip may damage a soft sample. The non-contact AFM was developed by Martin et al. [59] to surmount this problem. In non-contact AFM, the tip is scanned over sample surface while the attractive forces such as Van der Waals forces between the tip and the sample surface are sensed. The cantilever is vibrated and brought near the sample surface. The force gradient due to the interaction between the tip and the sample surface then modifies the spring constant of the cantilever and changes its resonant frequency. The shift in the cantilever's resonant frequency changes the cantilever's response to the vibration source in a detectable way. If the cantilever is designed appropriately, the amplitude of the cantilever oscillation can be used to track the frequency shift. The control system maps the sample surface by adjusting the piezo height to maintain constant vibrational amplitude. Application of the non-contact AFM is limited due to some fundamental drawbacks inherent to the technique. The tip must be vibrated close to the sample surface with low energy because Van der Waals forces are relatively weak. Therefore,

moving the vibrating tip closer to the surface increases the chances of getting stuck in the contamination layer, especially the water layer, which covers the surface of samples, exposed to the atmosphere. Trapping the tip in the water layer severely degrades the image quality.

The typical contact AFM was used for this study. A schematic of the sensing system of the AFM is illustrated in Figure 3.8. A micro-fabricated silicon nitride cantilever with a sharp tip is lowered onto the sample surface with a tip force of less than 10^{-9} Newton. As the tip is brought close to the sample, it is first attracted to the sample surface. As explained before, a variety of long range attractive forces, such as Van der Waals forces, are at work when the tip gets very close to the surface, the electron orbital of the atoms on the surface of the tip and the sample start to repel each other. As the gap between the tip and sample decreases, the repulsive forces neutralize the attractive forces and become dominant. The beam from a laser diode is focused onto the back of the cantilever and reflected onto a multiple-stage photodiode. The amplified differential signal between the upper and lower photodiodes provides the sensitive measure of the cantilever deflection. A computer processes output signals and generates a three-dimensional image of the sample surface.

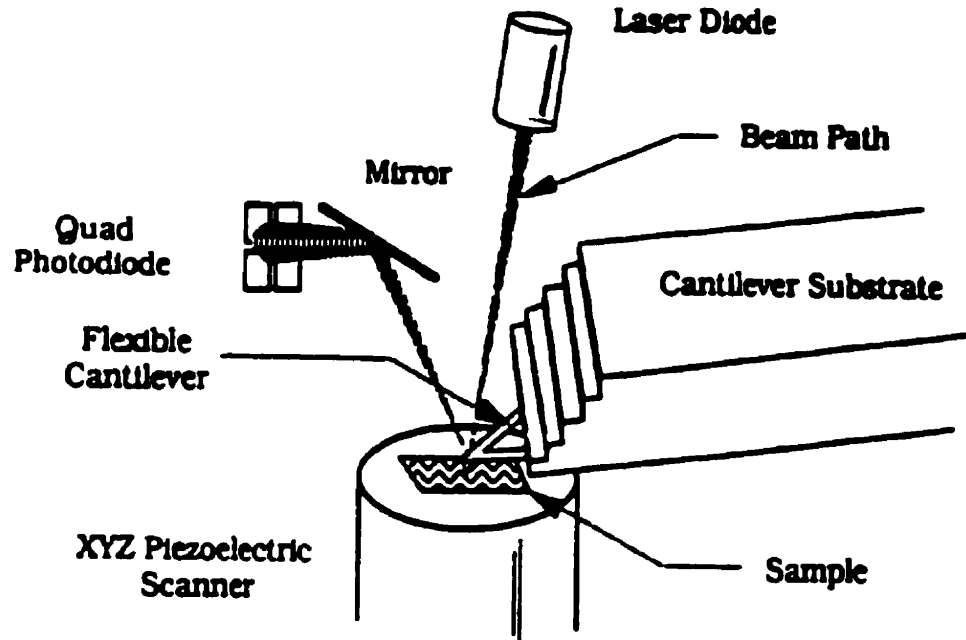


Figure 3.8. Schematic of the sensing system of AFM.

3.4. THERMOGRAVIMETRIC ANALYSIS

Thermal gravimetric analysis has been used in many fields of studies and is the one most commonly used technique for the analysis of oxidation kinetics [60 - 62]. During this analysis, the mass of the sample in a controlled atmosphere is recorded continuously as a function of temperature or time during heating. The amount and the rate of weight gain or weight loss at elevated temperatures are then analyzed and related to the structure and composition of the given sample.

The thermogravimetric analyzer (TGA) from Cahn Instruments Inc., TG-171, was used to analyze the oxidation kinetics of copper in this thesis. It provides a means for measuring weight changes of samples with a sensitivity of one microgram. The maximum operating temperature is 1700°C and the maximum weight allowed is 100g. The furnace temperature and gas atmospheres are controlled by a computer attached to the instrument. Time, weight and temperature data are acquired by the computer at defined time intervals and stored on its hard disk. A schematic representation of the TGA is illustrated in Figure 3.9. A sample is hanged on an extension wire connected to the microbalance and located inside the furnace as shown in this figure. The furnace elevator control buttons provide up and down movement of the furnace, which allows easy access for sample loading without handling the reactor tube. A thermocouple is located just under the sample and detects the current temperature. The standard type B thermocouple is used for temperatures higher than 1100°C and a type K thermocouple is used for the 25°C to 1100°C ranges. The current temperature is also shown on the temperature display. The cooling fan removes the heat generated by the furnace. The fan, along with the thermal shield under the balance, prevents thermal drift in microbalance reading. A wide range of heating and cooling ramps and isothermal segments can be selected by the computer controlling the TGA system. The temperature rates are adjustable from 0.1°C/min up to 100°C/min depending on the type of the test performed and the results that are required. However, the typical rates are in the range of 5°C/min to 20°C/min.

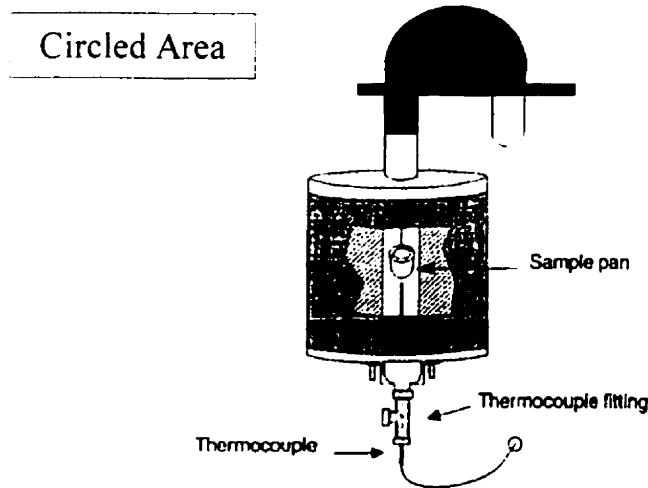
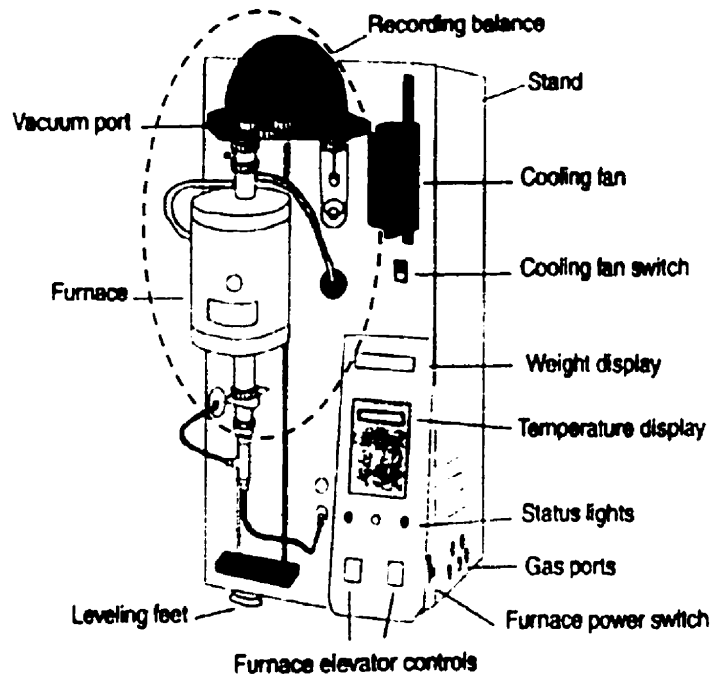


Figure 3.9. A schematic of the TGA (TG-171) from Cahn Instruments Inc.

Chapter 4

The Influence of Texture on the Reliability of Aluminum Interconnects

The influence of texture on the reliability of aluminum thin film interconnects is discussed in this chapter. This chapter is organized into eight sections. It starts with the general introduction of the work that has been done so far to understand the role of texture. The experimental procedures for this study are outlined in section 4.2. The discussion on the results obtained starts from section 4.3. The influence of texture and grain boundary character on the film reliability is discussed in section 4.3 and 4.4, respectively. In section 4.5, the discussion on the influence of microstructure is provided. Following this section, the correlation between the texture of the films and their stress-induced failures is presented. A quantitative model to obtain the optimum deposition conditions for strong $\{111\}$ texture in the film is suggested in section 4.7 and a summary of chapter 4 is given in section 4.8.

4.1. INTRODUCTION

Aluminum has been popularly used as an interconnect material because of its low electric resistivity and good adherence to SiO_2 . Other advantages of using aluminum as interconnects include the fact that this material is easily formed and etched.

As thin film multilayer interconnects are becoming smaller and more complex, various types of failures due to the increasing sophistication in multilayer interconnect structures of integrated circuit chips have been induced. One of the important reliability concerns is the electromigration-induced failure. Texture, which is developed during the deposition processes and annealing [4–6], is one of the factors influencing the electromigration-induced failure of thin film interconnects. Recent studies show that the activation energy for electromigration is dependant on texture and that a strong $\{111\}$ texture in aluminum films improves the electromigration lifetime of interconnects [7, 8].

Grain boundary character distribution (GBCD), which is related to texture, is also important since the electromigration takes place primarily along the grain boundaries. It is well known that diffusivity along grain boundaries is different, depending on whether they are low angle boundaries or high angle boundaries. During the last few years, research conducted on the properties of the special grain boundaries such as coincidence site lattice (CSL) grain boundaries has intensified, because they have been shown to be linked to special physical properties of materials [63–65]. Specifically, the electromigration failure depends on the grain misorientation distribution and, therefore, links the grain boundary structure to the mass transport primarily along the grain boundaries. However, the role the CSL boundaries play in electromigration failure remains relatively unclear. There have been few systematic studies of the effect that CSL boundaries have on electromigration failure in thin films interconnects [66].

Another important factor that causes the failure of thin film interconnects is the stress due to thermal expansion mismatch between the aluminum metallization layer and the silicon substrate [9, 10]. Not much work has been done to correlate the texture and stress-induced failures, although it is speculated that controlling the local orientation of grains could minimize stress-induced failures [11].

Although the influence of grain size on the reliability of interconnects has been well established [4, 67, 68], very little work has been done to determine the relationship between other microstructural properties such as grain clustering and surface morphology, and their reliability.

The purpose of this chapter is to improve the understanding of how texture, grain boundary character distribution, CSL boundary distribution and microstructure affect the reliability of aluminum thin film interconnects. The results on the influence of texture on the reliability of Al thin film interconnects are described and discussed. The correlation between the texture and stress-induced failures is also analyzed. It is important to control the film texture and obtain the optimum texture to improve the resistance to electromigration-induced and stress-induced failures. A quantitative model of texture development by controlling the deposition parameters is suggested in the end of the chapter.

4.2. EXPERIMENTAL PROCEDURES

4.2.1. Sample Preparation

Pure aluminum (Al) films provided by the IBM T. J. Watson Research Center were used for this study. Aluminum films were deposited on the oxidized silicon wafers by the partially ionized beam (PIB) technique and by sputtering. The sputtering system was described and illustrated in Chapter 2.3. In the PIB technique as shown in Figure 4.1, a small fraction of evaporated aluminum atoms were ionized while a potential applied to the substrate. Both neutral aluminum atoms and ionized atoms (self-ions) were deposited on the substrate simultaneously. The energetic ions provide enhanced surface mobility during deposition and effective in-situ cleaning. The substrate bias potential (ion energy) was fixed at 2 kV. Two specimens were deposited using the PIB technique with two different ion contents: PIB-2/1 with 1% ion content and PIB-2/2 with 2%. The substrate was held at room temperature; the background pressure was 10^{-4} Pa during deposition, and the deposition rate was approximately 10 Å/sec. The sputtered film, SP-2, was deposited at 2 kV. The thickness of all Al films was about 1 μm. The films obtained using the three different processing conditions were then annealed at 400°C for an hour in forming gas (90%N₂ - 10% H₂).

4.2.2. Electromigration Test

The electromigration test for pure aluminum films was done at the IBM T. J. Watson Research Center. For the electromigration analysis, thin films were patterned into test structures by reactive ion etching (RIE) in BC_l₃/Cl₂/CHCl₃ gases. During RIE etching, the wafer was placed on a radio frequency (RF) capacitive-coupled bottom electrode, which is considerably smaller than the grounded part of the system (Figure 4.2). This and the relatively low working pressure (< 500 mtorr) mean that the wafers are subjected to a heavy bombardment of energetic ions from the plasma as a result of the large, negative self-bias at the wafer surface. Anisotropic etching is obtained because

ion-enhanced chemical etching has a higher etching rate in the direction perpendicular to the wafer surface than in the direction parallel to the wafer surface. Patterned wafers were annealed at 400°C for 1 hour in a forming gas of 90% N₂ + 10% H₂. The wafers were then coated with ~ 2 μm of sputtered SiO₂. Contact holes were opened in the sputtered oxide with a standard wet etch process. The wafers were diced and the chips were mounted in 28-pin ceramic packages and ultrasonically wirebonded with Al-1wt.%Si wire. At least ten unpassivated lines, 1.8μm wide, were tested at a current density of 1x10⁶ A/cm² and at temperatures of 150, 175, 200, 225 and 253°C. Data for the 225°C tests are used in this study.

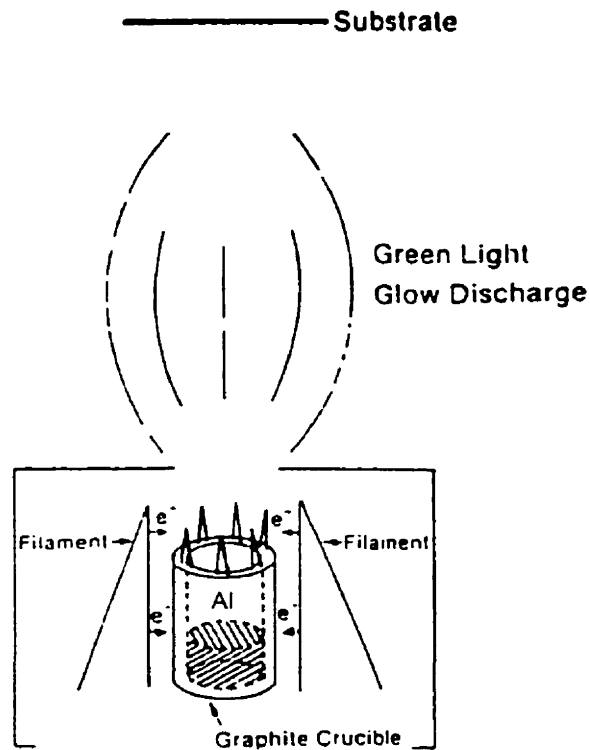


Figure 4.1. A schematic drawing of the partially ionized beam deposition.

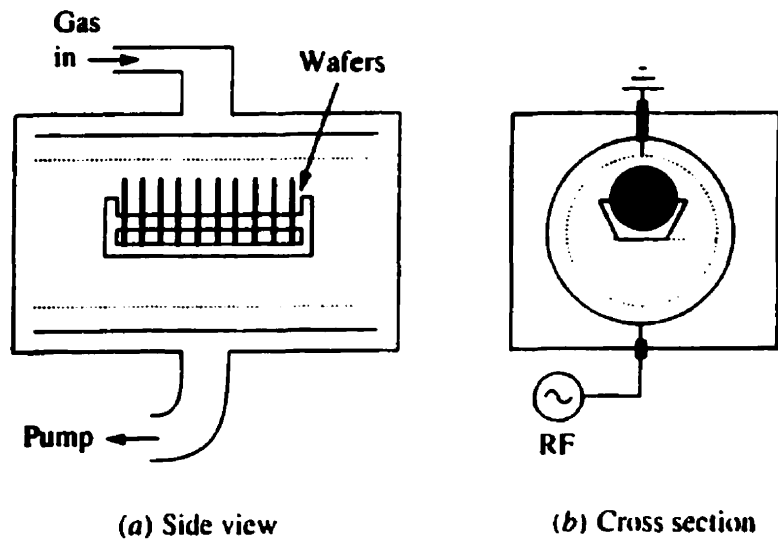


Figure 4.2. A schematic of barrel plasma RIE system.

4.2.3. Texture Measurement

The texture of the annealed Al films was measured on a Siemens texture measuring system, consisting of a PDP-11/73 controlled vertical diffractometer (D-500), attached to a Huber Eulenan cradle. The scheme of the texture goniometer system is similar as shown in Figure 3.2. The diffractometer and cradle combined provide three independent specimen rotations: the theta and 2-theta rotations provided by the diffractometer, and the χ (about an axis orthogonal to ND) and η (about ND) rotations by the cradle. Also, oscillation (translation along RD) of the specimen improves the statistics by increasing the number of grains that are being sampled. The Siemens' 2.0 kW, molybdenum target tube was run at 40 kV and 40 mAmps, while the scintillation detector operated at 900 V. The x-ray-created signals in the detector were fed through a pulse-height analyzer with time constants set at 2.0 seconds, a preamplifier gain of 32, and window settings of baseline, 2.5 V. with width, 5.0 V. The tube and detector settings were selected so as to optimize the signal-to-noise ratio for the texture measurements. The impact of defocusing on the

measurements was limited by using what is called a 'texture nose attachment' on the x-ray tube. In addition to the conventional beam-focusing slits, the texture nose is a narrow vertical slit protruding very near to the specimen; it therefore decreases the spread of the illuminated area on the specimen, and thus, the defocusing for all angles of χ .

For each specimen, texture data was collected by step-scanning every 5 degrees over the ranges $0^\circ \leq \chi \leq 80^\circ$ and $0^\circ \leq \eta \leq 355^\circ$ for the (111), (200) and (220) pole figures. Counting times for adequate counting statistics were typically 2 seconds per step.

The Siemens system automatically corrected the raw data using defocusing, absorption correction and subtracting background intensities. This data was then plotted in the form of pole figures, which were checked for signs of any remaining grinding texture or any other noticeable asymmetries. In those cases where the raw data exhibited suspicious irregularities, or if, in other words, they did not exhibit good orthorhombic symmetry, the specimens were reattached to the sample holder and remeasured. The Siemens system is not equipped with a monochromator. When measuring the texture of a thin layer (less than several micrometers of thickness) on a single crystal substrate without a monochromator, a pole figure having mixed intensities from both the thin layer and the substrate is expected [69]. The intensity from the substrate was identified and removed from the pole figure. The coefficients of ODF (up to $l_{\max} = 22$, even l only) were calculated using an incomplete pole figure method [70], which were either used to plot ODF sections or texture fibers.

4.2.4. Calculation of Grain Boundary Character Distribution (GBCD)

The distribution of coincidence site lattice (CSL) grain boundaries can be obtained from both the orientation distribution function (ODF) and the backscattered Kikuchi diffraction (BKD) patterns.

To calculate the frequency of CSL boundaries from the ODF obtained by texture measurement, special computer programs were written [71]. The program for this calculation operates in the following way: it picks two orientations with a probability determined by the ODF, calculates their misorientation, and checks if this misorientation is close to the given sigma misorientations. The accuracy of coincidence is defined by Brandon's accuracy criterion [72] of $\Delta\theta = 15^\circ \Sigma^{-1/2}$. The calculation of the frequency of occurrence of CSL boundaries is based on the assumption that the material is spatially disordered, i.e., features such as correlation between orientation of neighboring grains, inhomogeneities, clustering and grain size effects are not taken into account. The only factor that influences this calculation is the orientation distribution. The calculation is also carried out under the assumption that all of the grains are the same size. According to the above assumptions, the frequency obtained represents either the number of grain boundaries of a certain misorientation or the total area of such boundaries. A hundred thousand pairs of orientations were generated from the ODF and their misorientations were classified as a CSL or non-CSL boundaries. The frequency of occurrence up to $\Sigma 29$ CSL boundaries was calculated.

A direct method to obtain the distribution of CSL boundaries is from BKD patterns, in contrast with using ODF to the indirect method. The distribution of CSL boundaries was obtained using the TexSEM Laboratories' (TSL) orientation imaging microscopy (OIM) system attached in the Philips' XL – Field Emission Gun (FEG) Scanning Electron Microscope. The microscopy is called 'orientation imaging', owing to the fact that contrast is formed by gradients of the local lattice orientation. More specifically, backscattered Kikuchi diffraction (BKD) patterns were analyzed to determine the lattice orientation in small, localized regions. By identifying the orientation of neighboring grains from the BKD patterns, the grain boundary between these two grains can be drawn and classified as non-CSL boundary or as one of the CSL boundaries. A grain boundary was also classified as either a low angle grain boundary or a high angle grain boundary for the grain boundary character distribution. The measurements using the OIM considered grains to be different when the misorientation between two

measurements was greater than 5 degrees. The numbers of total grain boundaries considered in the specimens of PIB2/1, PIB2/2 and SP2 are 13533, 15262 and 12141, respectively. The frequency of occurrence of CSL boundaries between $\Sigma 3$ and $\Sigma 29$ CSL boundaries was obtained in addition to the grain boundary character distribution. Details on the orientation imaging microscopy are described in Chapter 3.4.

4.2.5. Microstructure Analysis

To obtain the grain size distribution of each specimen, the orientation imaging microscopy (OIM) that was used for the calculation of grain boundary character distribution was used. Grain boundaries were drawn by identifying the orientation of each grain, to which followed the determination of the grain size distribution.

For the analysis of the orientation clustering, the distribution of grain size as a function of the misorientation angle that defines a grain boundary was measured using the OIM. If the misorientation between two measurements is found to be greater than a specific angle, such as 2, 5, 10, 15 or 20 degrees, the measurements are considered to depict different grains. The average grain size as a function of the misorientation angle was calculated using these data.

To improve the understanding of the effects of grain orientation and their grain boundaries on the reliability of interconnects, the local failed areas of the patterned lines due to electromigration were also analyzed by SEM and OIM. The morphology of the failed area was recorded by a photographic recording system attached to the SEM. The orientation of grains surrounding the failed areas was obtained in addition to the identification of their grain boundaries. Working distance was 10 mm and the accelerating voltage was maintained at 20 kV.

More precise observation of the surface morphology of the aluminum films was obtained using Digital Instruments' atomic force microscopy (AFM), which gives three-dimensional images and nanoscale morphology of the film surface.

4.2.6. Measurement of Residual Stress

For the analysis of residual stress in the aluminum thin films, the Rigaku rotation anode X-ray generator (RU-200BH) with copper target was used. A nickel filter was used to reduce the background of the diffraction pattern. The tube voltage was 50 kV and the tube current was 150 mA. A step-size of the goniometer was set to 0.024 degrees and the counting time was 5-10 seconds for each angular step. The diffraction intensity (counts) and relative goniometer angle is recorded and analyzed in the computer. The general schematic of X-ray diffractometer system is shown in Figure 3.1.

The most common method to determine the residual stress level in a material is the " d - $\sin^2\psi$ " method, which is described in Chapter 3.1.2. For the d versus $\sin^2\psi$ plot, X-ray diffraction patterns from each specimen were measured for six different ψ tilts (0, 10, 20, 30, 40 and 50°).

4.2.7. Monte-Carlo Simulation to Obtain the Optimum Texture

A three-dimensional model for Monte Carlo (MC) simulation of the texture formation during film deposition is suggested. Nine different aluminum orientations with different surface energies were taken into account for this simulation. The atomistic defect simulation handler (ADESH) from the Center for Atomistic Simulations and Analysis (CASA) was used to calculate the surface energies of the grains of aluminum. ADESH is an interactive program where one can prepare and process atomistic configuration of materials. Details of this simulation are discussed in Chapter 4.7.

4.3. CORRELATION BETWEEN THE TEXTURE OF FILMS AND THEIR RELIABILITY

The texture of the PIB2/1, PIB2/2 and SP2 specimens are shown in Figure 4.3. All of the three specimens have a $\{111\}$ fiber texture as seen in the gamma fiber plot where $\Phi \cong 55^\circ$, $\varphi_2 = 45^\circ$ and φ_1 goes from 0° to 90° . To clarify the shape of the $\{111\}$ fiber, the $\varphi_1 = 45^\circ$ sections in the ODF of the specimens are presented in Figure 4.4. The specimen PIB2/1 has the sharpest $\{111\}$ fiber texture and the maximum intensity of 73 times random is located in the center of the fiber. PIB-2/2 also has the maximum value of $f(g) = 25$ in the center of the $\{111\}$ fiber; however, the maximum value is much weaker than that of specimen PIB-2/1. The specimen SP2 has a fiber texture, which is weak and inclined away from $\{111\}$ fiber by about 8~10 degrees with a maximum intensity of 6. Actually, the specimen SP2 has a fiber texture close to $\{332\}$, which is near the $\{111\}$ fiber texture.

In the early stages of film formation, the island growth (Volmer-Weber growth) predominates in polycrystalline films deposited on the amorphous or polycrystalline substrates. Figure 4.5 shows the three important energies during the film formation where γ_s is the surface energy of the substrate, γ_f is the surface energy of the film, γ_{sf} is the interface energy between the substrate and the film, and θ is the contact angle. For island growth, $\theta > 0$, and therefore $\gamma_s < \gamma_{sf} + \gamma_f$. The γ_{sf} is important in the initial stage of film formation since lattice matching between the substrate and the film deposit can reduce the interfacial energy; however, the γ_f becomes dominant as film starts to grow. The γ_f is anisotropic and minimization of γ_f works as a driving force of the texture formation during film growth. Aluminum film generally has a $\{111\}$ fiber texture in the absence of a strong substrate effect or a condition of high vapor supersaturation (low substrate temperature and/or high deposition rate), since the surface energy (γ) in face centered cubic crystals ranks as $\gamma_{\{111\}} < \gamma_{\{100\}} < \gamma_{\{110\}}$. According to Walton's model [73], high vapor supersaturation potentially leads to randomly oriented nuclei of the film.

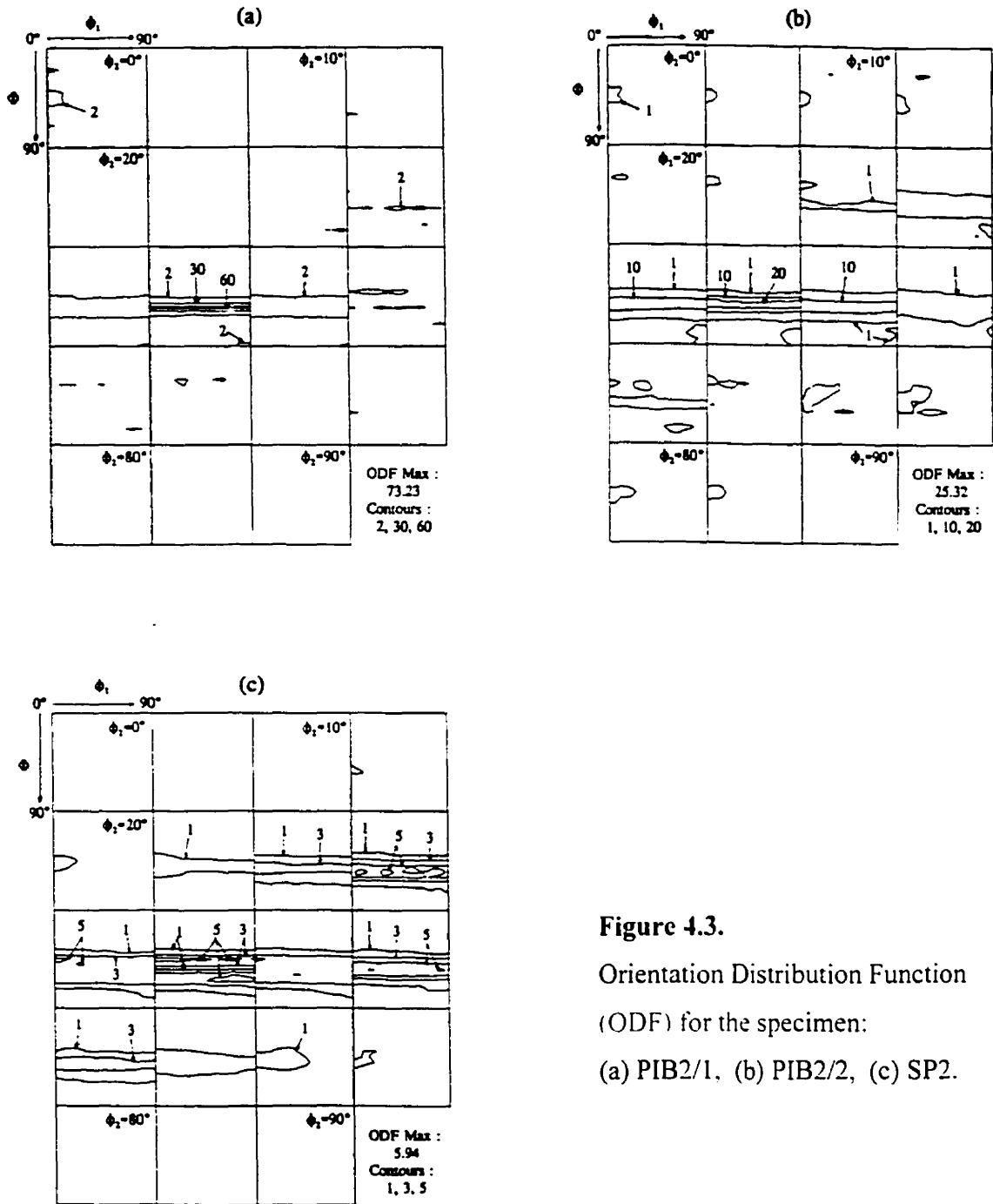


Figure 4.3.
Orientation Distribution Function (ODF) for the specimen:
(a) PIB2/1, (b) PIB2/2, (c) SP2.

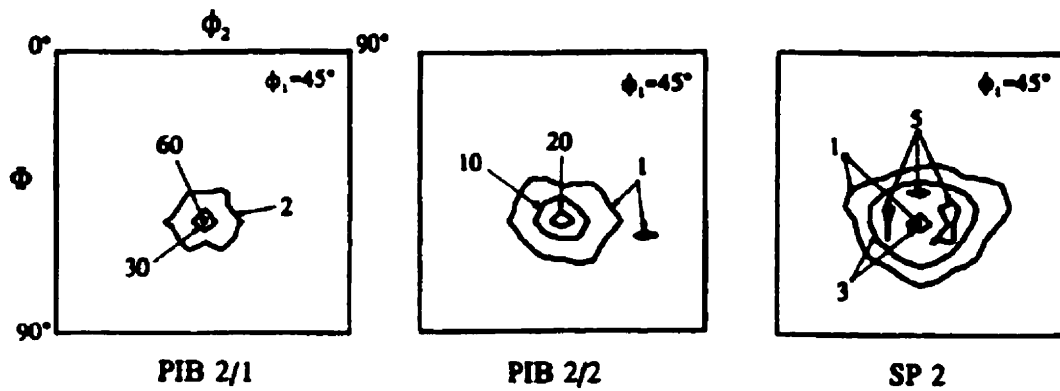
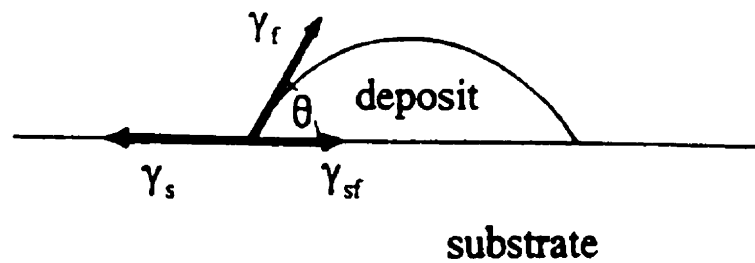


Figure 4.4. $\phi_1 = 45^\circ$ sections of the ODF obtained from the three specimens.



$$\gamma_s = \gamma_{sf} + \gamma_f \cos \theta$$

Figure 4.5. A schematic of the basic energy equilibrium on a substrate surface during film formation.

The results of the electromigration tests are shown as the cumulative failure distribution in Figure 4.6. The median time-to-failure (MTF or t_{50} value) is the time required for 50% of the test population to fail and usually represents the reliability of film interconnects. As shown in this figure, the median time-to-failure for the specimen PIB2/1, PIB2/2 and SP2 are 772 hours, 235 hours and 29 hours, respectively.

The median time-to-failure (t_{50} value) is illustrated as a function of the maximum intensity of the fiber texture in Figure 4.7. It is clear that the lifetime of aluminum interconnects increases as the strength of fiber texture increases. It should be also noticed that the tilt of the predominant texture component away from the {111} fiber texture observed in SP2 has a significant effect on the median time-to-failure.

This result corresponds well with the previous works. The importance of texture on reliability was first recognized in the early studies of electromigration by Attardo and Rosenberg [4]. They reported a substantially improved median time to failure (MTF) for strongly {111} textured interconnect lines compared to weakly textured lines. However, an unambiguous correlation was not possible because the grain size was very different between the two conditions and the thickness and width of tested strips are thicker than those of lines actually used in the industry. A more detailed analysis by Vaidya and Sinha [74] provided a quantitative measure of several microstructural attributes, including texture. They found that the MTF increases with the increasing grain size, S , the degree of {111} texture, and the decreasing spread in the grain size distribution, σ , as shown in equation 4.1.

$$MTF = \frac{S}{\sigma^2} \log(I_{\{111\}}/I_{\{200\}})^3 \quad (4.1)$$

where S is the median grain size, σ is the standard deviation of the log-normal grain size distribution. $I_{\{111\}}$ and $I_{\{200\}}$ are the intensities of the corresponding X-ray diffraction peak. However, this correlation was developed only for polycrystalline lines where their width is larger than their grain size. Li et al [7] also showed a substantial increase

in electromigration lifetime as $\{111\}$ texture become stronger, but this study lacked the statistical significance since only one line was examined in each condition for the electromigration test. The $I_{\{111\}} / I_{\{200\}}$ value or the $I_{\{111\}}$ value obtained from x-ray diffraction was mostly used in earlier studies. However, these values do not represent the intensity of $\{111\}$ texture accurately because the width or background intensity can be changed, depending on specimens. A pole figure or ODF, representing the volume fraction of grains having different orientations, must be used for better accuracy. More recent studies by Knorr and Rodbell [8] isolated the texture effect in pure aluminum and AlCu alloy thin films. They pointed out that a substantial improvement in reliability is possible by obtaining strong $\{111\}$ fiber texture.

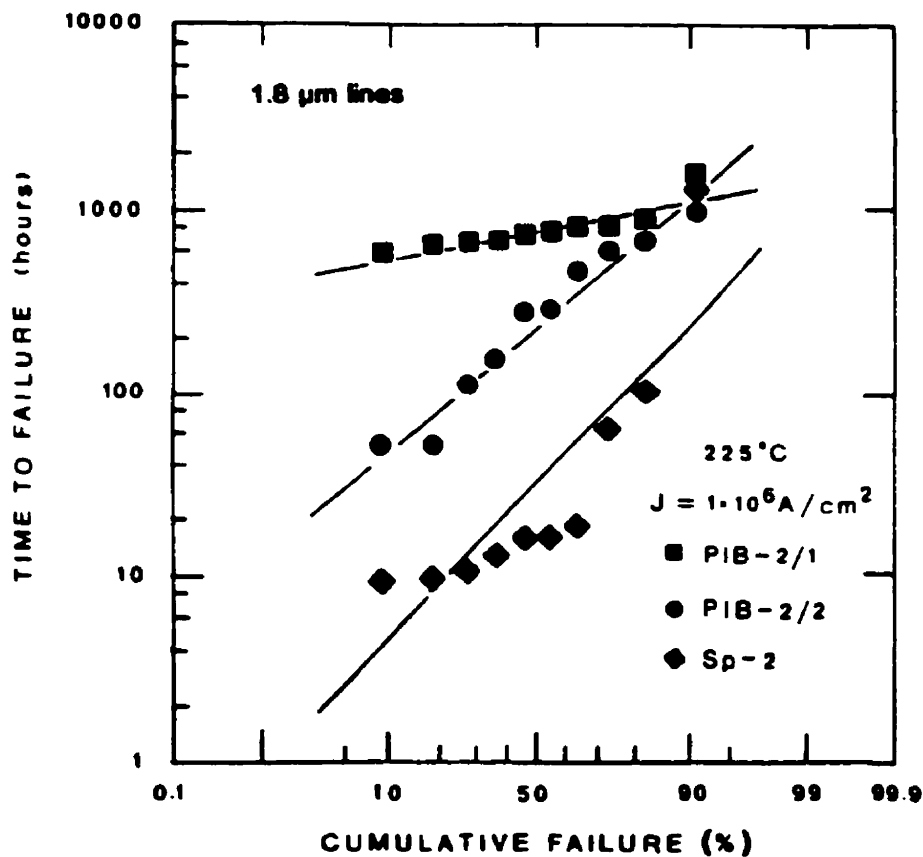


Figure 4.6. The results of electromigration tests from the specimens.

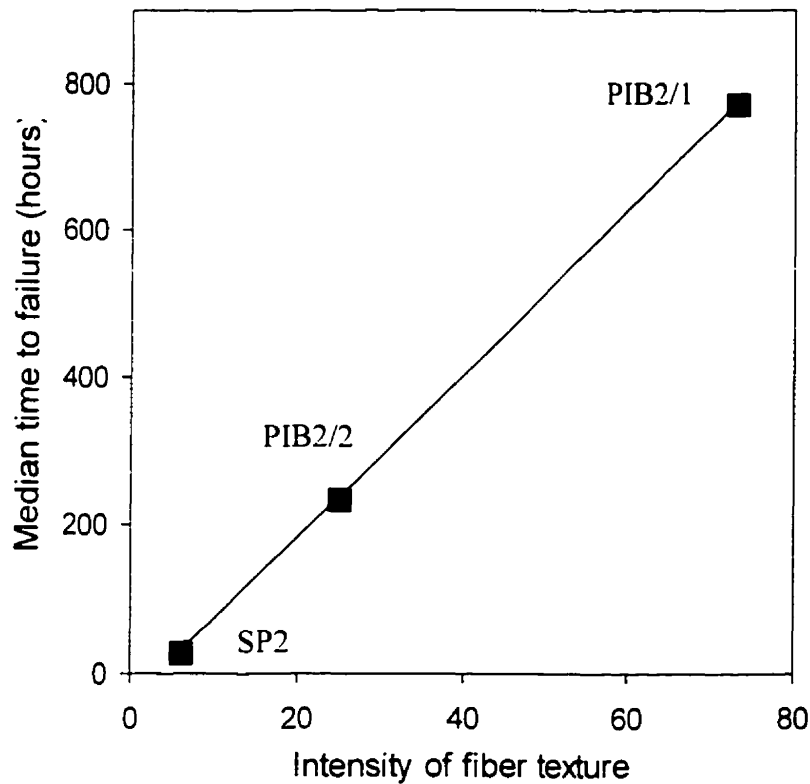


Figure 4.7. Median time to failure as a function of the intensity of fiber texture.

Much work has been done to correlate the film texture and its reliability. Researchers agree on the fact that strong $\{111\}$ texture in Al film interconnects improves their reliability. However, the nature of this fact has not been well understood and explained. Considering the fact that electromigration mostly take place along grain boundaries and texture is closely related with the grain boundary characteristics, investigation on the grain boundary characteristics is necessary. This work is described and discussed in the following chapter.

4.4. CORRELATION BETWEEN THE GRAIN BOUNDARY CHARACTER AND THE RELIABILITY OF INTERCONNECTS

Electromigration is a phenomenon of the migration of metal atoms mostly along the grain boundaries. Therefore, it is necessary to work on grain boundary characteristics and their influence on electromigration.

It is convenient to classify the grain boundaries based on misorientation angles. Generally, grain boundaries are grouped into two classes, namely *low angle grain boundaries* (LAGB) and *high angle grain boundaries* (HAGB). The angle at which transition from high angle to low angle boundaries occurs is typically between 10° and 20°. The boundaries with misorientation higher than the transition angle are called *high angle grain boundaries*. *Low angle grain boundaries* are those, which are composed of arrays of dislocations [75, 76], and structure and properties of these boundaries vary as a function of misorientation [77].

Figure 4.8.(a), (b) and (c) show the distribution of misorientation angle between grains in the specimen PIB2/1, PIB2/2 and SP2. These data were obtained using orientation imaging microscopy (OIM) with 5 degrees of grain boundary definition. If the misorientation between two measurements was greater than 5 degrees, the measurements were considered to be from different grains. As can be seen from the same figure, the specimen PIB2/1 has a relatively larger number of LAGBs than the other specimens. Worthy of note especially is that the number of grain boundaries with 5 - 6° of misorientation is the highest in this specimen. The theoretical misorientation distribution obtained from the randomly oriented (not textured) specimen [71] is illustrated in Figure 4.8.(d). One noticeable detail is that all of the Al films, even the specimen SP2 that has relatively weak texture, have higher number of LAGBs than the randomly oriented specimen. In cubic materials, the relative rotations of the two grains can be described in 24 different ways because of the symmetry. It is conventional to describe the rotation by the smallest misorientation angle (θ) and the corresponding

axis. Mackenzie [78] has shown that the maximum value of θ is 62.8° for axis $<1.1.\sqrt{2}-1>$.

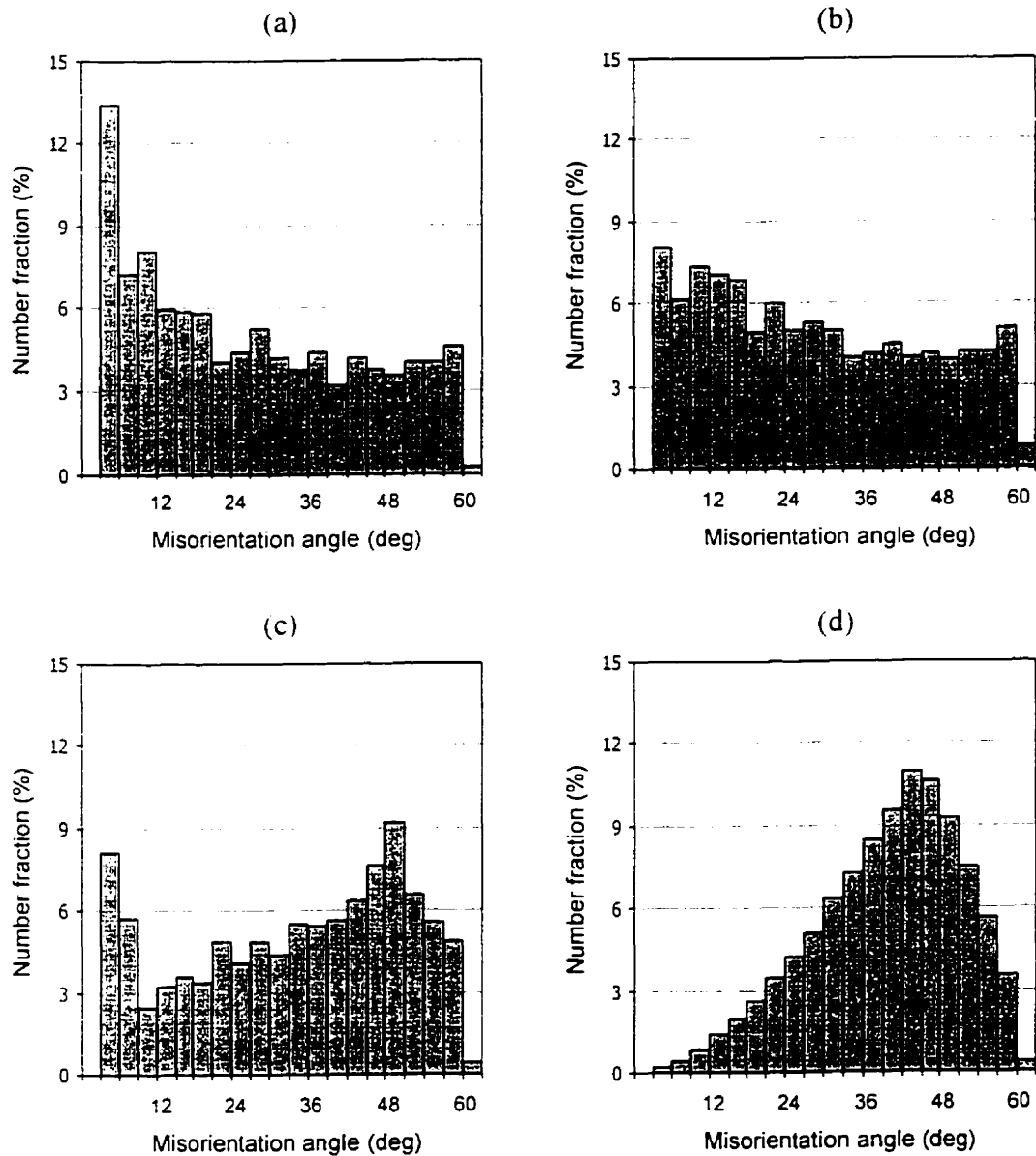


Figure 4.8. Distribution of misorientation angle of grains in (a) PIB2/1, (b) PIB2/2, (c) SP2, (d) randomly oriented specimen.

The number of low angle grain boundaries (less than 15°) of each specimen is summed and plotted in Figure 4.9. The total fractions of LAGBs in the specimen PIB2/1, PIB2/2 and SP2 are 0.35, 0.29 and 0.2, respectively. It is generally known that diffusion along low angle grain boundaries is slower than that along high angle grain boundaries because most of the low angle grain boundaries usually consist of arrays of well-separated lattice dislocations. The diffusion spectrum for fcc metals obtained by Gjostein [79] shows that the HAGB diffusivity is much higher than LAGB diffusivity. The correlation between the median time to failure (MFT) and the number of low angle grain boundaries is illustrated in Figure 4.10. It seems that the relatively high amount of LAGB, especially the large number of grain boundaries of very low misorientation ($5 - 6^\circ$) in PIB2/1, may play a part in extending the lifetime of a specimen. Hoffman [80] pointed out that the diffusion parallel to the tilt axis is much faster than the diffusion perpendicular to the tilt boundary, especially for the LAGB. In the specimen PIB2/1, most of the grains have $\{111\}$ planes parallel to the substrate since it has strong $\{111\}$ fiber texture. Viewed in the direction normal to the film plane, most of grains differ from each other only by a rotation, which would produce $\{111\}$ tilt grain boundaries perpendicular to the film plane. LAGBs are composed of a vertical array of parallel edge dislocations and thus the direction of the fastest diffusion (along the dislocation cores) is orthogonal to the film plane. Therefore, the grain boundary diffusion is expected to be slower as $\{111\}$ texture increases. This factor is also expected to contribute to the longer lifetime of the specimen PIB2/1. However, the contribution of LAGBs on the reliability of the films is not believed to be very large since there is only about 6% difference in the number of LAGBs between PIB2/1 and PIB2/2.

A grain boundary is the region where two periodic structures, i.e., the two adjoining crystal lattices, meet. When two identical crystal lattices are rotated around a common crystallographic axis and a number of lattice sites coincide with sites of the other lattice, a boundary with a certain relative orientation (coincidence orientation) is formed. This boundary is called coincidence site lattice (CSL) boundary [81].

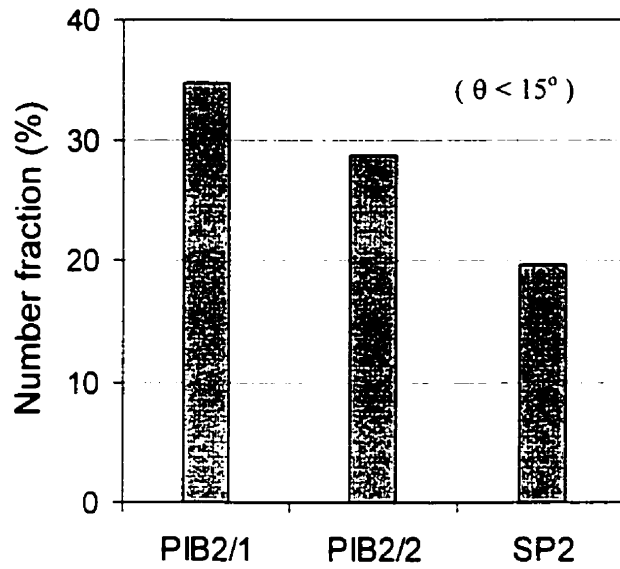


Figure 4.9. The number fraction of low angle grain boundaries ($\theta < 15^\circ$).

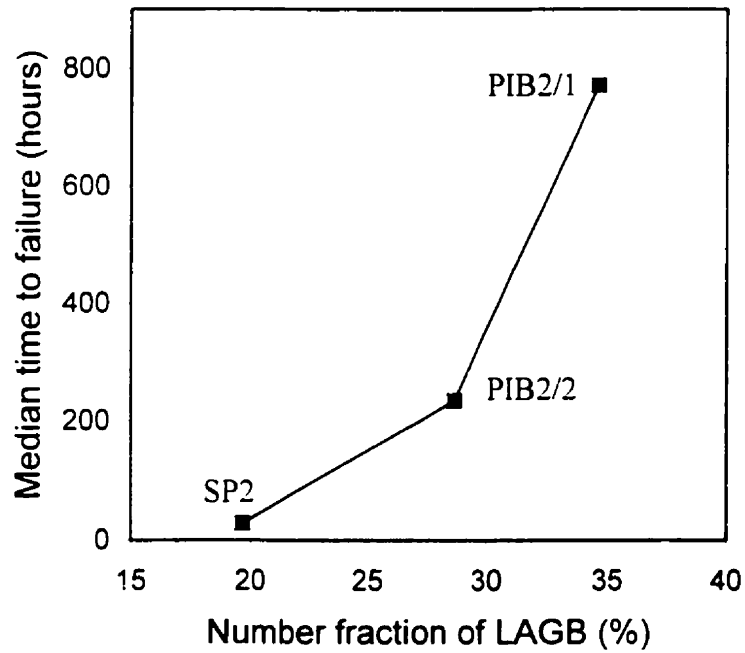


Figure 4.10. Median time to failure as a function of number of Low angle grain boundaries.

The reciprocal density of coincidence sites relative to crystal lattice sites is denoted by Σ , which is characterized by the rotation axis (hkl) and the rotation angle (θ) [81]. For example, the grains adjacent at a $\Sigma 5$ boundary have one-fifth of their representative crystal lattice points in coincidence. For the cubic systems, these CSL boundaries have odd integers as Σ values. These CSL boundaries, especially the low Σ boundaries, are known to behave like low angle grain boundaries and have exceptional physical and chemical properties such as low energy, high resistance to corrosion and fracture or high migration rate in the presence of impurities [63 - 65]. Low Σ boundaries are also called 'special' boundaries because of these special properties. CSL boundaries lose their special properties as Σ values increase. High Σ grain boundaries, usually $\Sigma > 51$, are not considered as 'special' anymore. The CSL boundaries up to $\Sigma 29$ have been considered for this study.

Figure 4.11 shows the distribution of CSL boundaries from $\Sigma 3$ to $\Sigma 29$ for the three specimens. These data were also obtained using orientation imaging microscopy (OIM) with 5 degrees of grain boundary definition. In all specimens, the frequency of the $\Sigma 3$ and $\Sigma 7$ boundaries are relatively higher than other CSL boundaries. In addition, the thin films deposited by the partially ionized beam technique (PIB2/1, PIB2/2) have a higher number of $\Sigma 3$, $\Sigma 7$, $\Sigma 13b$, $\Sigma 19b$ and $\Sigma 21a$ boundaries than the sputtered film (SP2). More specifically, PIB2/1 has a much higher number of these specific CSL boundaries than the other specimens. It is noticeable that these boundaries have a common $\langle 111 \rangle$ rotation axis. Specimen SP2 shows the random distribution of CSL boundaries except for slightly higher frequency of $\Sigma 3$ and $\Sigma 7$ boundaries. The $\Sigma 3$ boundary is the well-known completely coherent $\{111\}$ planar twin boundary, which has been shown in general to possess very low diffusivity. As Faridi and Crocker [83] proved, vacancy migration energies in the core of this boundary are at most only slightly lower than in the lattice. According to Sutton et al [84], the structure units making up the $\Sigma 27$ boundary are much more loosely packed than the units making up the $\Sigma 11$ boundary, which appear to be relatively closely packed. Therefore, the diffusion rates along the $\Sigma 3$ and $\Sigma 11$ boundaries are expected to be slow, and the diffusion rate along the $\Sigma 27$

boundary is expected to be relatively faster. The measurements of relative diffusion rates along some CSL boundaries in aluminum by Herbeuval et al [85] also agree with result obtained by Sutton et al [84]. Peterson [86] also found remarkably low diffusivity along $\Sigma 3$ and $\Sigma 11$ boundaries in various fcc metals. The number of $\Sigma 3$ boundaries in the specimen PIB2/1 is quite noticeable. About 11% of all the grain boundaries in the PIB2/1 are $\Sigma 3$ boundaries. This is a very high number considering the fact that there is about 1.8 % of $\Sigma 3$ boundaries in a randomly oriented specimen [71]. It seems that the high frequency of $\Sigma 3$ boundaries, which have relatively low diffusivity, contributes to specimen PIB2/1's long lifetime. The specimen PIB2/1 and PIB2/2 have negligible number of $\Sigma 11$ and $\Sigma 27$ boundaries. The SP2 has about the same number (0.7%) of $\Sigma 11$ and $\Sigma 27$ boundaries, and thus the influence of these boundaries on diffusivity compensate for each other.

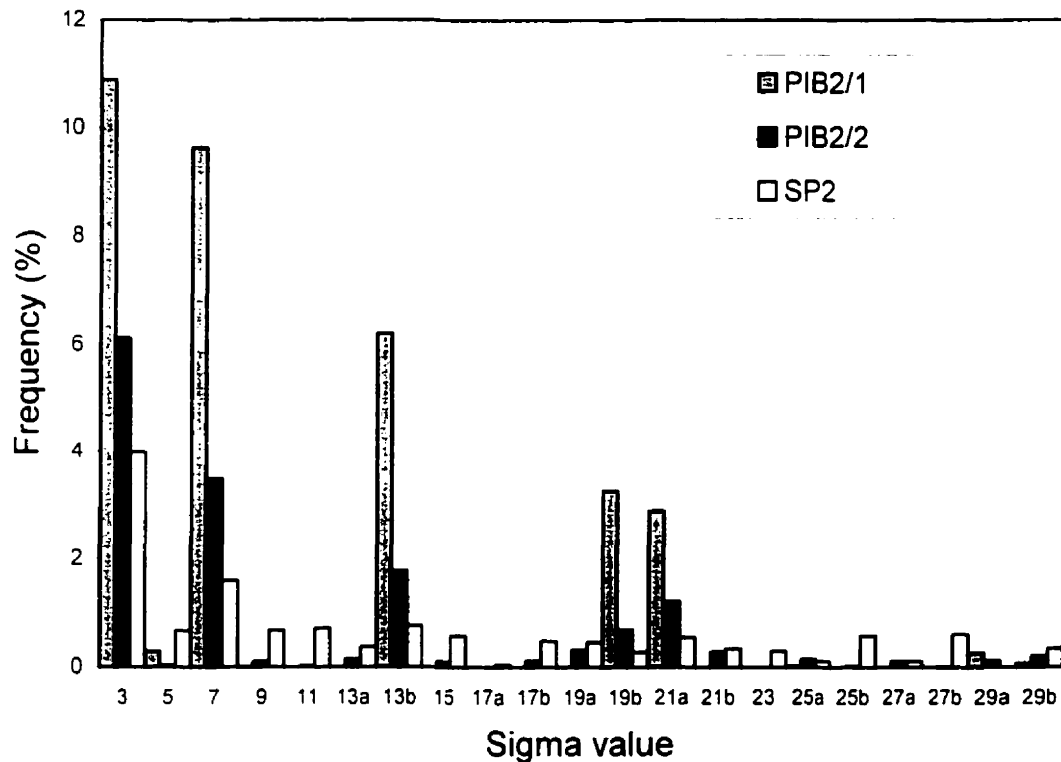


Figure 4.11. Distribution of CSL boundaries obtained from OIM ($\Sigma 3$ - $\Sigma 29$).

Figure 4.12 shows the distribution of CSL boundaries from $\Sigma 3$ to $\Sigma 29$ calculated from the orientation distribution function (ODF) of the three specimens. It shows similar trend in the distribution of CSL boundaries obtained from OIM. For example, the specimens PIB2/1 and PIB2/2 have a higher frequency of $\Sigma 3$, $\Sigma 7$, $\Sigma 13b$, $\Sigma 19b$ and $\Sigma 21a$ boundaries than the SP2 specimen. However, the frequency of CSL boundaries calculated from ODF is lower than that obtained from OIM. Especially in the specimen PIB2/1, the difference of frequency of $\Sigma 3$ boundaries is large: more than 7%. The calculation of CSL distribution from ODF is based on the method developed by Moraviec et al [71]. They assumed that the material is composed of oriented but pointwise grains (hence each of same size), chaotically scattered throughout the sample to avoid correlation between neighboring orientations and providing statistical homogeneity. In other words, they ignored the inhomogeneity, grain clustering and grain size effects. However, those inhomogeneities usually exist in real materials.

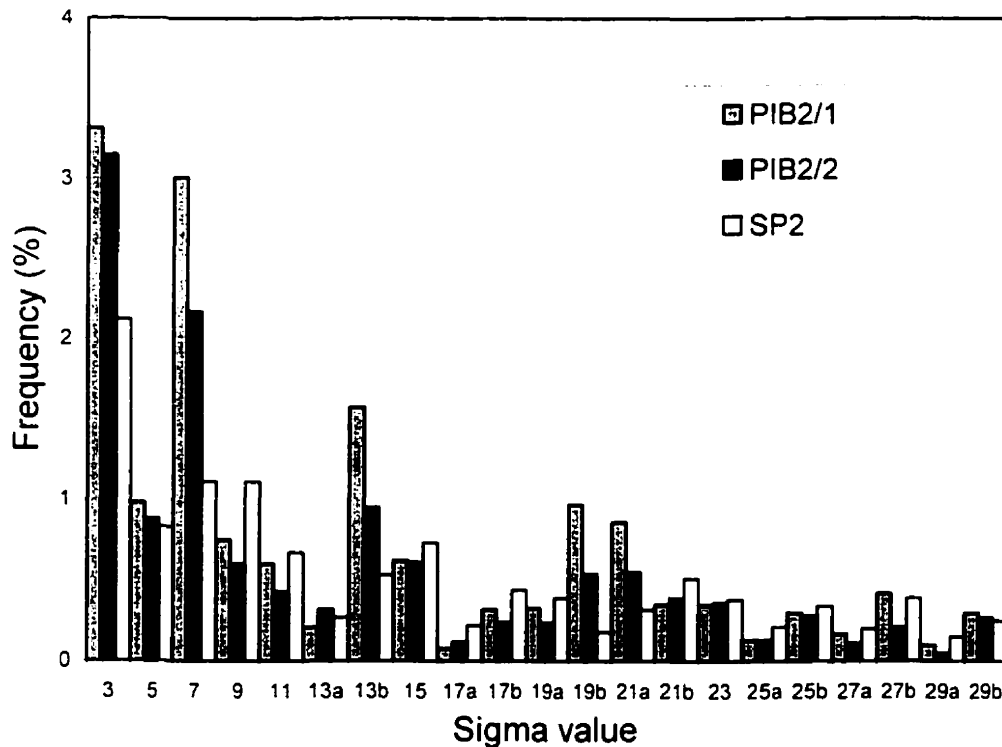


Figure 4.12. Distribution of CSL boundaries obtained from ODF ($\Sigma 3 - \Sigma 29$).

For example, the investigated specimens (PIB2/1, PIB2/2 and SP2) are found to have clusters of grains having similar orientation, which will be discussed in Chapter 4.5. It seems that the CSL boundary distribution obtained by OIM is more reliable than that from ODF.

In Figure 4.13, the results of the electromigration test are compared to the total frequency of CSL boundaries. The data obtained from OIM is used. The specimen PIB2/1 has the highest percentage of CSL boundaries, 33.3 %, as well as the longest median time-to-failure (t_{50} value), 772 hours. Specimen PIB2/2 had 15 % of CSL boundaries and t_{50} value of 235 hours. Specimen SP2 had the shortest lifetime, $t_{50} = 29$ hours, and the lowest percentage of CSL boundaries, 12.3 %. It is clear from this comparison that there is an association between the time-to-failure and the frequency of occurrence of CSL boundaries; a higher percentage of CSL boundaries correlates with a longer lifetime in patterned lines. Several studies [71, 72, 87, 88] have calculated the frequency of CSL boundaries in materials with a random grain orientation. A total of 9.6 % of the boundaries are found to be $\Sigma 3$ to $\Sigma 29$. This indicates that the grain boundary texture in SP2 deviates slightly from the distribution expected in a random material. An atom in the boundary occupying a site of the CSL would be in the region of good atomic fit because the site is common to both neighboring crystal lattices. Thus, the lower the Σ value, a higher planar coincidence site density, and thus lower diffusivity along the boundary core is obtained. Therefore, the presence of a high number of CSL boundaries in the specimen (specimen PIB2/1 in this study) seems to improve the electromigration lifetime of films as shown in Fig. 4.13.

Figure 4.14 shows the relationship between the $\{111\}$ texture and amount of LAGBs and CSL boundaries in the specimen PIB2/1, PIB2/2 and SP2. Clearly, the number of these boundaries increases with the intensity of the $\{111\}$ fiber texture. The microtexture of individual grains is responsible for the grain boundary misorientation geometry. Therefore, it is generally believed that the grain boundary character distribution and the CSL boundary distribution are linked to the material texture.

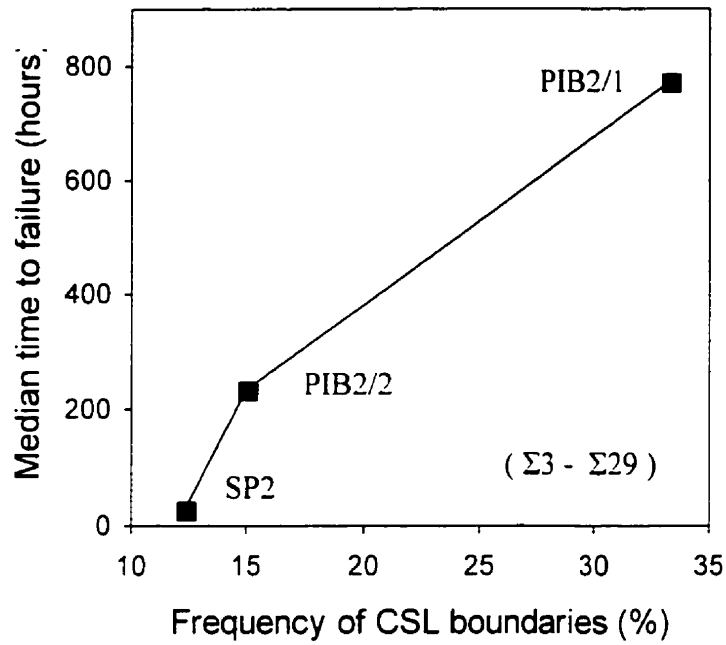


Figure 4.13. Median time to failure as a function of total frequency of CSL boundaries from $\Sigma 3$ to $\Sigma 29$.

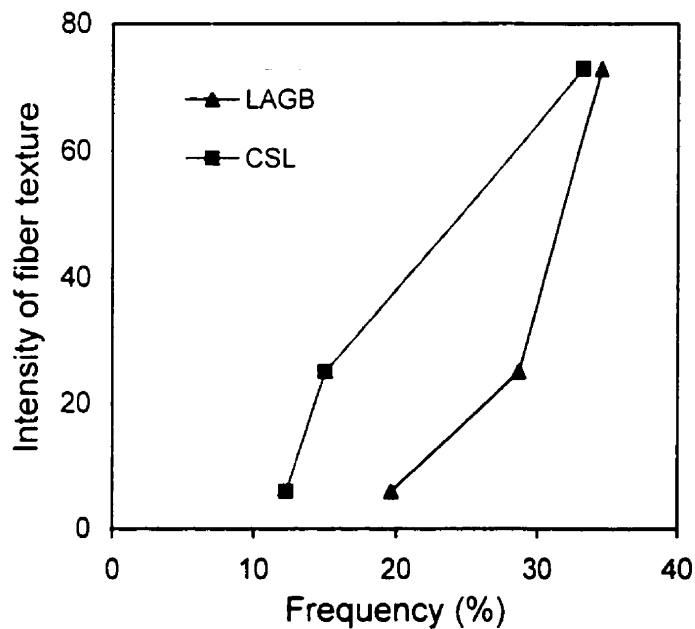


Figure 4.14. Frequency of low angle grain boundaries ($\theta < 15^\circ$) and CSL boundaries ($\Sigma 3 - \Sigma 29$) as a function of intensity of $\{111\}$ fiber texture.

The modeling of $\{111\}$ fiber texture by Garbacz et al [89] shows that the proportion of CSL boundaries continues to increase as the $\{111\}$ texture increases beyond the level found in PIB2/1.

The intensity of $\{111\}$ texture represents the volume fraction of $\{111\}$ grains in the specimen. Thus, many grains having the $\{111\}$ orientation exist in the specimen with strong $\{111\}$ texture. Assuming that there is a small deviation in grain size, the $\{111\}$ grains have more chance to neighbor each other and hence, many grains having low misorientation are expected. It can therefore be concluded that the number of LAGBs increases as texture becomes stronger. The relationship between CSL boundary distribution and material texture has not been clearly understood. Experimental results show that the percentage of CSL boundaries is often higher in textured materials than that in random oriented materials [89, 90]. In the case of Al films, the $\Sigma 3$ boundary is the coherent $\{111\}$ planar twin boundary having a common $\langle 111 \rangle$ rotation axis. The $\{111\}$ planes are parallel to the substrate in most of the grains in the specimen PIB2/1, since it exhibited a strong $\{111\}$ fiber texture. Viewed in the direction normal to the film plane, most grains differ from each other only by a rotation, which would produce $\{111\}$ tilt grain boundaries perpendicular to the film plane. This explains the high number of $\Sigma 3$ boundaries and other boundaries ($\Sigma 7$, $\Sigma 13b$, $\Sigma 19b$ and $\Sigma 21a$) having a common $\langle 111 \rangle$ rotation axis in the specimen PIB2/1.

A detailed analysis on the grain boundary characteristics around the failure sites has been done by using OIM. About 20 failure sites were investigated. In all the cases, high angle and non-CSL boundaries, which are represented as black lines in Figure 4.15, are connected to the failed area. It seems that most of the mass flux, which causes the voids, took place along these high angle, general boundaries. This result strongly supports that the reliability of films relates to the grain boundary character distribution, which is controlled by the film texture as explained before. However, only about 20 failed sites were found and analyzed in the examined specimens as mentioned before.

An investigation of more failed areas is recommended for better statistics. The image of the same failed area obtained by SEM is also shown in Fig. 4.15.

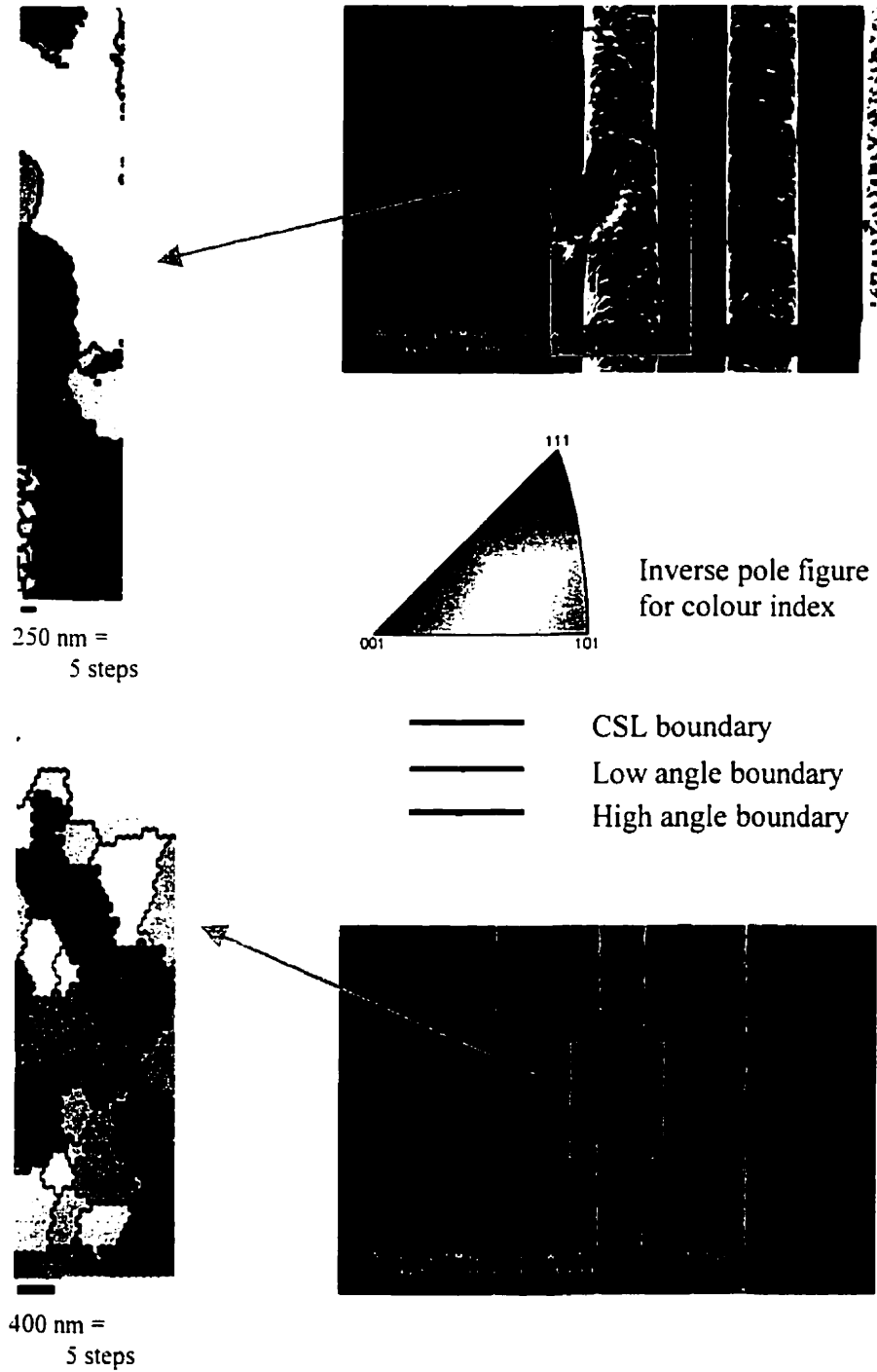


Figure 4.15. Grain boundary and orientation map of the failed area.

4.5. INFLUENCE OF MICROSTRUCTURE ON THE FILM RELIABILITY

The influence of microstructure (grain size and grain size distribution) is known to be important on the electromigration behavior in thin films [74, 91]. Figure 4.16 shows the orientation imaging microscopy (OIM) microstructure of each specimen and its grain size distribution. If the misorientation between two measurements is greater than 5 degrees, the measurements were considered to be from different grains. Different colors in the microstructure represent different orientations in this figure. The average diameter of grains for the specimen PIB2/1, PIB2/2 and SP2 are 1.21 μm , 1.06 μm and 1.14 μm , respectively. It seems that the specimen PIB2/1 has relatively larger grains than other specimens, even though the differences in grain sizes are not much. It is generally accepted that the median time to failure (MTF) increases with the grain size as shown in the equation 4.1. Considering this equation, the longest MTF is expected in the specimen PIB2/1 and the shortest MTF in the specimen SP2. However, this does not seem to agree well with the electromigration test data obtained as in Figure 4.7.

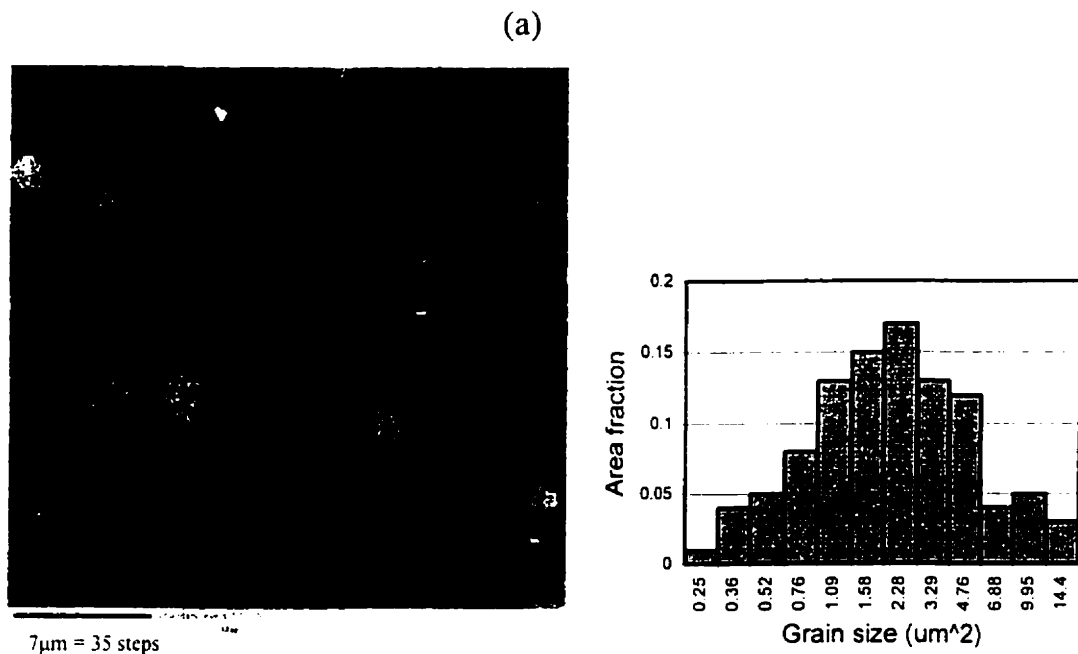


Figure 4.16. Microstructure and grain size distribution of the specimens: (a) PIB2/1,

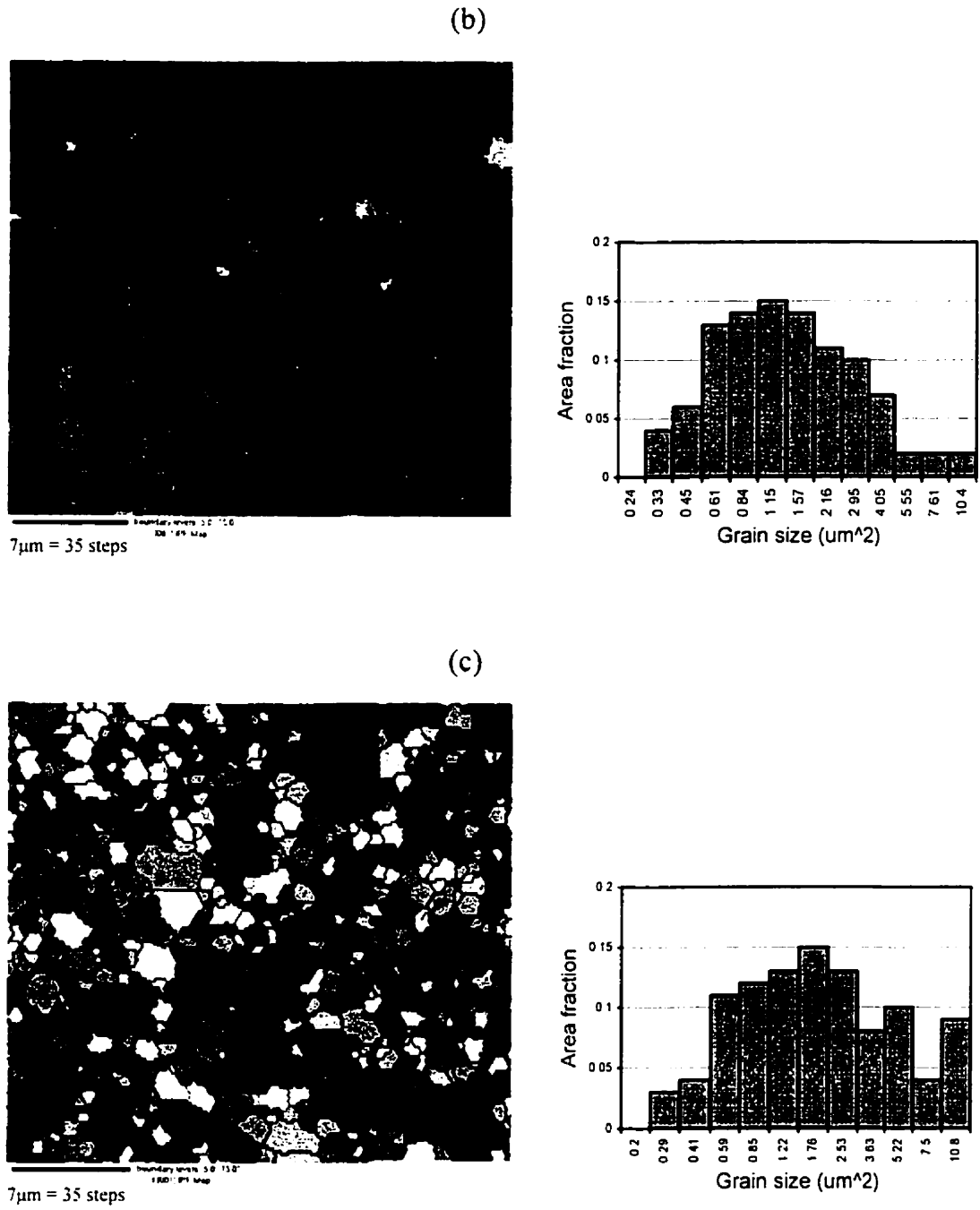


Figure 4.16. Microstructure and grain size distribution of the specimens: (b) PIB2/2, and (c) SP2.

The grain boundary is drawn depending on the differences in misorientation of two neighboring measurements in OIM. The misorientation definition for grain boundary drawing had been changed from 5 degrees to 2, 10, 15, 20 degrees for better statistics. Figure 4.17 shows the average grain size as a function of the misorientation angle, which defines a grain boundary, for three specimens. Equation 4.1 seems to correspond with the result obtained from the electromigration test when the misorientation angle for grain boundary drawing increases over 10 degrees. However, the data with high degrees of misorientation, such as 20 degrees, is not much reliable because it assumes several neighboring grains having similar orientation to one grain. For example, the PIB2/1 specimen has one grain, using the 20 degrees definition, which covers about 27% of the scanned area. Generally, 5 to 10 degrees of misorientation angle is chosen for the grain boundary drawing since it gives relatively reliable results. In this study, the misorientation angle was limited to 5 degrees in most cases. According to equation 4.1, the MTF is proportional to the grain size of the specimen. However, the grain size effect on MTF seems to be smaller than other effects such as texture and grain boundary character distribution, considering the fact that there are not many differences in grain size of each specimen. There is less than 15% difference in diameter of each specimen obtained with 5 degrees of grain boundary definition, and even with 10 degrees of grain boundary definition, there is only about 30% differences in diameter of each specimen.

One important factor that must be considered in the Figure 4.17 is the clustering of grains having similar orientations. For the specimen PIB2/1, the average grain size is drastically increased with increasing misorientation angle. The specimen PIB2/2 shows similar trend with the specimen PIB2/1. However, in the case of the specimen SP2, the change in average grain size is minor and seems to be independent of the misorientation angle. If the orientation of neighbor grains in textured materials were randomly distributed without any orientation clustering, the average grain size would be independent of the misorientation angle that defines a grain boundary. However, if the orientation of neighbor grains had a preference for being small-angled with each other, the average grain size would increase with increasing misorientation angle defining a

grain boundary. That is, the orientation clustering is represented by the dependency of the average grain size on the misorientation angle that defines a grain boundary. Therefore, the specimen PIB2/1 shows severe orientation clustering while the specimen PIB2/2 has less. In the specimen SP2, there is virtually no sign of orientation clustering.

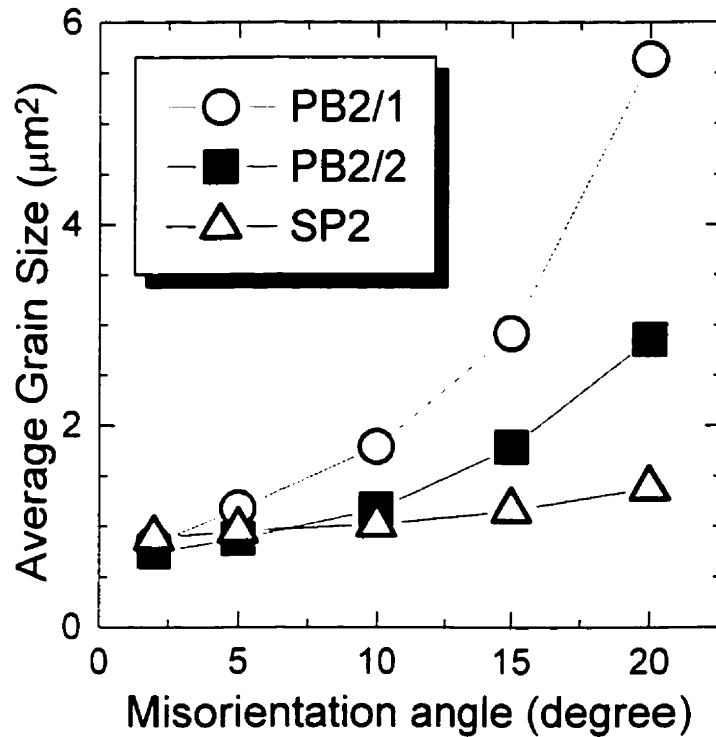


Figure 4.17. Average grain size as a function of misorientation angle [92].

As discussed in Chapter 4.4, the diffusivity along the low angle grain boundaries (LAGB) is less than that for high angle grain boundaries (HAGB) [79]. Therefore, the specimen that has more LAGB have lower diffusivity, so that the electromigration

failure is delayed. The possible reason that the orientation clustering increases the time-to-failure is also similar with the effect of the total frequency of LAGB on the electromigration failure as shown in Figure 4.10. If the orientation clustering were developed, the misorientation between grains becomes small and the total frequency of LAGB should be increased. Therefore, a longer time-to-failure is expected for the specimen.

Figure 4.18 shows the surface morphology of each specimen obtained by an atomic force microscopy. Each scan covers an area of $1\ \mu\text{m} \times 1\ \mu\text{m}$. As shown in this figure, PIB2/1 and PIB2/2 have similar surface morphology; the surface is essentially homogeneous with smooth surface features. However, SP2 has a rougher surface having round and sharp edges concurrently. There are many researches that relate grain size of films to their reliability. However, very little work has been done to determine the relationship between the surface roughness of films and their reliability. It seems that the effect of texture is more dominant in the case of PIB-2/1 and PIB-2/2. Local microstructure inhomogeneity can influence the local flux divergence and accumulation; for example, the large pyramidal protrusion would be a preferable area for hillock formation. It is suspected that the short electromigration lifetime of SP2 may be affected by its relatively rough surface.

There were many attempts to improve the structural properties of Al thin films by a variety of deposition techniques. It has been found that e-beam evaporated Al films at an elevated substrate temperature possess large grain size and that the grains have $\{111\}$ texture [91, 93]. A $\{111\}$ texture with a smaller grain size and a narrower grain size distribution was found in films deposited by a bias sputtering technique [94]. On the other hand, a $\{111\}$ texture accompanied by enlarged grain sizes of the film was found using the ionized cluster beam technique [95]. It is also reported that the simple partially ionized beam technique significantly improves the electromigration lifetime of Al films [96]. This corresponds well with the results obtained in this study.



(a) PIB2/1



(B) PIB2/2



(c) SP2

Figure 4.18. Surface morphology obtained by atomic force microscope (AFM) from: (a) PIB2/1, (B) PIB2/1, and (c) SP2.

The films deposited by partially ionized beam technique (PIB2/1 and PIB2/2) have longer electromigration lifetime than the sputtered Al film (SP2). Films deposited by the above-mentioned techniques all lead to better electromigration lifetime. Whatever technique is used, it is recommended to obtain the film with large grain size, a sharp {111} texture and a smooth surface. Having homogeneous grain size is also important since it gives a small standard deviation of grain size distribution.

4.6. CORRELATION BETWEEN THE TEXTURE OF FILMS AND THEIR STRESS-INDUCED RELIABILITY CONCERNS

It is well known that one of the major reliability concerns in thin film interconnects is the stress-induced failure. However, not much work has been carried out on the relation between film texture and its stress-induced failures.

Stress develops in aluminum interconnects because of thermal expansion mismatch between the substrate and the film. When Al or Al-base alloy interconnects are subjected to a thermal cycle during processing, they develop a characteristic stress-temperature profile as shown in Figure 4.19 [97]. The compressive stress during heating can produce thermal hillocks while the tensile stress on cooling drives the grain collapse and stress-induced voiding phenomena. All of above mentioned phenomena are speculated to be related to the texture of interconnects.

Hillocks appear as surface protrusions or side protrusions in lines as shown in Figure 2.18 and Figure 4.20. They are due to a stress relief mechanism where grain boundary diffusion and plastic flow are implicated as the deformation process. According to the model by Sanchez et al [98], Al interconnects undergo sufficient straining to induce yielding during typical thermal cycles and the yield stress is dependent on grain orientation. They suggested that the large compressive stress gradients between $\{110\}$ and $\{111\}$ oriented grains lead mechano-diffusional mass flux from the boundary regions surrounding $\{111\}$ grains to $\{110\}$ oriented grains. As a result, the growth of the $\{110\}$ grains out of the film plane producing hillocks is driven and thus partially relieves the compressive stress. Schwarzer et al [99] later found out that hillocks are formed on grains deviating from the $\{111\}$ fiber texture of sputtered Al interconnects.

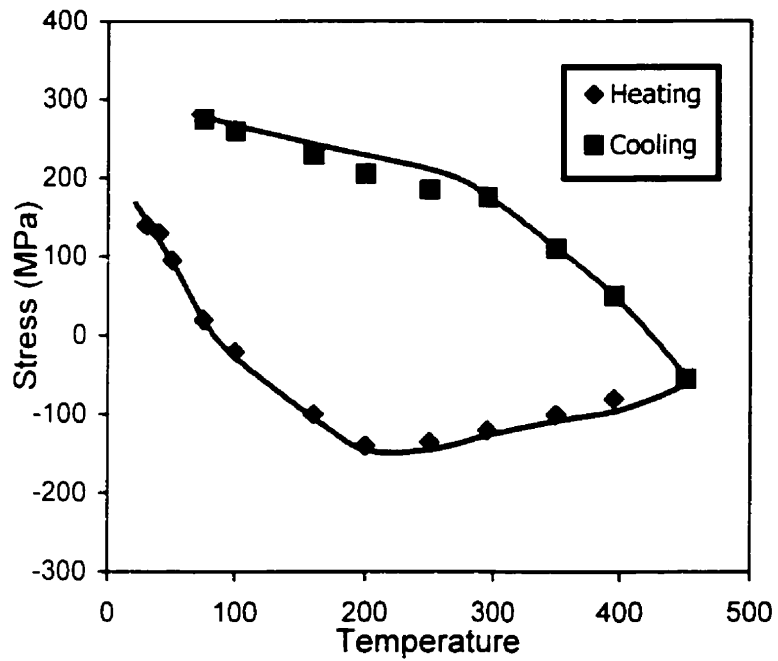


Figure 4.19. A stress-temperature profile for an Al-Si film deposited at 150°C.



Figure 4.20. A typical morphology of hillocks on the patterned line.

Grain collapse is a localized stress relaxation phenomenon, which occurs in Al interconnects under tension. The relaxation mechanism of the tensile stress is plastic yield by dislocation slip in some individual grains. A study [100] of this phenomenon shows that local deformation on the scale of an individual grain causes that grain to be depressed relative to the surrounding grains. The same phenomenon is usually observed, to some extent, in any film that is thermally cycled such that stress becomes tensile on cooling. No direct experimental evidence of orientation effects has been obtained, but modeling work suggest that texture is responsible. Grains with a {111} orientation have higher elastic constant than that of grains with other orientations [99, 100]. Thus, non-{111} grains would experience initial yielding while {111} grains would remain primarily elastic. The accommodation of the inelastic deformation accounts for the collapse. This process implies that grains with random orientation, i.e., grains with orientation away from {111}, are preferred sites for grain collapse.

Stress-induced void formation is a significant failure mechanism in narrow lines with less than 1 μm of line width. A tensile triaxial stress state develops in lines encapsulated with insulating dielectrics such as SiO_2 or Si_3N_4 . The stress is relieved during high temperature exposure by diffusive flow and damage to grain boundaries occurs in the form of slit and wedge-type voids. It was noted that {111} planes are found along the face of the voids because of surface energy minimization [101]. Therefore, specific boundaries are prone to be damaged where void volume is minimized [102]. Kordic et al [103] also found that the amount of stress-induced voids increases as the {111} texture weakens. It is speculated that control of local orientation would be an effective method to minimize stress voiding. However, there are no definitive experimental work or modeling studies that exist to quantify the extent of the texture effect.

Figure 4.21 shows the correlation between the intensity of {111} texture and the residual stress in the specimens PIB2/1, PIB2/2 and SP2. This figure shows that the residual stress of the films decreases as the intensity of the {111} texture increases. It is

important to have less stress in the film interconnects since residual stress is accumulated during processes and actual use as the thermal cycle (Fig. 4.19) is repeated.

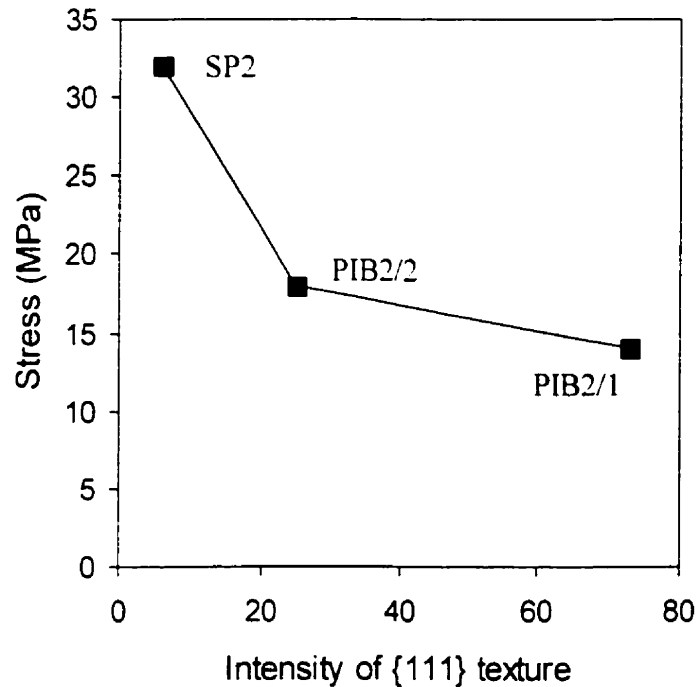


Figure 4.21. Correlation between the intensity of {111} texture and the residual stress.

The relation between the residual stress of films and their median time-to-failure (MTF) is shown in Figure 4.22. The MTF of interconnects decrease with the increasing stress. It seems that the stresses of the films contribute their influence on MTF. According to Kaneko et al [101], the vacancy formation energy is reduced by tensile stress, and the amount of energy reduction is determined by the specific volume of vacancies in the

metal lattice. This means that excess vacancies seriously affect the diffusion constant, enabling faster metal atom migration and faster void growth and thus shorter life time.

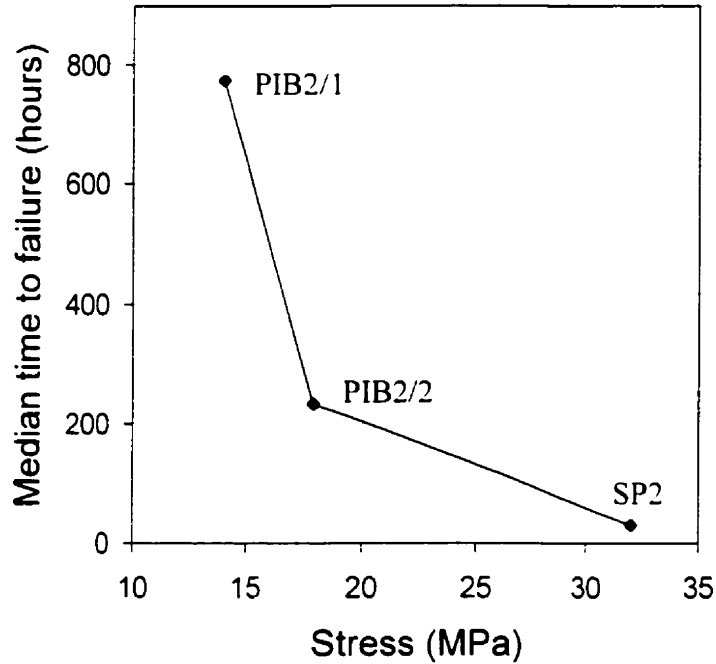


Figure 4.22. Median time to failure (MTF) as a function of residual stress.

It is generally assumed that texture plays an important role on the reliability of thin film interconnects and that a strong {111} texture is desirable to improve reliability. Although the importance of the {111} texture on electromigration behavior has been well established, the effect of texture on stress-induced failure has not been clearly understood. More detailed work is necessary to fully understand the correlation between the texture of films and their stress-induced failures.

4.7. MONTE CARLO SIMULATION OF THE TEXTURE DEVELOPMENT IN ALUMINUM THIN FILMS

It has been shown in Chapter 4.3 that strong $\{111\}$ texture in aluminum film increases its median time to failure. It is now necessary to know what are the optimum conditions to obtain strong $\{111\}$ texture during film deposition. A three-dimensional model based on Monte Carlo simulation of texture formation in Al film deposition is suggested for this purpose. Important parameters considered in this study are the surface temperature, the impingement rate of source atoms, the anisotropy of the surface energy, and the interface energy.

The basic processes on the surface of substrate in the initial stages of thin film growth are shown in Figure 4.23.

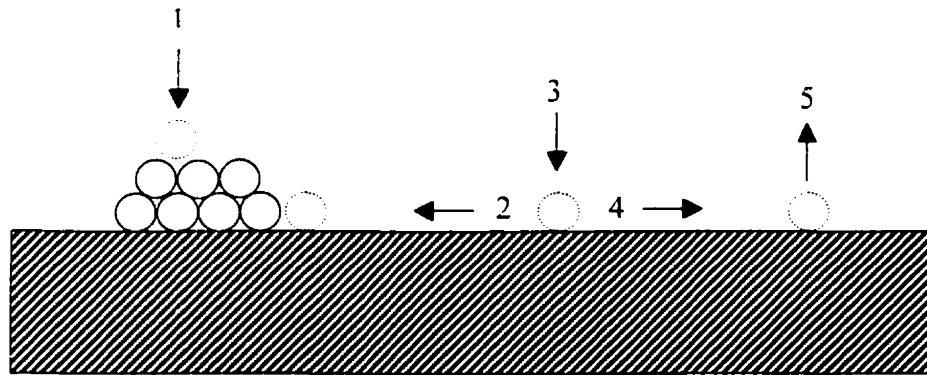


Figure 4.23. Processes on substrate in the early stages of thin film growth:

1. Impingement on nucleus
2. Diffusion to nucleus
3. Impingement on substrate surface
4. Diffusion on substrate surface
5. Re-evaporation

As shown Fig. 4.23, a single atom will stick at its current site or move to a neighboring site. It can also re-evaporate to the atmosphere. Several atoms can join to form small clusters on the surface of the substrate and be considered as nuclei after they reach a stable size. What is meant by "stable size of nucleus" depends on the interfacial energy between the nucleus and substrate and the surface energy of nucleus and substrate [104] as shown in Figure 4.5. Because of this relation, nuclei with low surface energy and interface energy will form more often than nuclei with higher energy. The surface and interface energy depends on the crystallographic orientation of the nucleus. As the nuclei grow after initial nucleation, the interaction between the substrate and deposits slowly diminishes. The growth rate of grains having different orientations is then influenced by the anisotropy of the surface energy of each grain.

For the Monte Carlo simulation, a 3-dimensional cubic array of sites is used to map the thin film. Each site is assigned an integer value, Q , which corresponds to the crystallographic orientation of site. The Q -value of every site is initially 0. It represents that the site is not occupied. As the deposition takes place, the Q -values of sites are changing from 0 to positive integer values. A different value represents a different orientation. An occupied site is referred to as a Monte Carlo block (MC-block).

There are two main parts to the procedure of Monte Carlo simulation. One is the deposition of MC-blocks and the other is the Monte Carlo scanning (MC-scanning). A specified number of MC-blocks are randomly deposited on the substrate surface before the MC-scan. The orientation (Q) assigned to each MC-block is chosen randomly from a given set of orientations. The MC-scanning is the heart of the procedure. A scan is performed after each deposition and consists of a specified number of trial jumps and rotations. The sites are randomly picked on the surface of the system if there is at least one MC-block deposited on these sites. These MC-blocks are then determined to be either a trial rotation or trial jump. The probability of occurrence of these two is equal. A simple procedure is used to determine whether it is a jump or a rotation. First, the local energy of MC-block at the original site with the original orientation, E_1 , is

calculated. If this MC-block has moved to a neighboring site having a different orientation, the new energy of the MC-block, E_2 , is calculated. If the MC-block at the new site has lower energy than that of the original site,

$$\Delta E = E_2 - E_1 \leq 0, \quad (4.2)$$

and this movement from a higher energy site to a lower energy site is accepted as a fact. If $\Delta E > 0$, this movement can also be accepted, but only according to the probability function, P .

$$P = \exp\left(-\frac{\Delta E}{k_B T_S}\right) \quad (4.3)$$

where k_B is the Boltzmann's constant and T_S is the temperature of the substrate. A random number is chosen between 0.0 and 1.0. If this number is less than P , the movement to the new site is accepted, i.e., the MC-block is left at the new site. The local energy of MC-block, E , is calculated as the sum of the interfacial energies between the MC-block and all of its neighboring sites. If there is no MC-block at the neighboring site, only the surface energy is taken into account.

$$E = \sum_{mn} \gamma_{Q_i Q_j} \quad (4.4)$$

where $\gamma_{Q_i Q_j}$ is the interfacial energy between the MC-block and its neighboring site. Each MC-scan consists of a number of trial rotations and jumps. This number represents the surface mobility. The higher number of trials corresponds to the higher surface mobility. Another deposition of MC-block takes place and MC-scan is repeated until the desired number of MC-blocks is deposited.

The influence of deposition rate and substrate temperature on the changes of film texture during aluminum deposition was analyzed. Nine aluminum orientations were taken into account for this work. The surface energy of these grains was calculated and

is listed in Table 4.1. The surface energies of each orientation were calculated by the ADESH (atomistic defect simulation handler) program. This program uses Monte Carlo relaxation to simulate relaxed surface at a given temperature. The energy of a surface is calculated using the Lennard-Jones potential after the relaxation at 550K. The interface energy is assumed to be 0 eV/atom between two grains having the same orientation and 20 eV/atom between two grains with different orientations.

Table 4.1. Surface energy of nine aluminum grains used for the simulation
(at 550 K, calculated by ADESH program)

Orientation	Surface Energy (eV/atom)
111	0.865
110	0.998
100	1.082
332	1.095
221	1.137
211	1.142
320	1.187
321	1.25
210	1.276

The results of the simulation with varying deposition rates are shown in Figure 4.24. The deposition rate increases as the number of blocks per each scan increases. At a high deposition rate, the deposited blocks experience more 'collisions' with other blocks and thus nucleation rate increases. As the nucleation rate increases, the average grain size decreases and the grains with low surface energy have less of an advantage to grow over other grains. The result is the development of a weak texture in this film. At a lower deposition rate, the deposited blocks have more time to find a low energy site to stick to. The low energy sites are usually the edges or the surface of grains having the same orientation. Therefore, grains grow larger and a strong texture is expected.

The surface mobility is another important parameter to be considered. The simulation has been done with different Monte Carlo Scan (MCS) parameters, which correspond to different mobility of atoms on the surface. As shown in Figure 4.25, the mobility of the deposited blocks increases as the MCS factor increases. This corresponds to an increase in the substrate temperature. The texture of the film is weak for the low MCS value because the deposited blocks have little time to find a low energy site before new blocks are deposited, thus introducing a higher number of nuclei. The deposited blocks have more time to find low energy site and texture of the film becomes strong when MCS value increases.

As shown in Figure 4.24 and Figure 4.25, the optimum conditions to obtain strong {111} texture are at low deposition rate and high surface mobility. Very strong {111} texture was obtained in the aluminum film with the low deposition rate and high mobility, as depicted in Figure 4.26.

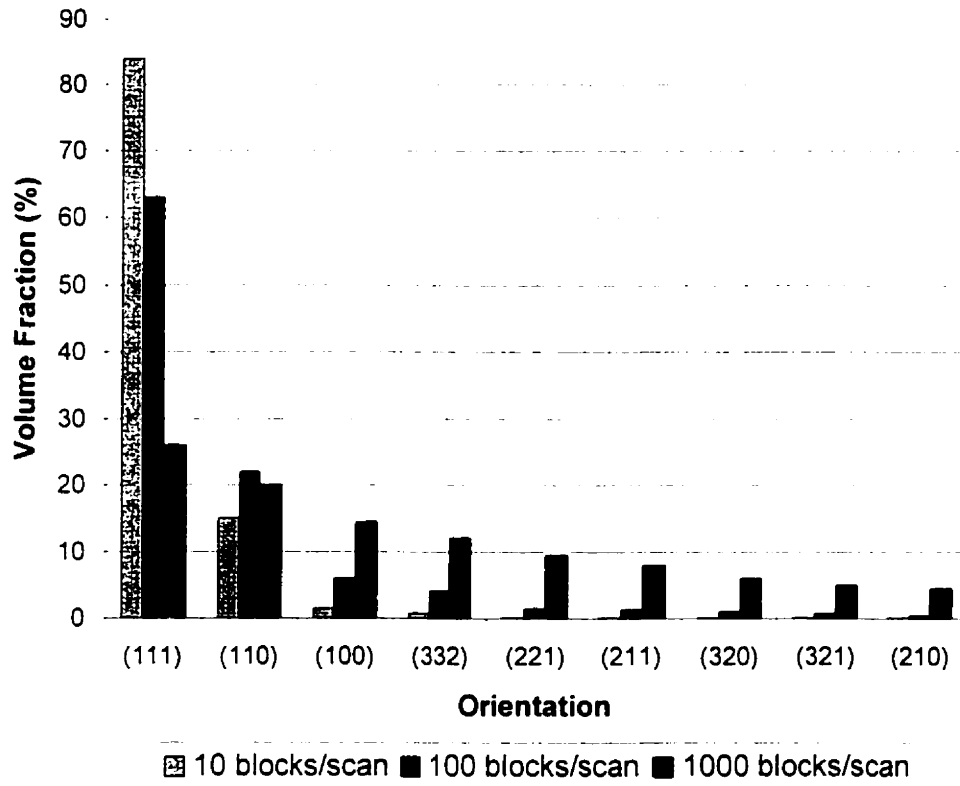


Figure 4.24. Volume fraction of differently oriented grains with different deposition rates.

Total deposition = 100,000 blocks, T = 550 K

MCS = 1 (The number of trials in each scan)

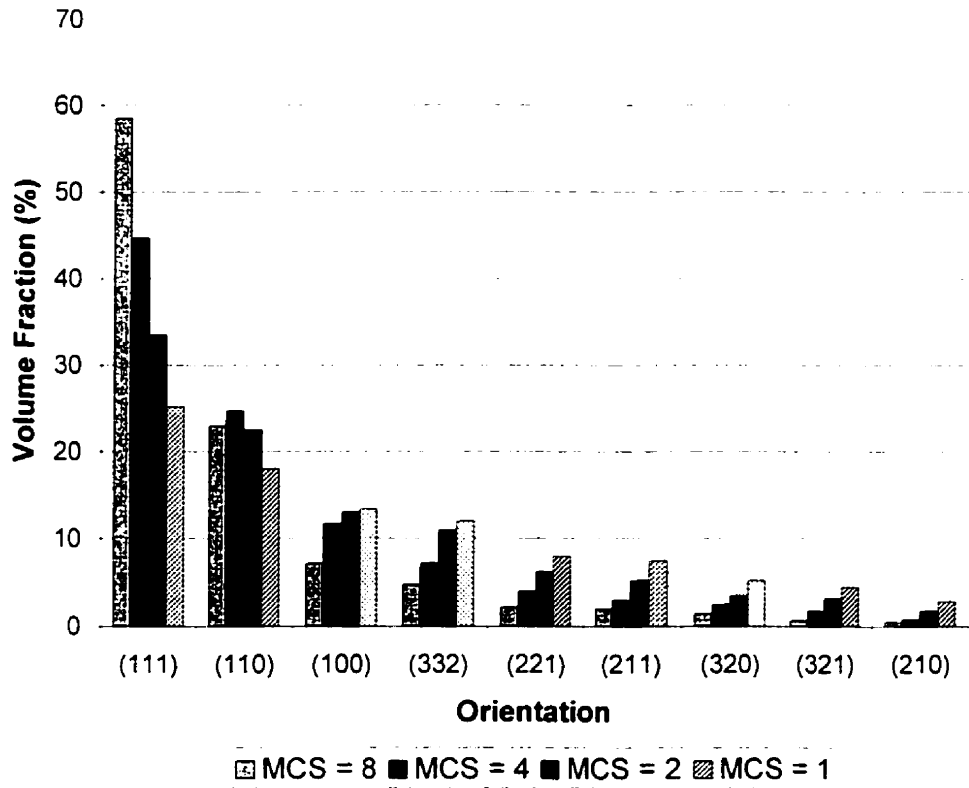


Figure 4.25. Volume fraction of differently oriented grains with different number of trials in each Monte Carlo scan.

Total deposition = 100,000 blocks, T = 550 K

Deposition rate = 1,000 blocks per scan

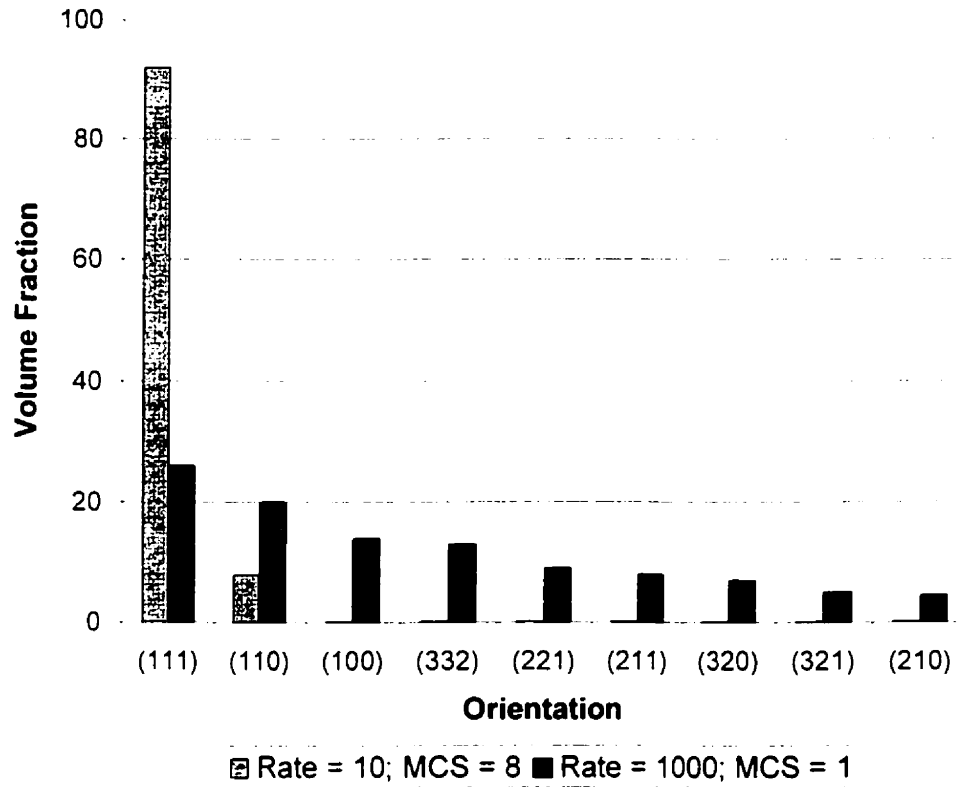


Figure 4.26. Volume fraction of differently oriented grains having different conditions during the film deposition.

Total deposition = 100,000 blocks. T = 550 K

4.8. SUMMARY

To understand the influence of texture on the reliability of aluminum interconnects, three aluminum specimens having different textures were studied. Results obtained from the electromigration test show that the strong $\{111\}$ texture in aluminum films improve their median time-to-failure.

The influence of the grain boundary character distribution and the CSL boundary distribution on the reliability of the aluminum interconnects was investigated because these boundary characteristics are closely linked to texture. The distribution of grain boundary misorientation angle and coincidence site lattice (CSL) boundaries were quantified using an orientation imaging microscopy (OIM). The experimental results showed that the specimen having the highest electromigration lifetime had a higher number of low angle grain and CSL boundaries than the other two. These boundaries are known to have low diffusivity. An analysis of the grain boundary characteristics around the failure areas seems to support this result. The high angle and non-CSL boundaries were connected to the failure areas in all the investigated specimens. Considering the fact that the number of low angle grain boundaries and CSL boundaries increases as the strength of $\{111\}$ texture increases, the strong $\{111\}$ texture in aluminum film is desirable to improve its reliability.

Microstructural analysis shows that the grain size of the investigated specimens was similar. However, the specimens having stronger $\{111\}$ texture are found to have an orientation clustering of grains, which contributes to the longer lifetime of the film by reducing the frequency of high angle grain boundaries.

A correlation between the texture of interconnect and its stress-induced reliability concerns had not been clearly understood. The experimental data obtained shows that the residual stress of films decreases as the intensity of the $\{111\}$ texture increases.

A model based on Monte-Carlo simulation of texture formation during the deposition of aluminum film was proposed to obtain the optimum conditions for the strong {111} texture development. The optimum conditions were found to be at low deposition rate and high mobility of atoms on the surface, which corresponds to high substrate temperature.

Chapter 5

The Influence of Texture on the Oxidation Kinetics of Copper

The object of this chapter is to improve the current understanding of the influence of substrate texture on the oxidation kinetics of copper interconnects and to suggest a method of reducing oxidation. The chapter consists of five sections. The first section introduces copper as an interconnecting material; reliability concerns such as high diffusion and oxidation rate are also discussed. The experimental procedures carried out for this study are described in the second section. Results obtained from the oxidation tests of copper single crystals are given in section 5.3. A discussion on the development of oxide texture and the changes of its morphology during oxidation is also provided in this section. A model that correlates the texture of polycrystalline copper with its oxidation kinetics is suggested in section 5.4. Section 5.5 is a synopsis of Chapter 5.

5.1. INTRODUCTION

Interconnects are commonly made of aluminum since this metal provides low electric resistivity and fabrication feasibility. However, the increasing trend in making electronic devices smaller requires the use of higher current densities, thus making it difficult to continue to use aluminum interconnects, as they are susceptible to electromigration failure.

Copper has been studied extensively to replace aluminum because of its lower resistivity and higher resistance to electromigration failure. The low resistivity is an important criterion in high-performance microprocessors because it enables signals to move faster by reducing the so-called “RC” (resistance \times capacitance) time delay. Copper lines conduct electricity with about 40% less resistance than aluminum ($1.67 \mu\Omega \times \text{cm}$ for copper, versus $2.65 \mu\Omega \times \text{cm}$ for aluminum). This translates to a speed-up of as much as 15% in microprocessors with copper interconnects when compared to those with aluminum interconnects. Copper enables a reduction not only in the ‘resistance’ part of the RC time delay, but also in the ‘capacitance’ part, since the metal line can be made thinner by using copper. This helps to reduce the amount of power consumption, which makes copper attractive to use in battery-powered applications such as notebook computers. As mentioned above, another benefit of copper is its superior resistance to electromigration failure when contrasted with aluminum. This is due to copper atoms being heavier and more tightly bound than aluminum atoms. Copper lines can then handle higher current densities, such as those found in high-power transistors. Also, a tighter packing density per level can be achieved by using narrower copper lines. This means that fewer layers of metal are needed to construct a chip, which lead to significantly reduced manufacturing costs. In fact, only about half of the metal layers are needed when using copper in comparison to aluminum as shown in Figure 5.1. One disadvantage in using copper is the fact that generating patterns in blanket copper films by etching processes can be very difficult. However, IBM has recently developed a new patterning method called “Damascene” that accompanies

copper electroplating [106 - 109]. IBM reported that the damascene approach requires 20–30% fewer manufacturing steps than traditional subtractive patterning using aluminum, and thus, may lead to a potential cost saving of up to 30% for the metallization process, or, 10–15% for the full wafer manufacturing [106].

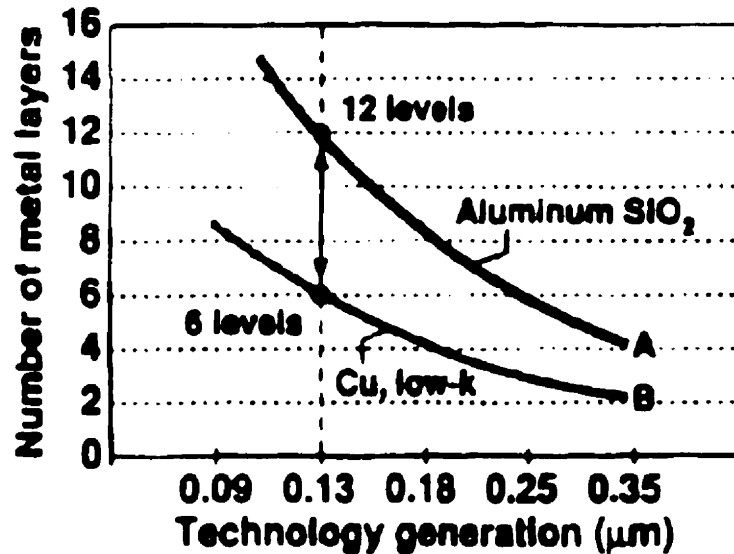


Figure 5.1. Reduced complexity; one of the main benefits of copper [105].

Despite the many advantages of copper, the substitution copper for aluminum as an interconnecting material has not been fully accomplished yet (e.g. the first commercial microprocessor using copper only came out to market in 1999) due to several reasons. One cause is that it diffuses very fast to both oxides and silicon. If there are no obstacles to block it, copper atoms can reach the source/drain/gate area and destroy the device. To prevent copper from reaching silicon areas, copper lines and plugs must be totally sealed at all locations and at all levels. Barrier layers must be effective against copper diffusion and simultaneously be thin enough to maximize the advantage that a small cross-section of copper represents. They should also be good adhesion layers for

copper deposition, and easy to remove during chemical mechanical polishing (CMP). So far, the best known barriers are either Ta or TaN deposited by physical vapor deposition (PVD) or chemical vapor deposition (CVD). Another disadvantage in using copper is that this metal cannot be readily patterned using conventional subtractive plasma etching because of the lack of volatile halide by-products. Therefore, using it requires the implementation of an entirely new manufacturing technique, i.e., the IBM damascene method, as mentioned before. Although there was a report of potential cost savings with the damascene method [106], copper metallization is not necessarily a simpler alternative to aluminum. The manufacturing price should be determined by considering all aspects of the technology currently used. A third problem with using copper is that it readily oxidizes under standard chip fabrication conditions (in air, at relatively low temperature, i.e., $< 200^{\circ}\text{C}$) and does not form a stable self-protective oxide layer similar to Al_2O_3 on aluminum that would stop further oxidation and erosion. The formation of copper oxides degrades the electrical and mechanical properties of copper.

Extensive studies have been performed on the oxidation of copper in the 50's and 60's [14, 61, 62, 110 – 112]. In the 90's, the study of copper oxides intensified due to the interest in using copper as an interconnection material. Some methods have been suggested to protect the oxidation of copper film, such as passivating copper with a protection layer [15] or adding alloying elements [16]. It is generally accepted that the oxidation of copper is anisotropic and depends on the orientation of the copper substrate. However, there has not been much work studying the influence of the texture of polycrystalline copper substrate on its oxidation kinetics.

If a relationship between substrate texture and copper oxidation kinetics exists, then measuring texture could be a method of predicting the copper oxidation. The conventional method of evaluating copper oxidation is by performing an oxidation test, which is destructive by nature. Apart from giving information about oxidation, texture

measurement could also give useful information about other physical, chemical and mechanical properties of copper interconnects.

The remainder of this chapter attempts to improve the understanding of the oxidation kinetics of copper interconnects, and suggests a method to reduce copper oxidation. Copper single crystals having different orientations were oxidized and the results obtained from the oxidation tests were analyzed. The influence of substrate orientation on the development of oxide texture and its morphology were also studied. A quantitative model was proposed to predict oxidation kinetics of copper from the texture of the specimens.

5.2. EXPERIMENTAL PROCEDURES

5.2.1. Sample Preparation

Pure copper single crystals were provided by the Institute of Metallurgy and Materials Science, a division of the Polish Academy of Science in Kraków, Poland. Six copper single crystals having different orientations were carefully selected. The single crystals had the (100), (110), (111), (123), (311) and (314) faces parallel to the surface. Copper plates of 99.999% purity were used as polycrystalline specimens. The grain size and texture of the plates were measured, and three specimens having similar grain sizes but different textures were selected. The single crystals and the polycrystalline specimens were cut and polished mechanically with metallographic polishing papers to P1200. These specimens were then electrolytically polished in a solution of 165 ml of phosphoric acid (H_3PO_4 , 85%) and 35 ml of distilled water for 30 minutes to remove strained layers. The current density was set $0.06 A/cm^2$. It was very important at this point to obtain a flat and clean surface before the oxidation test since remaining impurities and scratches can change oxidation patterns. Texture measurements were carried out again for the polished specimens to confirm that there have been no changes in their orientation during the polishing process. The size of specimens prior to the oxidation test was about 1.2 cm width \times 2 cm length \times 0.1 cm thickness.

5.2.2. Oxidation Test

The Thermogravimetric Analyzer (TGA) TG-171 from Cahn Instruments Inc. was used to obtain details on the oxidation kinetics of the copper specimens. Analyzed specimens were placed inside a platinum specimen holder, which was positioned inside the furnace and hung on an extension sapphire rod connected to a microbalance (Figure 3.9). A heating rate of $10^\circ C/min$ was used to reach $200^\circ C$, following which the specimens were incubated for about 9 hours. Air provided the oxidative atmosphere at a flowing rate of 80 ml/minute. A Type K thermocouple was used to detect the

temperature inside the furnace. The weight of the specimen and the temperature were recorded every 60 seconds by the computer controlling the TGA system. A detailed description of the TGA is given in Chapter 3.4.

5.2.3. Texture Measurement

The texture of the copper specimens was obtained by the Siemens texture measuring system described in Chapter 4.2.3. The Siemens' 2.0 kW molybdenum target tube was run at 40 kV and 40 mA. The (111), (200) and (220) pole figures of the specimens were obtained. From the pole figure data, the coefficients of orientation distribution function (ODF) were calculated using the incomplete pole figure method [70].

The texture of the oxides on the single crystal specimens could not be measured by the Siemens system since the machine is not equipped with a monochromator. When measuring the texture of a thin layer (less than several micrometers of thickness) on a single crystal substrate without the use of a monochromator, a pole figure having mixed intensities from both the thin layer and the substrate can be expected [69]. Usually, the intensity from the single crystal substrate, which is not wanted, is stronger. Therefore, the texture of the oxides on single crystals was measured by using the Rigaku rotation anode X-ray generator (RU-200BH) with a copper target, described in Chapter 4.2.6.

It is generally difficult to obtain a distinct diffraction pattern from thin oxide layers because the diffracted x-ray beam is weak, which results in a relatively high background. Therefore, the oxide films on single crystals were characterized using the x-ray diffractometer set-up with a 1° grazing angle to increase the intensity of x-ray diffracted from the oxides. The tube voltage was 50 kV and the tube current was 150 mA. A step-size of the goniometer was set to 0.024 degrees and the counting time was 10 seconds for each angular step.

Grazing incidence diffraction patterns of oxides on single crystal specimens oxidized at 200°C for 1 minute, 30 minutes, 3 hours and 9 hours were obtained. Only diffraction peaks from {111}, {200}, {220} and {311} oriented grains were considered because the diffraction intensity from other grains was too low to be analyzed.

It is to note that in actuality, the diffraction intensity does not represent the true texture of the specimens. To obtain the true texture, specimens of randomly oriented copper oxide (Cu₂O) powder were annealed at 200°C for 1 minute, 30 minutes, 3 hours and 10 hours, and the diffraction patterns of oxides were then acquired. Afterwards, each diffraction peak from the oxidized copper specimens was normalized with the diffraction peak from the Cu₂O powder. This was then translated to the volume fraction of each type of grain orientation, which represents the 'true' texture of oxides.

5.2.4. Microstructure Analysis

The polycrystalline specimens were polished with metallographic polishing papers up to P1200 and subsequently etched for 50 seconds in a solution of 20 ml of NH₄OH, 18 ml of H₂O and 2 ml of 30% H₂O₂. A camera attached to an optical microscope was used to evaluate the microstructure of the specimens.

The surface morphology of the oxide on single crystal specimens was obtained using Digital Instruments' atomic force microscope (AFM). Morphology changes during oxidation were thus used to investigate the influence of substrate orientation on oxidation. Several areas on each specimen were investigated and the surface roughness was calculated. The roughness (R_q) was defined as the standard deviation of the Z value (height) within the given area, and is written as

$$R_q = \sqrt{\frac{\sum (Z_i - Z_{ave})^2}{N}} \quad (5.1)$$

where, Z_i is the current Z value. Z_{ave} is the average of the Z value within the given area, and N is the number of points within the given area.

Various attempts were made to obtain the orientation of copper oxide grains by using orientation imaging microscopy (OIM), but this was not successful. The small size of the oxide grains, only several nanometers in the early stage of oxidation, and the rough surface morphology of oxides are speculated to be reasons for this failure.

5.2.5. Prediction of Oxidation Kinetics of Copper

A quantitative model was proposed to predict the oxidation kinetics of copper from the texture of the specimen. Details on this method are described and discussed in section 5.4.

5.3. THE INFLUENCE OF SUBSTRATE ORIENTATION ON THE OXIDATION KINETICS OF COPPER

5.3.1. The Oxidation Kinetics of Copper Single Crystals

The oxidation kinetics of copper single crystals having different orientation is illustrated in Figure 5.2. The single crystals have the (100), (110), (111), (123), (311) and (314) faces parallel to the surface. Only the Cu_2O phase was formed during the oxidation tests.

As shown in Figure 5.2, the crystal faces (100), (110), (123), (314), (111) and (311) represent, in that order, decreasing rates of oxidation. The oxidation rate of the (100) single crystal was much higher than that of the others in the early stage of the oxidation tests. This result seems to agree well with the works of Rhodin [62], Rustman [113] and Harris, et al. [114]. In the studies of Rhodin and Rustman, the order of faces was (100), (110) and (111), in decreasing order of oxidation rate, while in Harris' study, the relative order was (100), (111) and (311). In comparison, the work of Young, et al. [111] showed that the order was (100), (111), (110) and (311), again in decreasing order of oxidation rates. The oxidation of the (111) face was found to be higher than that of the (110), while the reverse was found in the other studies [62, 113]. Young et al. pointed out that a very small amount of impurities on the surface could change the oxidation kinetics and that the (110) face was especially susceptible to surface contamination. In all studies mentioned above, the (100) face was reported having a much higher oxidation rate than the other faces. Oxidation tests in the studies mentioned above had been carried out at temperatures below 200°C.

The oxidation kinetics of copper single crystals change in the case of high temperature oxidation. Bénard and Talbot [115] oxidized several copper single crystals at 900°C and the order of their faces in terms of decreasing oxidation rates was found to be (210), (221), (110), (111) (100) and (123). One possible cause for the difference in oxidation

kinetics at various temperatures can transpire from the type of oxide that is present. It is generally believed that Cu_2O is the only oxide formed at temperatures below $\sim 250^\circ\text{C}$ at 1 atm in air, whereas both Cu_2O and CuO are developed during oxidation at temperatures above $\sim 250^\circ\text{C}$, as shown in Figure 5.3 [116]. Although many theories on oxidation rate laws have been developed, no single rate law can explain all the data obtained from oxidation experiments of copper at different temperatures.

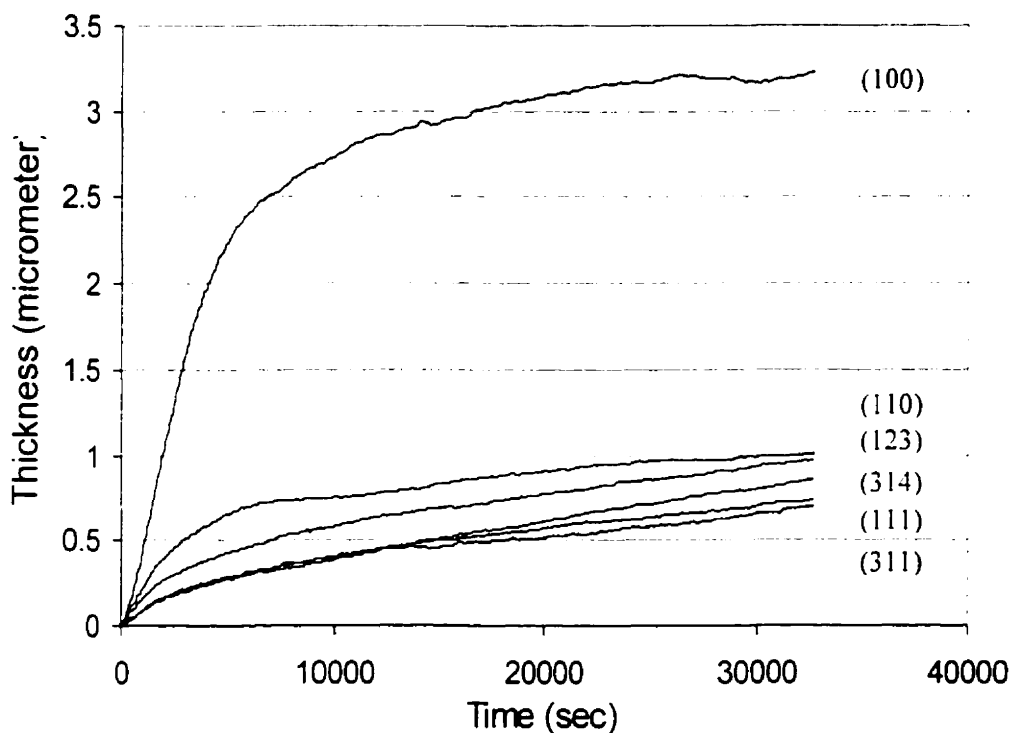


Figure 5.2. Oxidation kinetics of the copper single crystals having different faces, at 200°C .

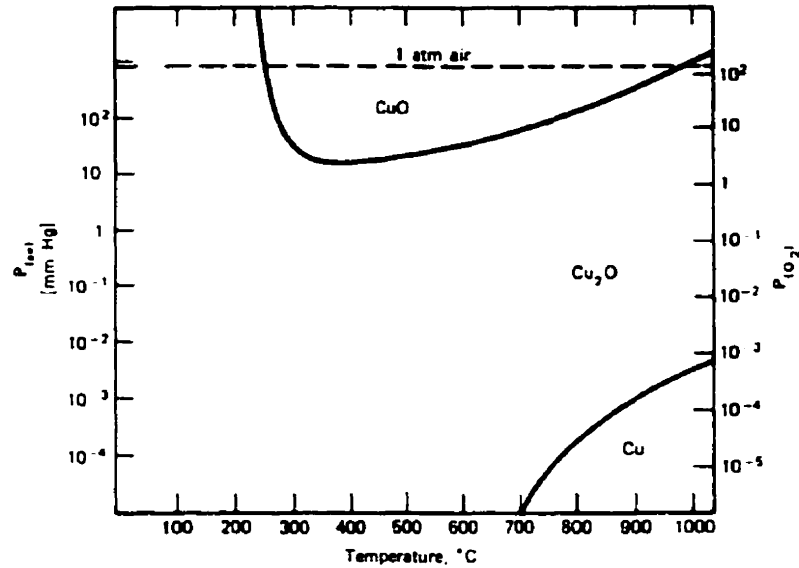


Figure 5.3. Pressure-temperature stability region for Cu₂O and CuO [116].

No single theory on copper oxidation can explain the anisotropic oxide growth on different crystal faces, although many suggestions have been made [117–120]. Lawless and Gwathmey [112] found that the oxide on the (100) face has four directional relationships with its substrate, which are $[1\bar{1}0]_{\text{Cu}_2\text{O}} // [1\bar{1}0]_{\text{Cu}}$, $[0\bar{1}1]_{\text{Cu}_2\text{O}} // [1\bar{1}0]_{\text{Cu}}$, $[01\bar{1}]_{\text{Cu}_2\text{O}} // [110]_{\text{Cu}}$ and $[1\bar{1}0]_{\text{Cu}_2\text{O}} // [1\bar{1}0]_{\text{Cu}}$, whereas there are two on the (111), namely $[1\bar{1}0]_{\text{Cu}_2\text{O}} // [1\bar{1}0]_{\text{Cu}}$ and $[\bar{1}10]_{\text{Cu}_2\text{O}} // [1\bar{1}0]_{\text{Cu}}$. The slowest oxidizing face, the (311), has only one orientational relationship with the oxide, ($[1\bar{1}0]_{\text{Cu}_2\text{O}} // [1\bar{1}0]_{\text{Cu}}$). i.e., the oxide can have only one orientation in this case. They suggested that this might account for a large difference in oxidation rates for different crystal faces. If the oxide nucleates on many surface sites, there is an equal probability that any of the four orientational relationships will occur. As the oxide grows, grain boundaries and a high concentration of structure defects develop at places where different oxide nuclei meet one another. Therefore, the oxide growth on a (100) face has more grain

boundaries and defects than others. These grain boundaries and defects are responsible for high rates of diffusion of copper ions towards the oxide surface and hence, a high oxide growth. They also reported that the misfit between the (311) face of copper and its oxide was 0.5%, relatively lower than that of others. The misfit here was defined as $b/a - 1$, where b and a are the distance between lattice points for the oxide and metal respectively in a given direction for which the misfit is being determined. Under the small misfit condition, the defect density in the oxide is at a minimum and the diffusion of cuprous ions is not facilitated by a high defect concentration.

The theory behind the oxidation kinetics of copper is rather complicated since the degree of oxidation varies with pressure, temperature, atmosphere and other factors. However, it is quite clear that the early stage of oxidation is very important since most of the oxidation takes place during this period.

5.3.2. The Changes in the Oxide Texture during Oxidation

Figure 5.4 shows the changes of the orientation of the copper oxide layer (Cu_2O) of each specimen during oxidation. Only the volume fractions of {111}, {100}, {110} and {311} grains were considered because the diffraction intensity from the grains of other orientations was too low to analyze.

In the early stage of oxidation as depicted in Fig. 5.4.(a), it can be seen that the fastest oxidation rates occurred on the (100) single crystal having an oxide of the {111} orientation. The oxides on the (110) and (111) single crystals also had a relatively large number of {111} grains in addition to {100} grains, while the oxides on the (123) and (314) single crystals had {111}, {100} and {110} grains. It was noticeable that the (311) crystal had a relatively large number of {311} grains in its oxide.

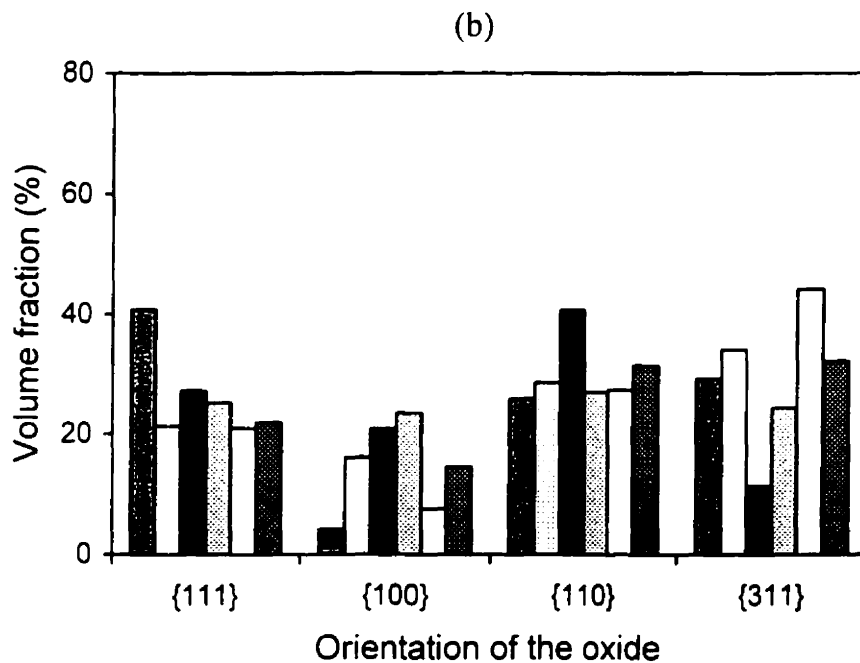
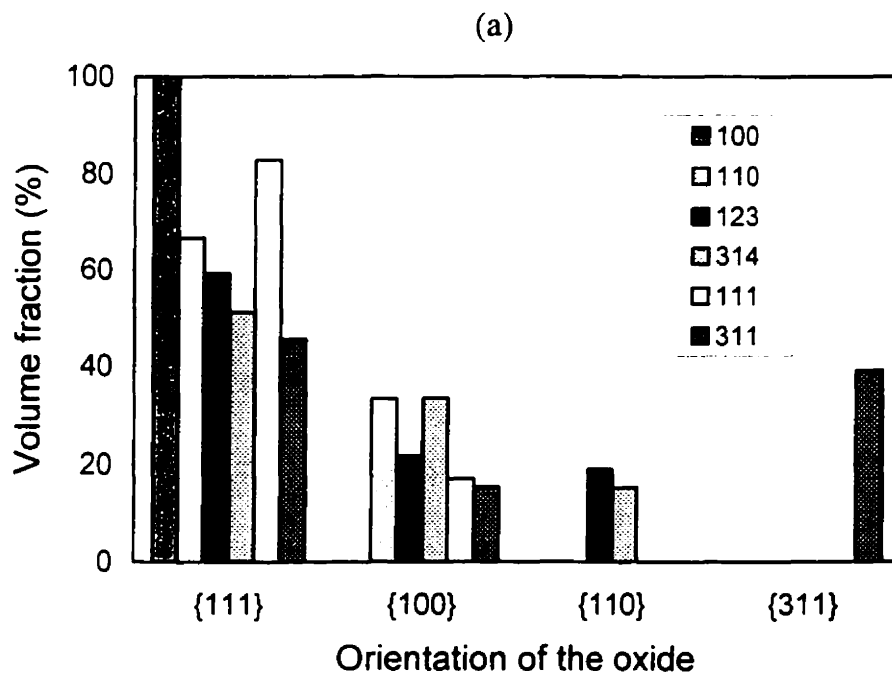


Figure 5.4. Volume fraction of different texture components in Cu₂O oxidized at 200°C for (a) 1 minute, (b) 30 minutes,

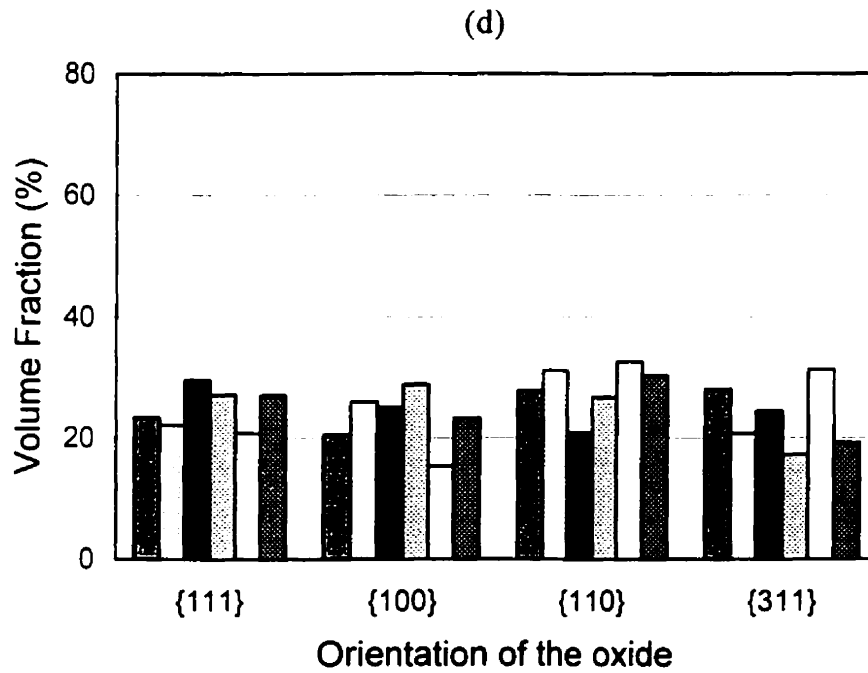
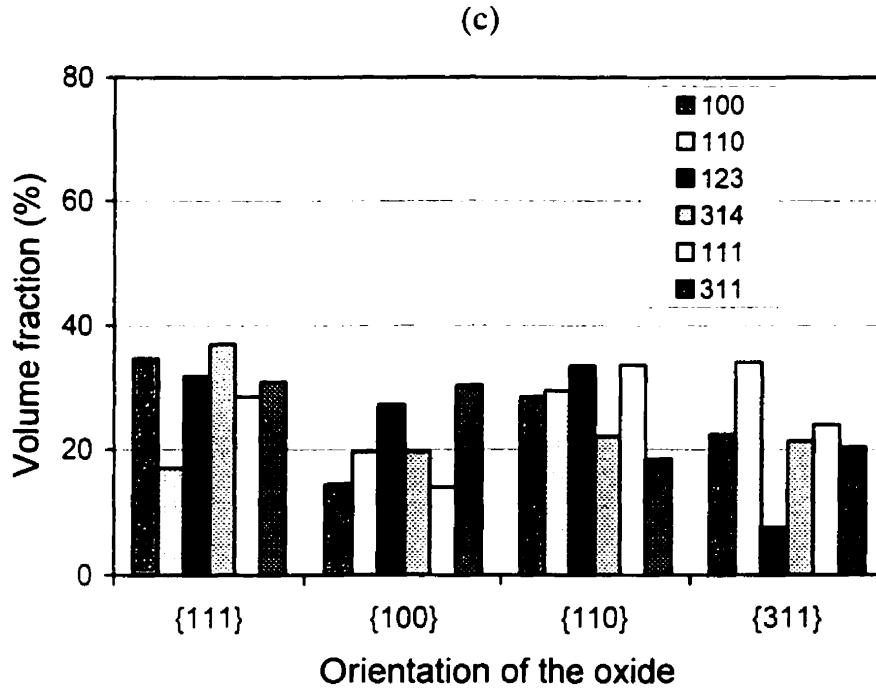


Figure 5.4. Volume fraction of different texture components in Cu_2O oxidized at 200°C for (c) 3 hours and (d) 9 hours.

According to Gwathmey [121] and Gorny [117], the {111} orientation of Cu_2O was found on the (100) and (111) faces of the copper substrate. Their work is in agreement with the results obtained in this study, although here, there was also a small number of oxide grains having {100} orientation on the (111) face. In an extensive study by Lawless and Gwathmey on the epitaxial relationship between copper substrate and its oxides [112], copper specimens having eight different orientations were examined. They found only one type of oxide orientation for each specimen, while two or three oxide orientations were observed in this study, except for the oxide on the (100) single crystal (Fig. 5.4.(a)). The thickness of the oxides in the above-mentioned reports [112, 117, 121] was in the range of 8–300 nm. The thickness of oxides was about 50–150 nm after 1 minute of oxidation in this study. It seems that the recrystallization had already started in the oxides, except on the (100) single crystal. The oxide on the (100) single crystal still seemed to have an epitaxial relationship with its substrate. It should be noted that the conditions of oxidation and the method of sample preparation deviated a bit from the previous works. Therefore, the results obtained in this study should not be strictly compared to other results.

As the oxidation time reached 30 minutes, the number of {110} and {311} grains increased in the oxides of all specimens, as shown in Figure 5.4.(b). However, the amount of {111} grains of Cu_2O was maintained high on the (100) single crystal. The thickness of oxides was about 150–900 nm in this stage. There were not many transformations in the orientation of oxides as oxidation proceeded. The copper oxide on all the specimens had an almost random orientation during the last stages of the test, as revealed in Figure 5.4.(c) and (d). It seems that the copper oxide was strongly oriented in the early stage of oxidation and began to lose the strength as its thickness increased.

5.3.3. The Changes in the Morphology of Oxides during Oxidation

The morphology of copper oxide (Cu_2O) after 1 minute, 30 minutes, 3 hours and 9 hours of oxidation is shown in Figure 5.5, Figure 5.6, Figure 5.7 and Figure 5.8, respectively. The roughness (RMS) of oxide on each specimen is given under each image. The dimension of each surface area was $1\ \mu\text{m}$ by $1\ \mu\text{m}$ and the height scale was 200 nm.

As shown in Figure 5.5.(a), a large number of fine oxide grains were observed in the (100) copper. The mean roughness of the oxide was 2.9 nm, which was relatively lower than that of the oxides on the other specimens. As mentioned before, the (100) face of copper is known to have a higher number of orientational relationships with its oxide, i.e., the oxide on the copper (100) face can have more diverse orientations [112]. If the oxide is nucleated at many places on the surface, there is an equal probability that any of these orientational relationships will occur. And thus, a larger number of oxide nuclei having different orientational relationships is expected on copper (100). This seems to be responsible for the fast oxidation of the (100) single crystal by introducing more grain boundaries and defects, which accelerate copper ion diffusion. The oxide on the (110) face seemed to have more relatively large grains than the other oxides. Its roughness was 9.6 nm, which was the highest among all investigated oxides. On the single crystal (111) and (311), several large oxide grains were found on the surface of small grains, as can be seen in figures 5.5.(e) and (f). These grains appeared to have recrystallized at a later stage and begun to grow with a morphology similar to that illustrated in Fig. 5.5.(b). In spite of the some differences in morphology, the variation in the thickness of oxides on different specimens in the initial stage of oxidation was relatively small (Figure 5.2).

Figure 5.6 shows the morphology of oxides after 30 minutes of oxidation. The oxide grains became much bigger in all specimens, and the growth of oxide grains on the (100) single crystal was especially significant. The cross-section of oxides on this

specimen after 1 minute and 30 minutes of oxidation is compared in Figure 5.9. The oxide on the (100) face is thicker than the others in this stage (Fig. 5.2). It seems that the oxide grew very rapidly on the (100) face during the time interval of 1 and 30 minutes.

The size of oxide grains and their roughness increased as oxidation carried on after 30 minutes; however, no dramatic changes in morphology were observed (Fig. 5.7). As shown in Fig. 5.8, the oxides on all specimens had similar morphology after 9 hours of oxidation. It should be noted that roughness did not necessarily correspond to the grain size of the oxide (Fig. 5.5(d) vs. Fig. 5.6(d)). Nevertheless, in most cases, the grain size of the oxide increased as its surface roughness increased.

The oxidation kinetics of copper single crystals having different orientations and the changes in oxide morphology were studied. Considering the results obtained from the oxidation tests and the analysis of oxide morphology, it is recommended that the {100} texture in copper interconnects be avoided in order to reduce copper oxidation.

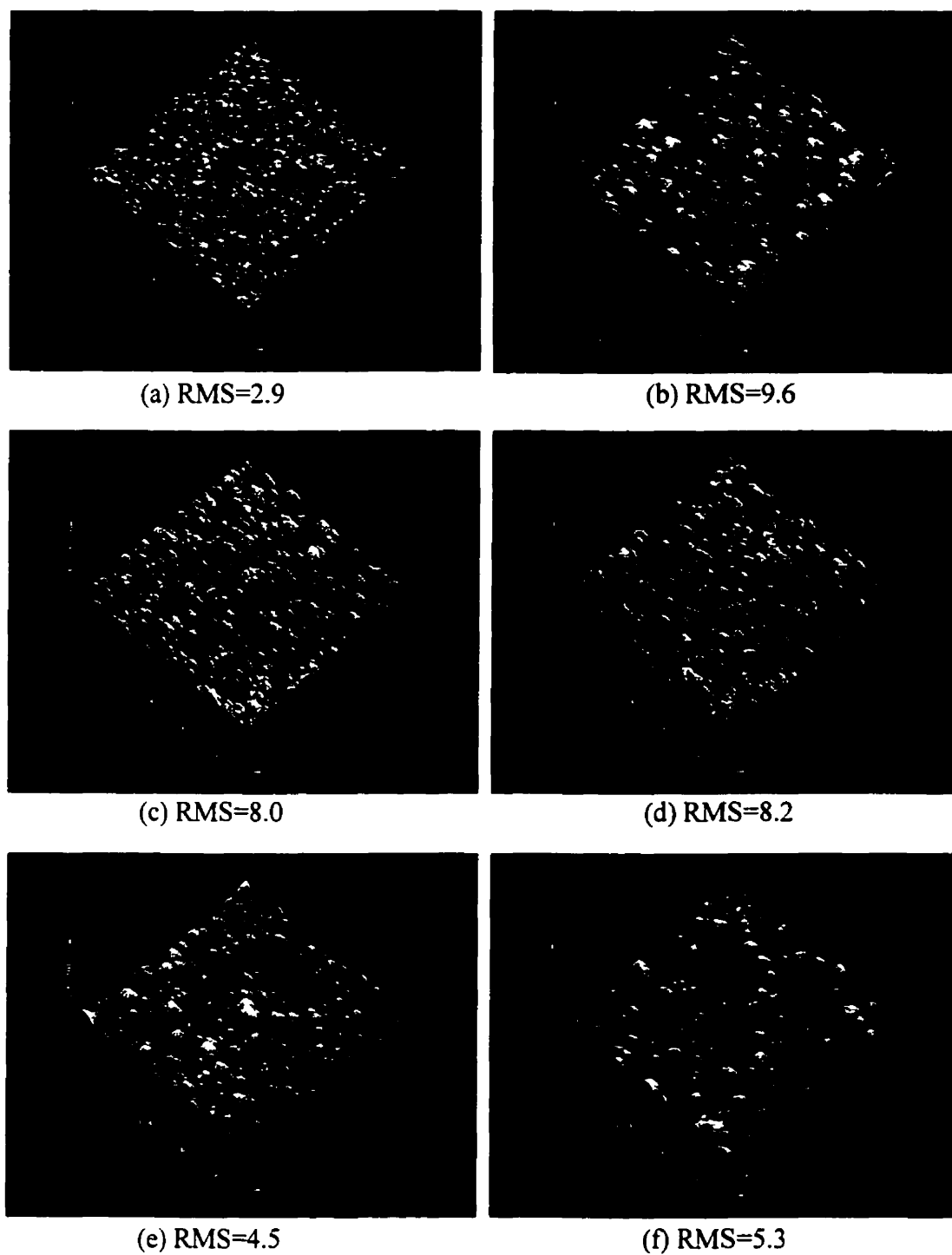


Figure 5.5. The morphology and roughness of oxide after 1 minute at 200°C on the (a) (100) face, (b) (110) face, (c) (123) face, (d) (314) face, (e) (111) face and (f) (311) face.

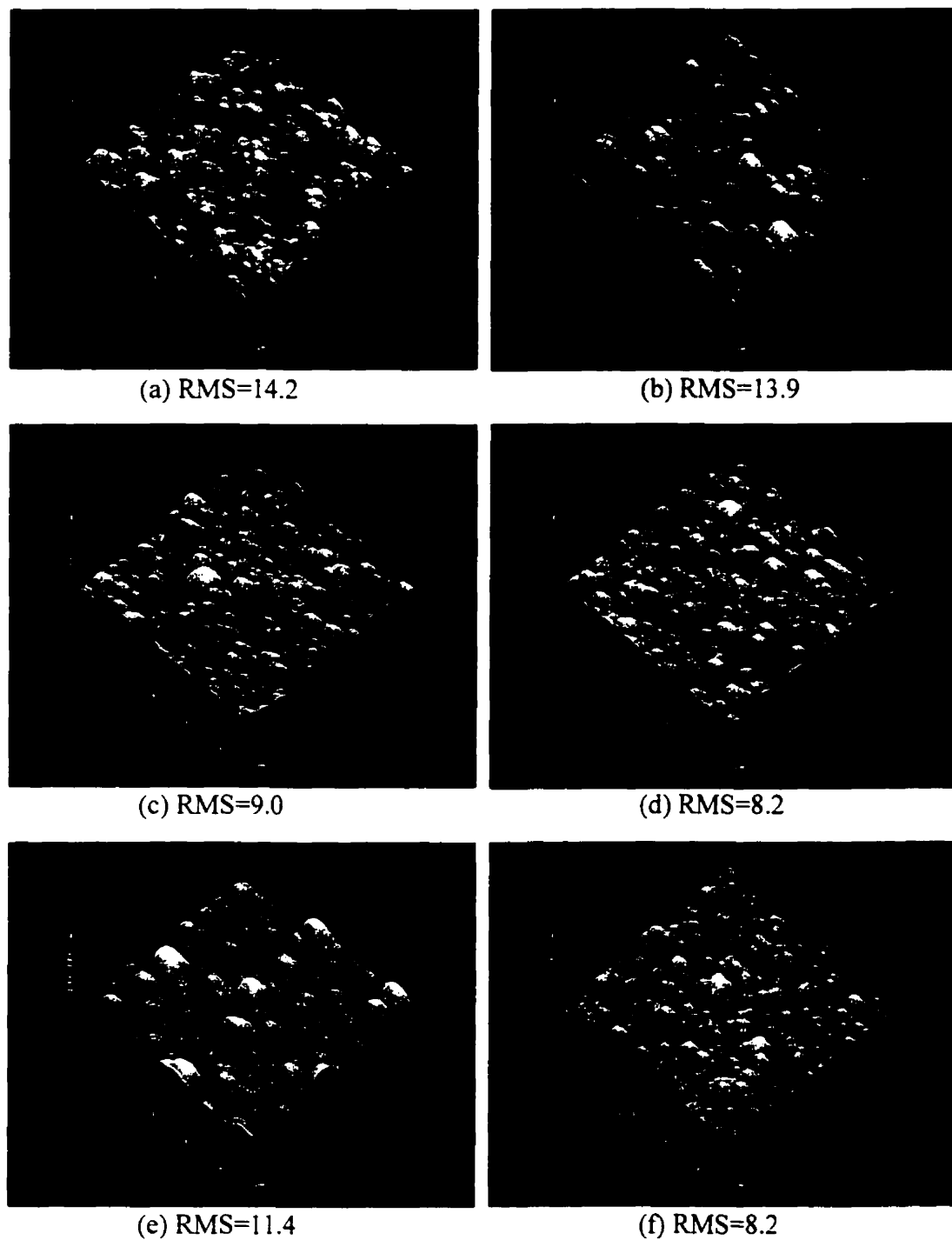


Figure 5.6. The morphology and roughness of oxide after 30 minutes at 200°C on the (a) (100) face, (b) (110) face, (c) (123) face, (d) (314) face, (e) (111) face and (f) (311) face.

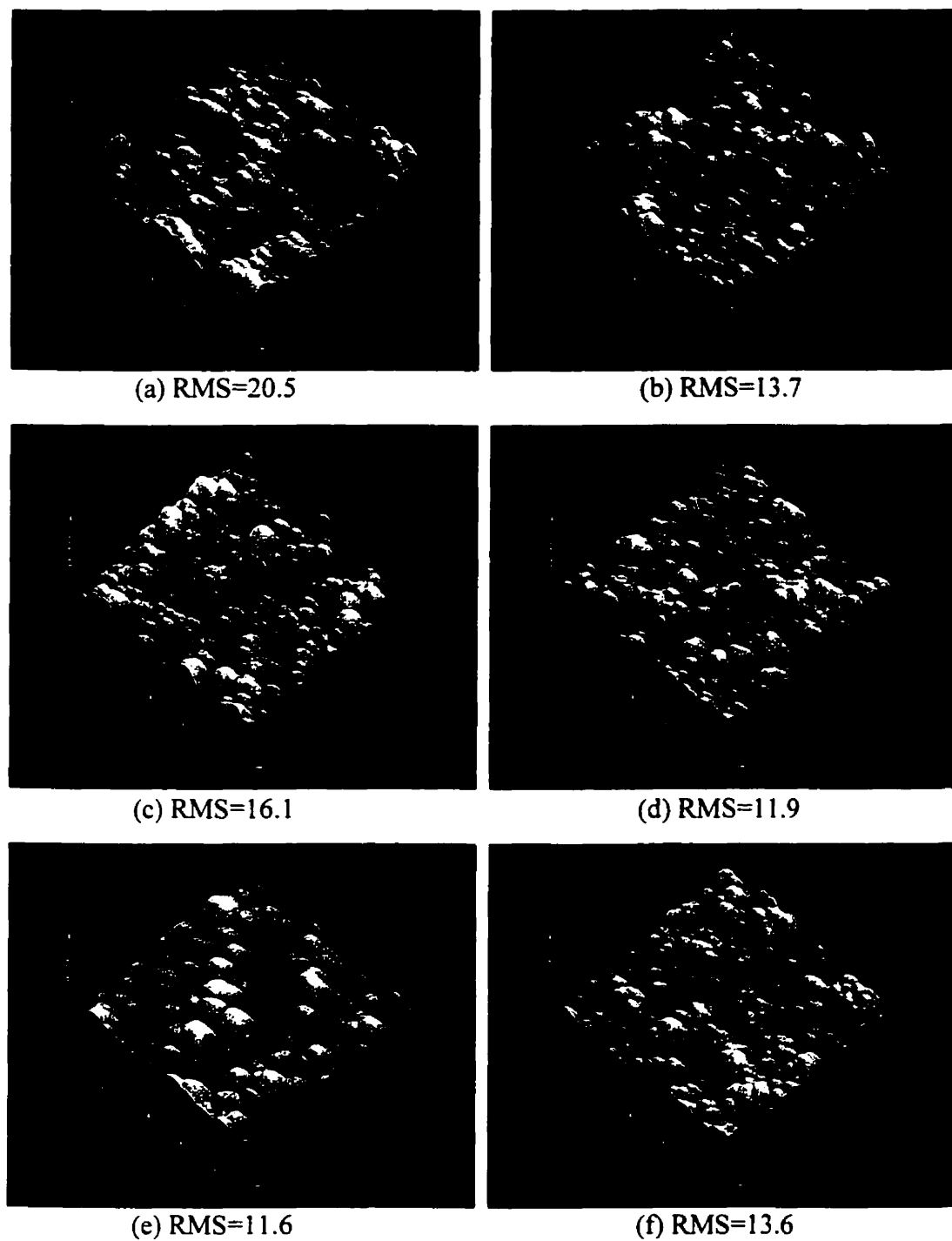


Figure 5.7. The morphology and roughness of oxide after 3 hours at 200°C on the (a) (100) face, (b) (110) face, (c) (123) face, (d) (314) face, (e) (111) face and (f) (311) face.

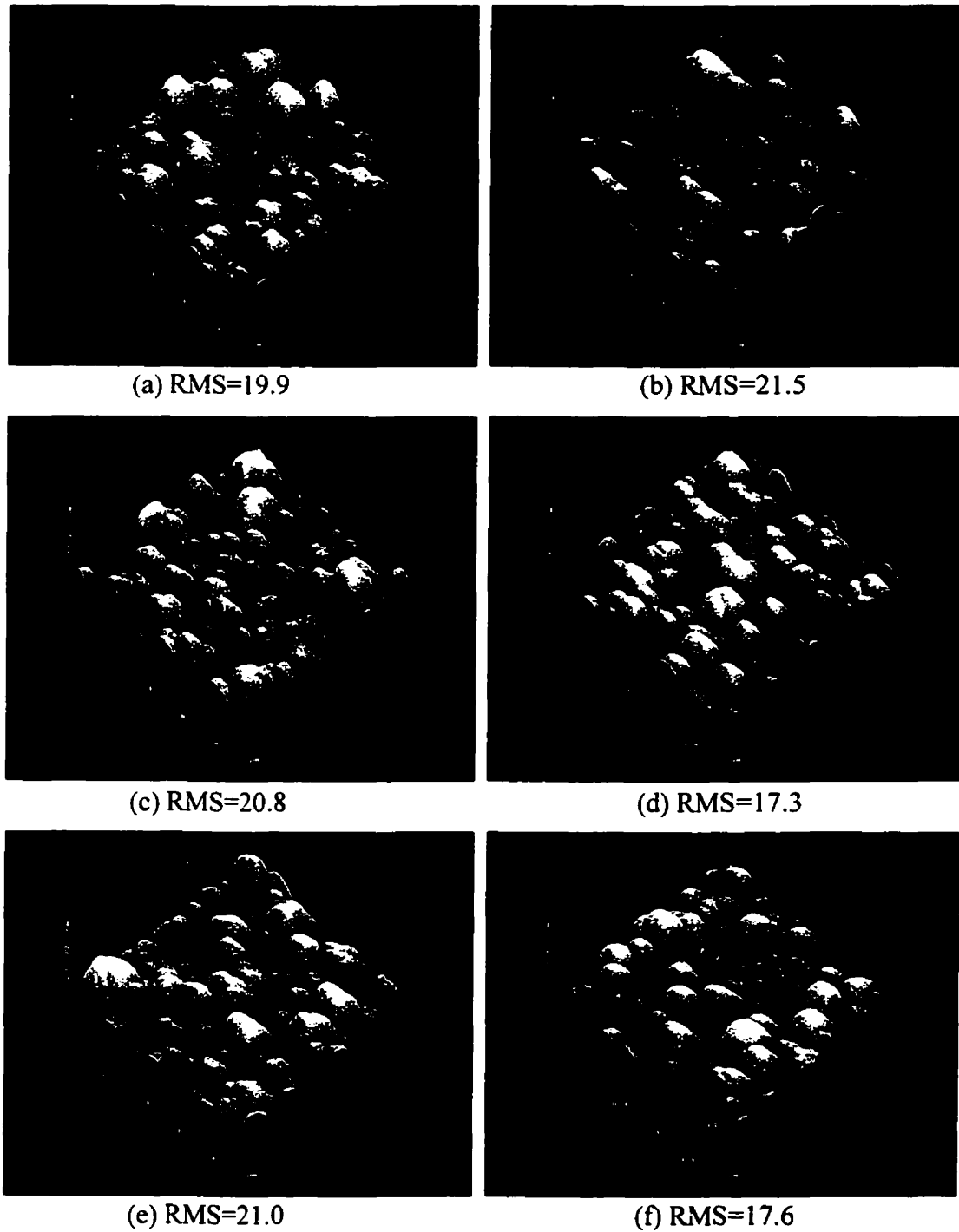
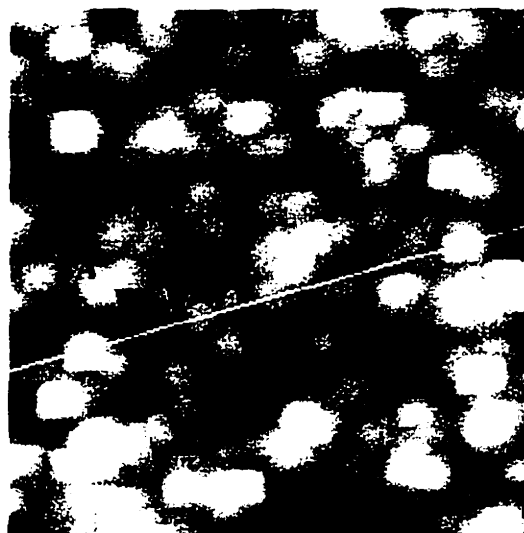
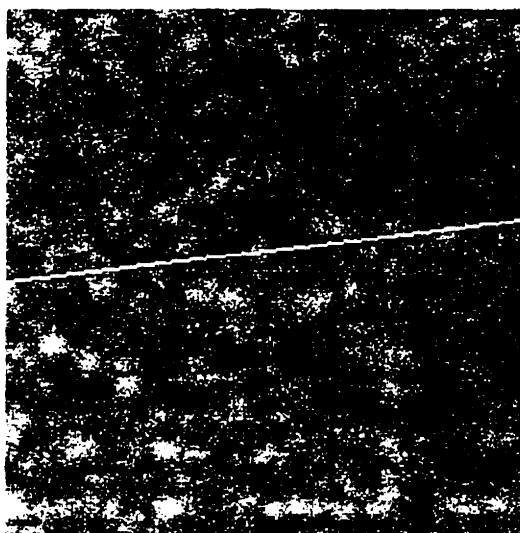
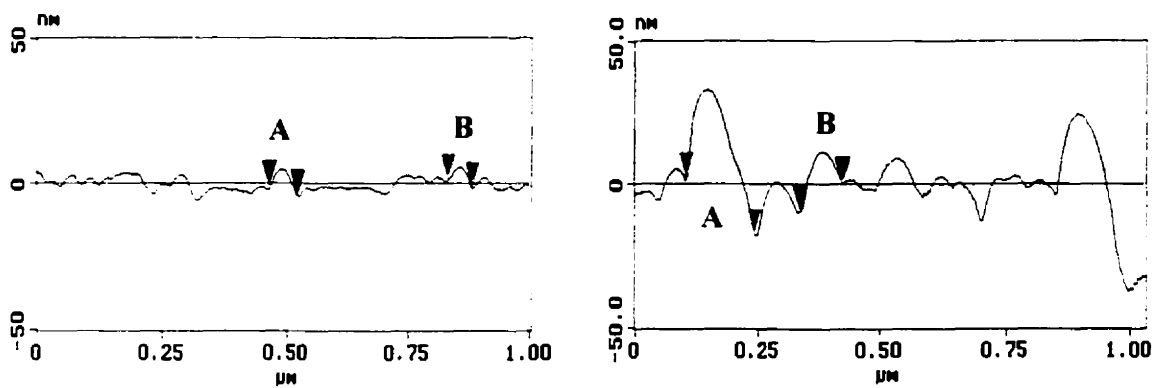


Figure 5.8. The morphology and roughness of oxide after 9 hours at 200°C on the (a) (100) face, (b) (110) face, (c) (123) face, (d) (314) face, (e) (111) face and (f) (311) face.



A	Horiz distance (L)	58.59 nm
	Vert distance	3.13 nm
B	Horiz distance	50.78 nm
	Vert distance	2.58 nm

(a) 1 minute

A	Horiz distance (L)	85.94 nm
	Vert distance	10.28 nm
B	Horiz distance	138.67 nm
	Vert distance	19.77 nm

(b) 30 minutes

Figure 5.9. The cross-sections of oxides on specimen C, which oxidized at 200°C for (a) 1 minute and (b) 30 minutes.

5.4. PREDICTION OF OXIDATION KINETICS FROM THE TEXTURE OF THE SPECIMEN

There have been many studies on details of copper oxidation kinetics such as oxidation rate laws, oxide film composition, alloying effects, effects of an oxidative atmosphere, and oxidation of single crystals [14, 60, 62, 111, 112, 122–125]. Although some of this work was carried out on the oxidation of single crystals, no study has been conducted to correlate the oxidation kinetics to the texture of polycrystalline substrates. Texture measurement is a non-destructive technique, while an oxidation test that could also reveal oxidation kinetics is a destructive one. At the same time, texture measurements can also give the other useful information about the physical, chemical and mechanical properties of the specimen, such as a strengthening [126], drawability [127, 128], fracture [129, 130] and magnetic properties [131, 132]. Therefore, there will be many advantages if one can predict copper oxidation from a texture measurement.

A quantitative model was proposed to predict oxidation kinetics of copper from texture data. An inverse pole figure was used to describe the texture and the amount of oxidation. It describes the orientation by specifying the poles of the sample coordinate system with respect to those of the crystal coordinate system in stereographic projection. The orientation is then given by the polar coordinates of three poles Φ_{RD} , β_{RD} ; Φ_{TD} , β_{TD} ; Φ_{VD} , β_{VD} . It can be written as a distribution function $R_{y_i}(h)$ as in Equation (5.1), which gives the frequency with which the various crystal direction h coincides with a specific sample direction y_i .

$$R_{y_i}(h) = \sum_{l=0}^{\infty} \sum_{\mu=1}^{M(l)} \frac{4\pi}{2l+1} \sum_{\nu=1}^{N(l)} C_l^{\mu\nu} \dot{k}_l^{\nu}(y_i) \dot{k}_l^{\mu}(h) \quad (5.1)$$

where the coefficients $C_l^{\mu\nu}$ are the coefficients of ODF and the $\dot{k}_l^{\nu}(y_i)$ and $\dot{k}_l^{\mu}(h)$ are symmetric spherical surface harmonics chosen to fulfill the sample and crystal symmetries, respectively.

As discussed in Chapter 5.1, the oxidation rate of copper is anisotropic. Therefore, the amount of oxidation of each orientation ($O(hkl)$), which represents the thickness of oxide in this model, can be drawn in an inverse pole figure space as a numeric value, a so-called 'oxidation weight'. From the experimental data as shown in Figure 5.2, the oxidation weights of $\{100\}$, $\{110\}$, $\{111\}$, $\{123\}$, $\{311\}$ and $\{314\}$ orientations were obtained. To describe the anisotropy of the oxidation behavior, the inverse pole figure space was then divided into 2.5° angular intervals and the oxidation weights of every corresponding crystallographic directions in the space were calculated by using Equation (5.2).

$$W(\Phi_{ND}, \beta_{ND}, hkl) = \frac{1}{(\text{Angular Distance between } O(\Phi_{ND}, \beta_{ND}) \text{ and } O(hkl))^2} \quad (5.2)$$

The oxidation weights drawn in an inverse pole figure space ($O(\Phi_{ND}, \beta_{ND})$) were defined as 'oxidation weight inverse pole figure', which can be described as Equation (5.3). An inverse pole figure for the normal direction (ND) of the specimens was used. The oxidation inverse pole figure was generated for all the time periods tested, and some of them are illustrated in Figure 5.10. One unit of the oxidation weight is a micrometer. As shown in Figure 5.10, the $\{100\}$ orientation oxidized more than the other orientations during the oxidation test.

$$O(\Phi_{ND}, \beta_{ND}) = \frac{\sum_{hkl} O(hkl) \cdot W(\Phi_{ND}, \beta_{ND}, hkl)}{\sum_{hkl} W(\Phi_{ND}, \beta_{ND}, hkl)} \quad (5.3)$$

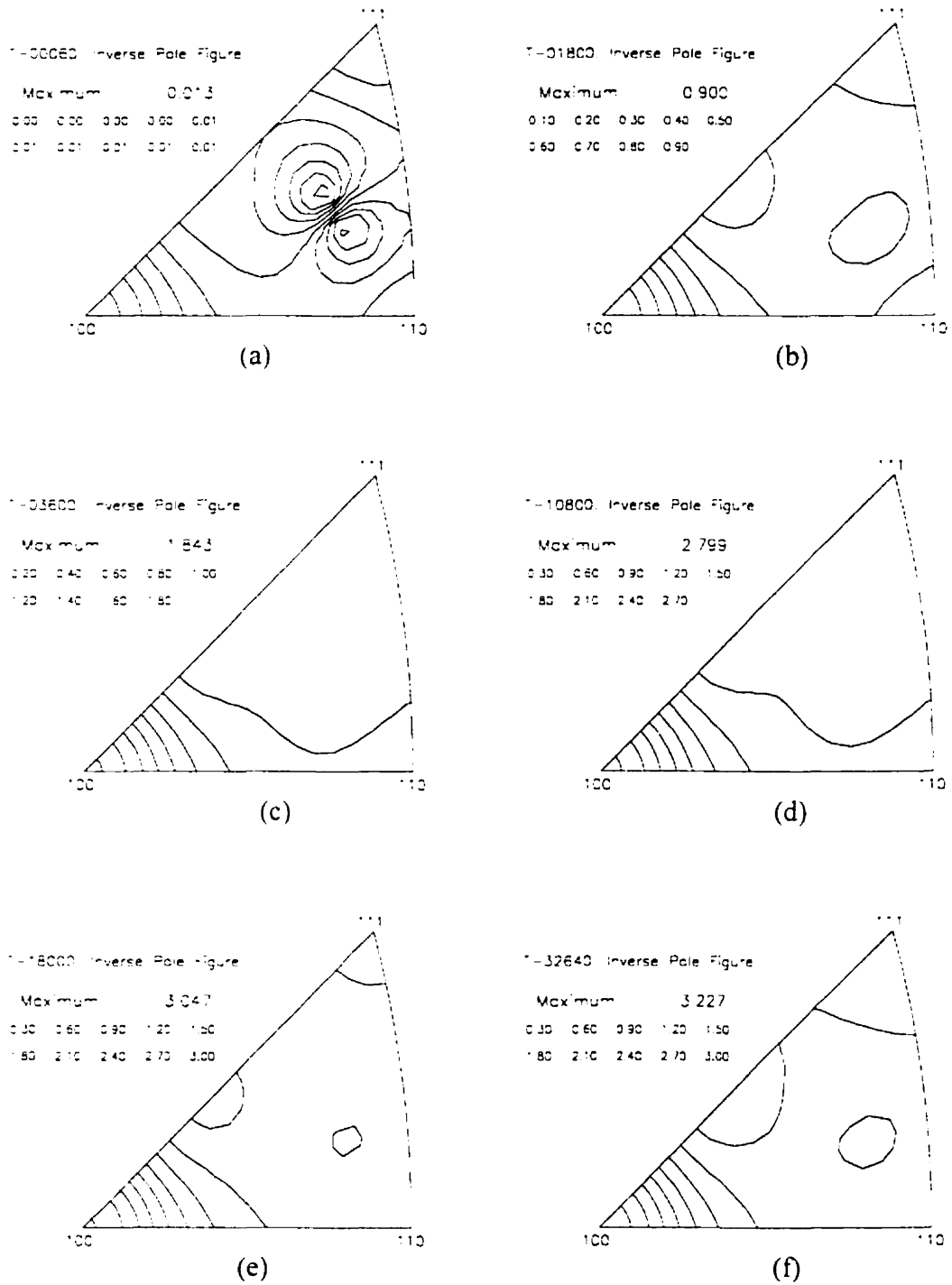


Figure 5.10. Oxidation inverse pole figures generated at various oxidation times: (a) 60 seconds, (b) 1,800 seconds, (c) 3,600 seconds, (d) 10,800 seconds, (e) 18,000 seconds, and (f) 32,640 seconds.

The amount of oxidation of polycrystalline specimens was calculated using the normal direction (ND) inverse pole figure of the examined polycrystalline specimens and the oxidation inverse pole figure that represents the weight of oxide at a given oxidation time. The amount of oxidation (\bar{O}) at any given time can be written as,

$$\bar{O}(t) = \frac{\int_0^{2\pi} \int_0^{\pi} R(\Phi_{ND}, \beta_{ND}) \cdot O(\Phi_{ND}, \beta_{ND}, t) \cdot \sin \Phi_{ND} d\Phi_{ND} d\beta_{ND}}{\int_0^{2\pi} \int_0^{\pi} R(\Phi_{ND}, \beta_{ND}) \cdot \sin \Phi_{ND} d\Phi_{ND} d\beta_{ND}} \quad (5.4)$$

where $R(\Phi_{ND}, \beta_{ND})$ is the inverse pole figure of direction normal to the surface of oxidized specimen and $O(\Phi_{ND}, \beta_{ND}, t)$ is the oxidation weight at a given time, which is represented in the inverse pole figure.

To compare the model with experimental results, specimens having the same six orientations as the single crystals were assumed, and their inverse pole figures were generated (Figure 5.11). The oxidation kinetics obtained from these inverse pole figures are illustrated in Figure 5.12. The evaluated values were lower than the experimental values obtained from the oxidation tests of the single crystals (Fig. 5.2). Figure 5.12 demonstrates that the oxidation of the specimen having a strong {100} texture had progressed much more than that of the other specimens. Among other specimens, the specimen (110) seemed to have exhibited a relatively higher oxidation all through the oxidation test. There were not many differences in oxidation among the specimens (314), (123) and (111). It was observed that the oxidation of the specimen (311), which actually had the lowest rate in the experimental tests, became higher than those of the specimens (314), (123) and (111). This may be from the calculation of the oxidation weight of each orientation. The location of the {311} orientation, which has the lowest oxidation weight, is close to the location of the {111} orientation, which has the highest oxidation rate. When the oxidation weights were calculated, their values near the {311} orientation were influenced by the high weight value of the {100} orientation and therefore became higher than expected. This error should diminish if

more experimental data points are used to determine the oxidation weight inverse pole figure.

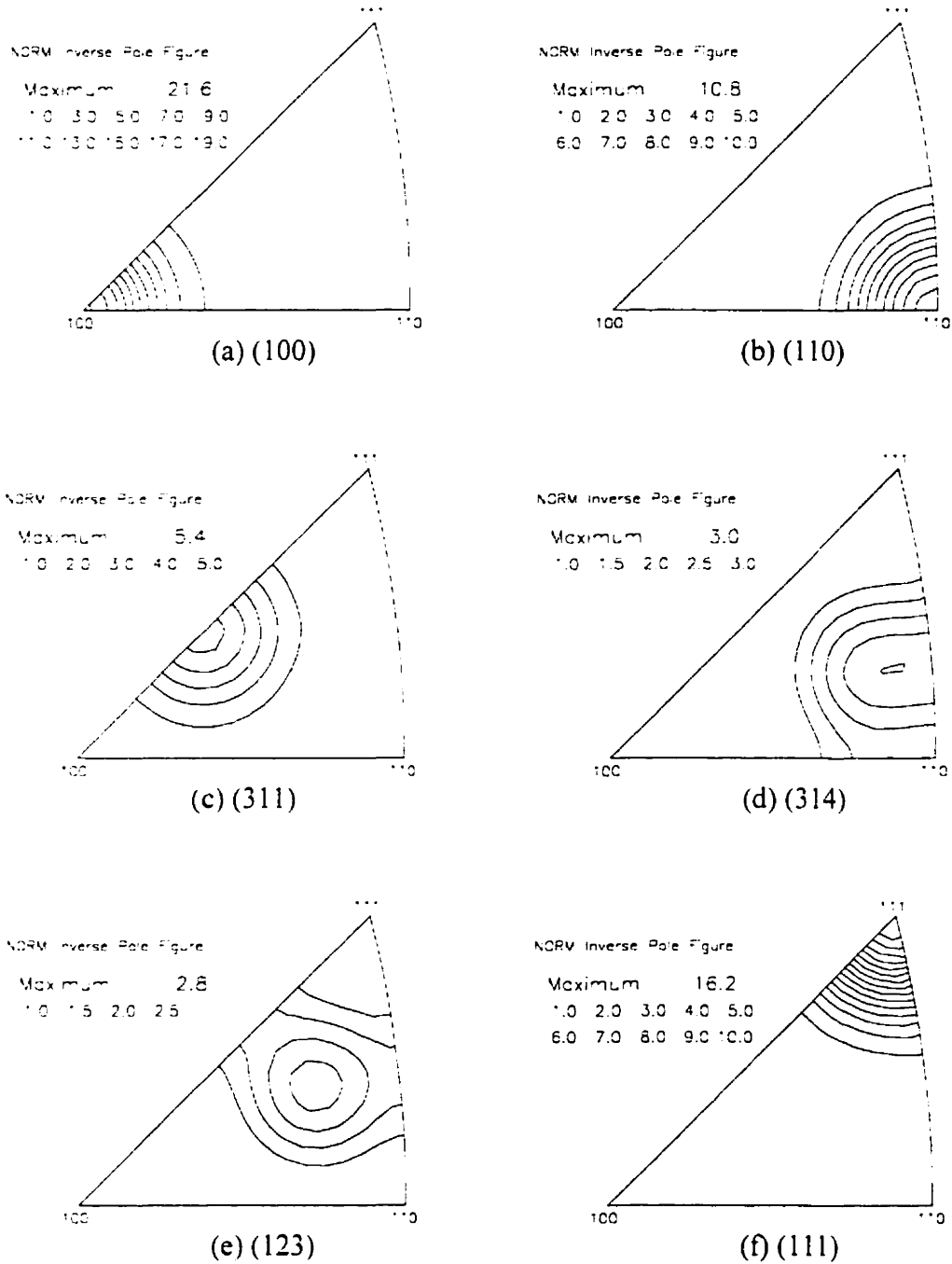


Figure 5.11. Inverse pole figures generated for the specimens assumed to have different orientations.

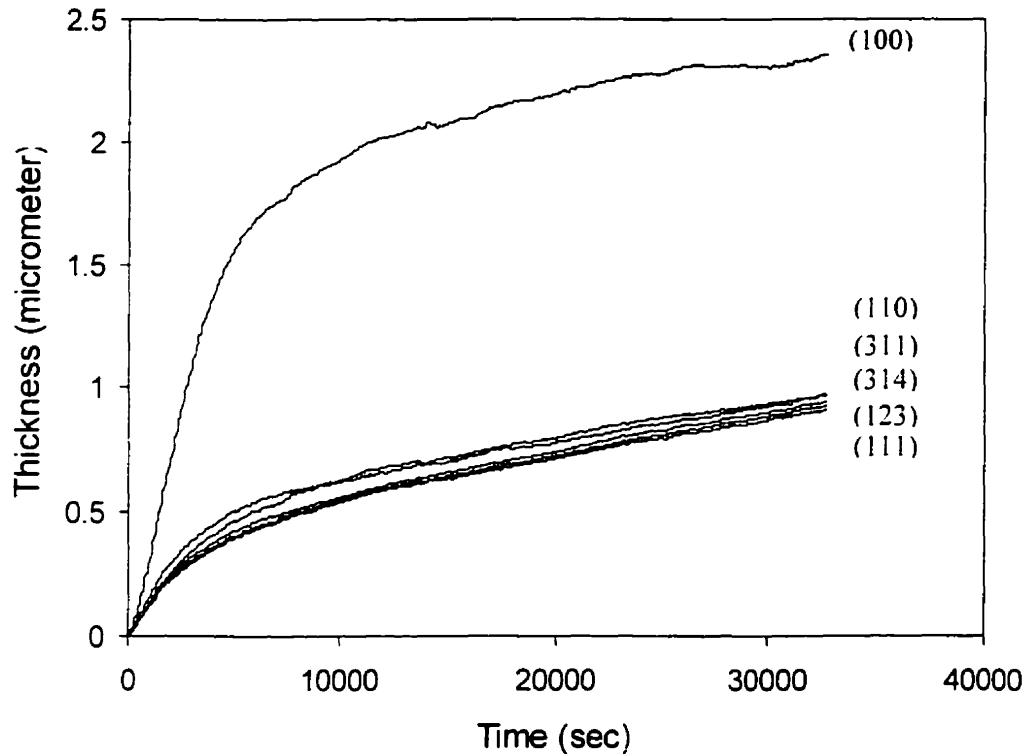


Figure 5.12. Oxidation kinetics simulated for the specimens having different orientations.

The proposed model can be used to predict the oxidation kinetics of any textured polycrystalline copper specimen. The oxidation kinetics at 200°C of polycrystalline coppers are shown in Figure 5.13. Copper specimens of 99.999% purity were used. Specimen selection is very important in the study of oxidation since the oxidation kinetics of copper varies with impurities and alloying elements [121–124]. It is known that certain added elements in copper can act as dopants and change the point defect concentration, which governs ionic mobility. Specimens having similar grain sizes were selected to avoid the possible influence of grain size on oxidation kinetics. The average diameter of grains of the investigated specimens was approximately 10–12 μm . Texture measurements carried out for the specimens and three specimens (PA, PB and

PC) having different textures were finally selected for this study. As shown in Fig. 5.13, the specimen PA oxidized faster than the specimens PB and PC, while the specimen PC oxidized the slowest. After 9 hours of oxidation, the difference in thickness between specimen PA and specimen PC was about $0.4 \mu\text{m}$.

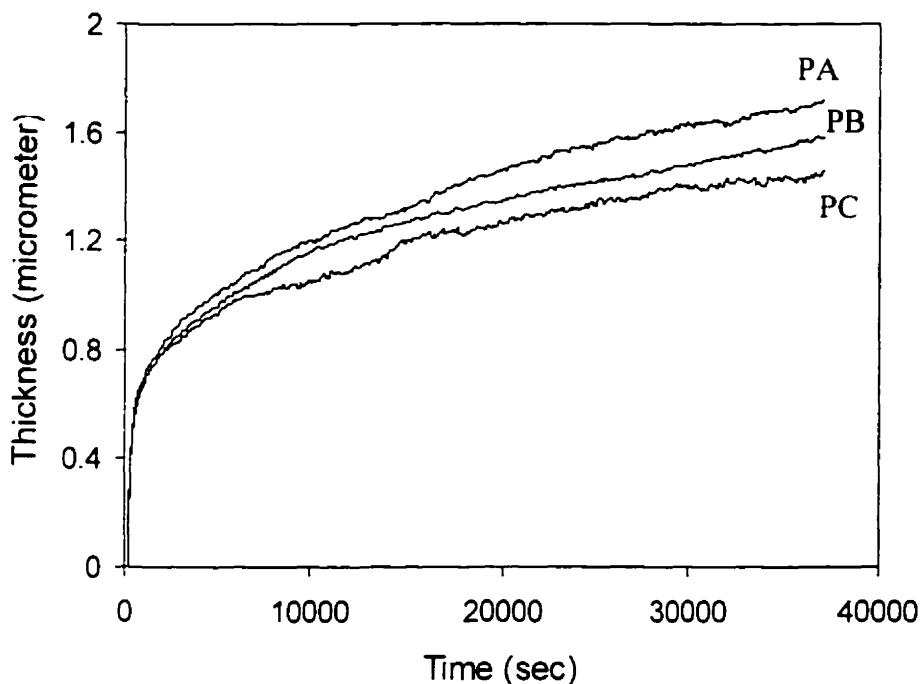


Figure 5.13. Oxidation kinetics of the copper polycrystalline specimens at 200°C .

The texture of each specimen is shown in an ND inverse pole figure (Figure 5.14). The specimen PA had a strong $\{100\}$ texture with a maximum of 5.9 and the specimen PC had a strong $\{102\}$ texture with a maximum of 4.7. No predominant texture was found in the specimen PB; however, the $\{110\}$ texture was relatively stronger than the other texture components. To re-iterate what was shown in Fig. 5.2, the specimen having (100) face parallel to its surface had the highest oxidation rate. Considering this fact, the strong $\{100\}$ texture in specimen PA was responsible for the fast oxide growth on it.

An inverse pole figure of a randomly oriented specimen was generated as well and is shown in Fig. 5.14.

The oxidation kinetics evaluated for the specimen PA, PB, PC and the randomly oriented specimen are shown in Figure 5.15. Comparing this figure to Fig. 5.13, the evaluated values seemed to be lower than the experimental ones, similarly observed in the results obtained for single crystals. In comparison, the amount of oxidized specimen PA, which had a strong {100} texture, was relatively higher than that of the other specimens. In the evaluated oxidation kinetics, the difference in oxidized amounts between specimens PB and PC became smaller than the difference observed in the experiments. The order of the oxidation kinetics curves in the measured and evaluated values was the same.

The model developed for this study is the first attempt to predict the kinetics of copper oxidation from its texture. It was applied only to the copper oxidation at a relatively low temperature of 200°C. Reasonable agreement was obtained when comparing the model predictions and the experimental results obtained from the oxidation of polycrystalline copper specimens. However, further improvement of the model is possible if more data points from single crystal experiments can be obtained. This model might be applied to other oxidation conditions and to the oxidation of other materials.

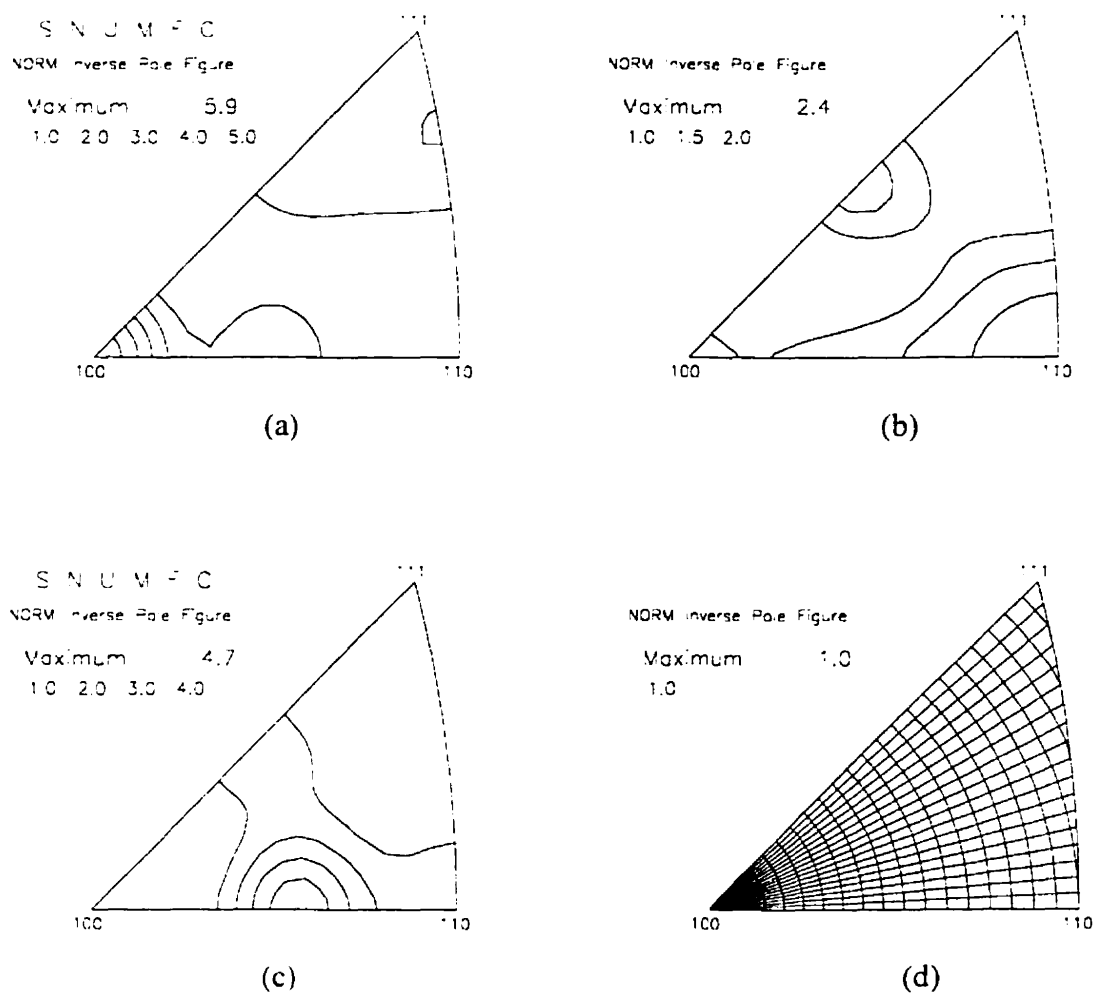


Figure 5.14. Texture of the polycrystalline specimens: (a) PA, (b) PB, (c) PC and (d) randomly oriented specimen.

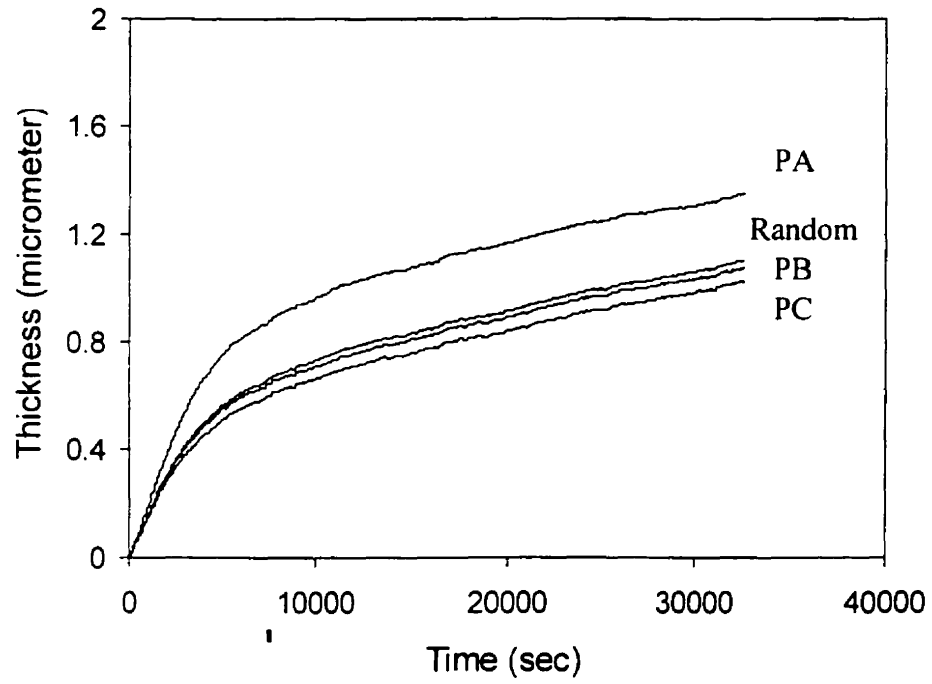


Figure 5.15. Oxidation kinetics simulated for the specimens PA, PB, PC and the randomly oriented specimen.

5.5. SUMMARY

To understand the oxidation kinetics of copper interconnects and the influence of substrate texture on oxide growth, copper single crystals having different orientations were oxidized at 200°C for 9 hours. The oxidation atmosphere was provided by flowing air. Only the Cu_2O phase was observed during oxidation.

The crystal faces (100), (110), (123), (314), (111) and (311) represent, in that order, decreasing rates of oxidation. The oxidation of the (100) single crystal was much higher than that of the others. During the initial stage of oxidation, the oxide on the (100) face of the copper specimen had a large number of fine oxide grains having a {111} orientation. These grains seemed to be responsible for the high oxidation rate of the specimen having the (100) orientation. A high number of grain boundaries and defects accelerate copper ion diffusion. It is therefore apparent that the {100} texture in copper should be avoided to reduce copper oxidation.

A quantitative model was proposed to predict the oxidation kinetics of copper from the texture of the specimens. The experimental data obtained from the single crystals were used for the model. Reasonable agreement was obtained between the theoretical and the experimental results obtained from the oxidation kinetics of polycrystalline copper specimens. However, further improvement of the model will require a larger number of data points from single crystals experiments. The model might be applied to other oxidation conditions and to the oxidation of other materials.

Chapter 6

Summary and Conclusions

The main objective of this study was (1) to expand the current understanding of the influence of texture on electromigration and stress-induced failures in aluminum interconnects, and (2) to understand the influence of substrate texture on the oxidation kinetics of copper interconnects and to suggest a method to reduce their oxidation.

To understand the influence of texture on the reliability of aluminum interconnects, specimens having different textures were prepared and electromigration tests were carried out on these specimens. The grain boundary character distribution and percentage of coincidence site lattice (CSL) boundaries were quantified using orientation imaging microscopy. The influence of texture and grain boundary character distribution on film reliability was discussed. The microstructure of the films was analyzed and the correlation between the texture of the films and their internal stress was investigated. Finally, a model of Monte-Carlo simulation of texture formation during the deposition of aluminum film was proposed to suggest the optimum deposition conditions for texture development.

Copper interconnect lines are susceptible to oxidation. The objective of this research was to understand the influence of substrate texture on the oxidation kinetics of copper and to suggest a method to reduce copper oxidation. This was accomplished by

oxidizing copper single crystals having different orientations and analyzing results obtained from oxidation tests. The influence of substrate orientation on the development of oxide texture and morphology was also studied. A quantitative model was proposed to predict oxidation kinetics of copper from the texture of the specimens.

6.1. CONCLUSIONS

The following conclusions are drawn from the work presented in this thesis.

6.1.1. The Influence of Texture on the Reliability of Aluminum Thin Films

1. Results obtained from the texture measurements and the electromigration tests showed that a strong $\{111\}$ texture in aluminum films improves their median time-to-failure.
2. The lifetime of the specimens increased as the number of low angle grain and coincidence site lattice (CSL) boundaries increased. High angle and non-CSL boundaries were observed in the failure areas. Considering the fact that the number of low angle grain boundaries and CSL boundaries increased as the strength of the $\{111\}$ texture increased, a strong $\{111\}$ texture in aluminum interconnects is desirable in order to improve their reliability.
3. While the investigated specimens had grains of comparable size, it was found that grains of similar orientations were clustered in the specimens having a stronger $\{111\}$ texture. This phenomenon contributed to the longer median time-to-failure of the interconnects by reducing the frequency of high angle grain boundaries.
4. This study could not establish a straightforward relationship between the texture of films and their stress-induced failure. Nevertheless, the experimental data obtained showed that the residual stress of films decreased as the intensity of the $\{111\}$ texture increased.

5. A model of a Monte-Carlo simulation of texture formation during the deposition of aluminum film was proposed to suggest the optimum conditions for a growth of a strong {111} texture component. A low deposition rate and a high mobility of atoms on the surface, corresponding to the presence of high substrate temperatures, were found to be the best operating parameters to acquire the desired {111} texture.

6.1.2. The Influence of Texture on the Oxidation Kinetics of Copper

1. Only the Cu_2O phase was formed during oxidation tests of the copper single crystals at 200°C in air. The crystal faces could be listed in decreasing order of oxidation rates as (100), (110), (123), (314), (111) and (311). The oxidation of the (100) single crystal was especially faster than that of the others.
2. In the initial stages of oxidation, the oxide on the (100) face of the copper specimen had a large number of fine oxide grains. They seemed to be responsible for the fast oxidation of the specimen by introducing more grain boundaries and defects, which accelerates copper ion diffusion.
3. Considering the results obtained from the oxidation tests and the analysis of oxide morphology, it is recommended that the {100} texture in copper interconnects be avoided in order to reduce copper oxidation.
4. A quantitative model was proposed to predict the oxidation kinetics of copper from the texture of the specimens. Reasonable agreement was obtained when comparing model predictions and experimental results obtained from the oxidation of polycrystalline copper specimens.

6.2. STATEMENT OF ORIGINALITY

The following aspects of the present work constitute original contributions to the field.

1. The correlation of the grain boundary character distribution and coincidence site lattice (CSL) boundaries with the texture and reliability of aluminum films is original; it explains why a strong $\{111\}$ texture in aluminum interconnects is desirable in order to improve their reliability.
2. The effect of orientation clustering, which is the clustering of grains having similar orientations, on the reliability of aluminum film was considered for the first time; it can be regarded as a possible factor influencing properties of other types films.
3. The model of Monte-Carlo simulation of texture formation during the deposition of aluminum films was proposed; it suggests the optimum deposition parameters to acquire a certain texture component during film deposition and it can be easily adapted to the deposition of other materials.
4. The analysis of the oxide morphology, which was obtained during the initial stages of oxidation, explains the theory suggested by Lawless and Gwathmey [112].
5. A quantitative model was proposed to predict the oxidation kinetics of a polycrystalline copper from its texture. With further improvement, this model has the potential to be applied to other oxidation conditions and to the oxidation of other materials.

6.3. FUTURE WORK

The following aspects are recommended for future work.

1. The influence of texture on the reliability of aluminum thin films was examined in this study. It was reported that the properties of thin films could be improved by adding alloying elements. Therefore, it is worthy to carry similar studies on aluminum alloy films.
2. No straightforward relationship between the texture of films and their stress-induced reliability concerns has been suggested so far. More intensive studies are necessary in this field.
3. Applications of the model of Monte-Carlo simulation, which proposes optimum conditions for the development of a certain texture component during film deposition, are wide-open and should be extended to other materials.
4. In this study, the results obtained from the oxidation tests of the bulk specimens were analyzed. The oxidation kinetics of bulk copper may differ from that of thin films. Oxidation tests for single crystal films are suggested to be carried out.
5. For better quantitative texture measurements of thin oxide layer on single crystals, a texture goniometer equipped with a monochromator is recommended.
6. The proposed model predicting the oxidation kinetics of copper from its texture was applied to the bulk specimens. Oxidation tests for copper films should be carried out and the results obtained from the bulk and film specimens should be compared. Further improvement of this model is necessary for its application to other oxidation conditions and to the oxidation of other materials.

7. A study on the influence of texture on the oxidation kinetics at higher temperatures would be an interesting investigation since at those temperatures, CuO phase exists in addition to the Cu₂O phase.

REFERENCES

- [1] G. E. Moor, *Electron Aust.*, 1980, vol. 42, p.14.
- [2] W. Myers, *IEEE Micro.*, 1991, vol. 11, p. 10.
- [3] C. Y. Chang and S. M. Sze, *ULSI Technology*, McGraw-Hill, New York, 1996.
- [4] M. J. Attardo and R. Rosenberg, *J. Appl. Phys.*, 1970, vol. 41, p. 2381.
- [5] E. Nagasawa, H. Okabayashi, T. Nozaki and K. Nikawa, *Proceedings of The 17th Reliability Physics Symposium (IEEE, New York)*, 1979, p. 64.
- [6] H. Taniguchi, T. Ushiro, Y. Okamoto, Y. Akagi and M. Koba, *Proceedings of Mat. Res. Soc. Symp.*, 1993, vol. 280, p. 523.
- [7] P. Li, A. S. Yapsir, K. Rajan and T. M. Lu, *Appl. Phys. Lett.*, 1989, vol. 54, p. 2443.
- [8] D. B. Knorr and K. P. Rodbell, *Proceedings of The Mat. Res. Soc. Symp.*, 1992, vol. 265, p. 113.
- [9] C. Li, R. D. Black and W. R. LaFontaine, *Mat. Res. Soc. Symp. Proc.*, 1989, vol. 30, p. 225.
- [10] W. D. Nix and E. Arzt, *Metall. Trans.A*, 1992, vol. 23A, p. 2007.
- [11] D. B. Knorr, *Mat. Res. Soc. Symp. Proc.*, 1993, vol. 309, p. 75.
- [12] P. Gwynne, *IBM Research*, 1997, No. 4, p. 17.
- [13] S. P. Murarka, R. J. Gutmann, A. E. Kaloyeros and W. A. Lanford, *Thin Solid Films*, 1993, vol. 236, p. 257.
- [14] A. Rönquist and H. Fischmeister, *J. Inst. Met.*, 1961, vol. 89, p. 65.
- [15] J. Li, J. W. Mayer and E. G. Colgan, *J. Appl. Phys.*, 1991, vol. 75, n. 5, p. 2820.
- [16] P. J. Ding, W. A. Lanford, S. Hymes and S. P. Murarka, *Appl. Phys. Lett.*, 1994, vol. 64, n. 21, p. 2897.
- [17] M. Hatherley and W. B. Hutchinson, *An introduction to texture in metals*, Chameleon Press, London, 1979.
- [18] H. J. Bunge, *Z. Metallkunde*, 1965, vol. 56, p.872.
- [19] A. S. Viglin, *Fizika Tverdogo Tela*, 1960, vol. 2, p. 2463.
- [20] J. Bardeen, and W. H. Brattain, *Phys. Rev.*, 1947, vol. 74, p. 230.
- [21] G. E. Moore, *IEEE Spectrum*, 1975, vol. 16, n. 4, p. 30.

-
- [22] W. Schockley, *Bell Syst. Tech. J.*, 1949, vol. 28, p 435.
- [23] *1994 Electronic Market Data Book*, Electronic Industries Association, Washington, D.C., 1994.
- [24] *1994 Annual Report of Semiconductor Industry*, Industrial Technology Research Institute, Hsinchu, Taiwan, ROC, 1994.
- [25] N. G. Einspruich, (ed.), *VLSI Electronics, Microstructure Science*, vol. 1, Academic Press, New York, 1981.
- [26] T. E. Price, *Introduction to VLSI Technology*, Prentice Hall International, Hertfordshire, UK, 1994.
- [27] P. Shepherd, *Integrated Circuit Design, Fabrication and Test*, Macmillan Press, London, UK, 1996.
- [28] N. Braithwaite and G. Weaver, *Electronic Materials*, Butterworths, London, UK, 1990.
- [29] S. P. Murarka, *Metallization*, Butterworth-Heinemann, Stoneham, MA, 1993.
- [30] S. H. Kang, J. W. Morris, Jr. and A. S. Oates, *JOM*, March 1999, p. 16.
- [31] J. L. Vossen and W. Kern, eds., *Thin Film Process*, Academic, New York, 1978, p. 12.
- [32] J. L. Vossen and W. Kern, eds., *Thin Film Process*, Academic, New York, 1978, p. 131.
- [33] B. Gorowitz, T. B. Gorczyca and R. J. Saia, *Sol. State Technol.*, June 1985, p. 197.
- [34] W. C. Lai, K. P. Cheung, D. P. Favreau, C. J. Case and R. Liu, *Proceedings of the 8th International IEEE VLSI Multilevel Interconnection Conference*, 1991, p. 89.
- [35] B. Luther, J. F. White, C. Uzoh, T. Cacouris, J. Hummel, et al., *Proceedings of the 10th International IEEE VLSI Multilevel Interconnection Conference*, 1993, p. 15.
- [36] K. C. Saraswat, D. L. Brors, J. A. Fair, K. A. Monnig and R. Beyers, *IEEE Trans. Electron Dev.*, ED-30, 1983, p. 1497.
- [37] A. Sherman, *J. Electrochem. Soc.*, 1990, vol. 137, p. 1892.
- [38] M. L. Green and R. A. Levy, *J. Electrochem. Soc.*, 1985, vol. 132, p. 1243.
- [39] M. Ohring, *Reliability and Failure of Electronic Materials and Devices*, Academic Press, San Diego, 1998.

- [40] E. R. Hnatek, *Integrated Circuit Quality and Reliability*, Marcel Dekker, Inc. New York, 1995.
- [41] J. R. Black, *IEEE Trans. Electron Dev.*, 1969, ED-16, p. 338.
- [42] J. R. Black, *Reliability Physics, 12th annual Proceedings*, 1974, p. 142.
- [43] J. Bass, *Philos. Mag.*, 1967, vol. 15, p. 717.
- [44] J. Klema, R. Pyle and E. Domangue, *Reliability Physics, 22th annual Proceedings*, 1984, p. 1.
- [45] J. Curry, G. Fitzgibbon, Y. Guan, R. Mullo G. Nelson and A. Thoma, *Reliability Physics, 22th annual Proceedings*, 1984, p. 6.
- [46] J. T. Yue, W. P. Funsten and R. V. Taylor, *Reliability Physics, 23th annual Proceedings*, 1985, p. 126.
- [47] J. W. McPherson and C. F. Dunn, *J. Vac. Sci. Technol.*, 1987, B5, p. 1321.
- [48] S. Mayumi, T. Umemoto, M. Shishino, H. Nanatsue, S. Ueda and M. Inoue, *Reliability Physics, 25th annual Proceedings*, 1987, p. 15.
- [49] A. K. Sinha and T. T. Sheng, *Thin Solid Films*, 1978, vol. 48, p. 117.
- [50] A. I. Sauter and W. D. Nix, *IEEE Trans. Components, Hybrids and Manufacturing Technology*, 1992, vol. 15, p. 594.
- [51] B. D. Cullity, *Elements of X-ray Diffraction, 2nd ed.*, 1978, Addison-Wesley, MA.
- [52] P. Blandford, *Ph. D. Thesis*, 1997, McGill Univ., Canada.
- [53] M. N. Alam, M. Blackman and D. W. Pashley, *Proc. R. Soc.*, 1954, vol. 221A, p. 224.
- [54] J. A. Venables and R. B. Jaya, *Philos. Mag.*, 1977, vol. 35, p. 1317.
- [55] C. J. Harland, P. Akhter and J. A. Venables, *J. Phys. E*, 1981, vol. 14, p. 175.
- [56] A. J. Wilkinson and D. J. Dingley, *Acta Metall. Mater.*, 1991, vol. 39, p. 3047.
- [57] D. J. Dingley and V. Randle, *J. Mater. Sci.*, 1992, vol. 27, p. 4545.
- [58] G. Binnig and C. F. Quate, *Phys. Rev. Lett.*, 1986, vol. 56, p. 930.
- [59] Martin et al., *J. Appl. Phys.*, 1987, vol. 61, p. 10.
- [60] R. F. Tylecote, *J. Inst. Metals*, 1952-53, vol. 81, p. 681.
- [61] J. P. Baul, D. W. Bridges and W. M. Fassell, *J. Electrochem. Soc.*, 1956, vol. 103, p. 273.

- [62] T. N. Rhodin, *J. Amer. Chem. Soc.*, 1951, vol. 73, p. 3143.
- [63] T. Watanabe, *Mater. Sci. Forum*, 1989, vol. 46, p. 25.
- [64] G. Palumbo, P. J. King, K. T. Aust, U. Erb and P. C. Lichtenberger, *Scripta Metall.*, 1991, vol. 25, p. 1775.
- [65] J. Harase and R. Shimizu, *Acta Met.*, 1992, vol. 40, p. 1101.
- [66] L. K. Fionova, O. V. Kononenko and V. N. Matveev, *Thin Solid Films*, 1993, vol. 227, p. 54.
- [67] J. Cho and C. V. Thompson, *J. Appl. Phys.*, 1991, vol. 69, p.2117.
- [68] M. Genut, Z. Li, C. L. Bauer, S. Mahajun, P. F. Tang and A. G. Milnes, *Appl. Phys. Lett.*, 1991, vol. 58, p. 2354.
- [69] H. Dittich, et al., *Mat. Sci. Forum*, 1993, vol. 133-136, p. 169.
- [70] J. Pospeich and J. Jura, *Z. Metallkunde*, 1974, vol. 65, p. 324.
- [71] A. Morawiec, J. A. Szpunar and D. C. Hinz, *Acta Metall.*, 1993, vol. 41, p. 2825.
- [72] D. G. Brandon, *Acta Metall.*, 1966, vol. 14, p. 1479.
- [73] D. Walton, *Phil. Mag.*, 1962, vol. 14, p. 1671.
- [74] S. Vaidya and A. K. Sinha, *Thin Solid Films*, 1981, vol. 75, p. 253.
- [75] J. M. Burgers, *Proc. Phys. Soc.*, 1940, vol. 52, p. 23.
- [76] W. T. Read and W. Shockley, *Phys. Rev.*, 1950, vol. 78, p. 275.
- [77] D. Turnbull and R. E. Hoffman, *Acta Met.*, 1954, vol. 2, p. 419.
- [78] J. K. Mackenzie, *Biometrika*, 1958, vol. 45, p. 229.
- [79] N. A. Gjostein, *Diffusion*, ASM, Metals Park, OH, 1973, p.241.
- [80] R. E. Hoffman, *Acta Met.*, 1956, vol. 4, p. 97.
- [81] W. Bollmann, *Crystal Defects and Crystalline Interface*, Springer-Verlag, New York, NY, 1970.
- [82] S. Ranganathan, *Acta Crystallogr.*, 1966, vo.: 21, p. 197.
- [83] B. A. Faridi and A. G. Crocker, *Phil. Mag.*, 1980, vol. 41A, p. 137.
- [84] A. P. Sutton and V. Vitek, *Phil. Trans. R. Soc.*, 1983, vol. A309, p. 1.
- [85] I. Herbeuval, M. Biscondi and C. Goux, *Mem. Sci. Rev. Met.*, 1973, vol. 70, p.39.
- [86] N. L. Peterson, *Int. Met. Rev.*, 1983, vol. 28, p. 64.
- [87] D. H. Warrington and M. Boon, *Acta Met.*, 1975, vol. 23, p. 599.

- [88] A. Garbacz and M. W. Grabski, *Acta Met.*, 1993, vol. 41 p.469.
- [89] A. Garbacz and M. W. Grabski, *Acta Met.*, 1993, vol. 41 p.475.
- [90] T. Watanabe K. I. Arai, K. Yoshimi and H. Oikawa, *Phil. Mag. Lett.*, 1989, vol. 59, p. 47.
- [91] S. Vaidya, T. T. Sheng and A. K. Sinha, *Appl. Phys. Lett.*, 1980, vol. 36, p. 464.
- [92] H. T. Jeong, J. A. Szpunar, K. T. Lee and D. P. Field, *Proceedings of 12th Int. Conf. Tex. Mat. (ICOTOM)*, J. A. Szpunar eds., 1999, vol. 2, p.1369.
- [93] A. T. English and E. Kinsbron, *J. Appl. Phys.*, 1983, vol. 54, p. 268.
- [94] Y. H. Park, P. Rossele, E. Majewski and J. F. Smith, *J. Vac. Sci. Technol. A*, 1985, vol. 3, p. 2308.
- [95] R. E. Hummel and I. Yamada, *Appl. Phys. Lett.*, 1988, vol. 53, p. 1765.
- [96] S. N. Mei and T. M. Lu, *J. Vac. Sci. Technol. A*, 1988, vol. 6, p. 9.
- [97] P. A. Flinn, *Mat. Res. Soc. Symp. Proc.*, 1989, vol. 130, p. 41.
- [98] J. E. Sanchez, Jr., and E. Arzt, *Scripta Metallurgica*, 1992, vol. 27, p. 285.
- [99] R. A. Schwarzer and D. Gerth, *J. Elect. Mater.*, 1993, vol. 22, p. 607.
- [100] N. Kristensen, F. Ericson and J. Schweitz, *J. Appl. Phys.*, 1991, vol. 69, p. 2097.
- [101] H. Kaneko, M. Hasunuma, A. Sawabe, T. Kawanoue, Y. Kohanawa, S. Komatsu and M. Miyauchi, *Proceedings of the 28th Reliability Physics Symposium (IEEE, New York)*, 1990, p. 194.
- [102] S. Ogawa and M. Inoue, *Stress-Induced Phenomena in Metallization*, C. Y. Li, P. Totta and P. Ho, eds., *Am. Insti. Phys. Conf. Proc.*, 1992, vol. 263, p. 21.
- [103] S. Kordic, R. A. M. Wolters and K. Z. Troost, *J. Appl. Phys.*, 1993, vol. 74, p. 5391.
- [104] K. Reichelt, *Vacuum*, 1988, vol. 38, p. 1083.
- [105] P. Stinger, *Semiconductor International*, June 1998, p. 91.
- [106] P. Gwynne, *IBM Research*, 1997, no. 4, p. 17.
- [107] D. Edelstein, et al., *IEEE Intl. Electron Devices Meeting Digest*, 1997, p. 773.
- [108] C. K. Hu and J. M. E. Harper, *Mater. Chem. Phys.*, 1998, vol. 52, p. 5.
- [109] P. C. Andricacos, et al., *IBM J. Res. Develop.*, 1998, vol. 42, p. 567.
- [110] R. F. Tylecote, *J. Inst. Met.*, 1950-51, vol. 78, p. 327.

- [111] F. W. Young, J. V. Cathcart and A. T. Gwathmey, *Acta Met.*, 1956, vol. 4, p. 145.
- [112] K. R. Lawless and A. T. Gwathmey, *Acta Met.*, 1956, vol. 4, p. 153.
- [113] B. Rustman and F. Mehl, *Trans. Amer. Inst. Min. Met. Eng.*, 1941, vol. 143, p. 246.
- [114] W. W. Harris, F. L. Ball and A. T. Gwathmey, *Acta Met.*, 1957, vol. 5, p. 574.
- [115] J. Bénard and J. Talbot, *Rev. Met.*, 1948, vol. 45, p. 78.
- [116] G. Honjo, *J. Phys. Soc. Japan*, 1949, vol. 4, p. 330.
- [117] N. B. Gorny, *Soviet Physics JETP*, 1956, vol. 2, p. 687.
- [118] D. A. Vermilyea, *Acta Met.*, 1957, vol. 5, p. 492.
- [119] E. Bauer, *Z. Krist.*, 1958, vol. 110, p. 372.
- [120] G. Jellinek, *Z. Krist.*, 1958, vol. 110, p. 335.
- [121] A. T. Gwathmey, *Record Chem. Progress*, 1953, vol. 14, p. 117.
- [122] J. S. Dunn, *J. Inst. Metals*, 1931, vol. 46, p. 25.
- [123] A. P. C. Hollowes and E. Voce, *Metallurgia*, 1946, vol. 34, p. 119.
- [124] W. E. Campbell and U.B. Thomas, *Trans. Electrochem. Soc.*, 1947, vol. 91, p. 623.
- [125] D. E. Thomas, *J. Metals*, 1951, vol. 3, p. 926.
- [126] W. A. Backofen, *Deformation Processing*, Addison-Wesley, 1972.
- [127] D. V. Wilson, *J. Inst. Met.*, 1966, vol. 94, p. 84.
- [128] J. A. Szpunar and D. C. Hinz, *J. Mater.*, 1990, vol. 42, p. 39.
- [129] F. R. Larsen and A. Zarkades, *Properties of Textured Titanium alloys*, MCIC Report AF781884, Battelle Columbus Labs. USA, 1974.
- [130] K. Lee, M. S. Sandlin and K. J. Bowman, *J. Am. Ceram. Soc.*, 1993, vol. 76, p. 1793.
- [131] J. A. Szpunar, *Textures and Microstructures*, 1989, vol. 11, p.93.
- [132] K. T. Lee and J. A. Szpunar, *Mat. Sci. For.*, 1994, vol. 157 – 162, p. 989.